ISSN 0912-1803

PHOTON FACTORY ACTIVITY REPORT

1988

#6

NATIONAL LABORATORY FOR HIGH ENERGY PHYSICS, KEK

Photon Factory

Activity Report

1988

Staff members of the Photon Factory are gathering with the office building in their background

KEK Progress Report 88- 3 A/M

KEK Reports are available from:

Technical Information & Library
National Laboratory for High Energy Physics
1-1 Oho, Tsukuba-shi
Ibaraki-ken, 305
JAPAN

Phone: 0298-64-1171
Telex: 3652-534 (Domestic)
(0)3652-534 (International)
Fax: 0298-64-4604
Cable: KEKOHO

PREFACE

Since its foundation a decade ago, the Photon Factory has been playing an important role as a unique synchrotron X-ray radiation source in this country. Installation of various insertion devices, storage of intense positron beam and reduction of beam emittance are the substantial achievements in the last few years. Exploitation of the Tristan Accumulation Ring as a synchrotron radiation source has paved the way for a new potential of our development. All these activities have brought us an increase of beamlines and expansion of scientific fronts. The 3rd International Conference on Synchrotron Radiation Instrumentation held in Tsukuba was one of the most highlighted events for the facility.

Foreseeing the coming years, we will commit to open new research fields using the promising single bunch beam and circularly-polarized wiggler radiation. A possible application of the Tristan Main Ring for synchrotron radiation researches is also in our perspective. Of most importance is to further contribute to the progress of all the fields using the synchrotron radiation in this country. In order to pursue these objectives, it is worthwhile to review our accumulated resources. This report would present full materials for such discussions.

Jun-ichi Chikawa
Director of the Photon Factory

EDITORIAL

The editors are sending herewith a new volume of the Photon Factory Activity Report which summarizes our activities in the past year. The report compiles a large number of user's short reports on various kinds of experiment made in this facility. These reports are classified according to the PAC codes. The report also includes text describing the Injector Linac, Light Source and Instrumentation Department. Most materials in the text carries the names of authors to whom readers may contact directly for further discussion if necessary. Also intended is to make the volume a package of basic information on this facility such as various parameters of the machines, insertion devices, beamlines and experimental apparatuses.

The editors would like to appreciate Yoshiko Yamaguchi, Miyako Kimura, Yumi Sakurai and Kiwako Tateno for their hard work in preparation of this issue. Special thanks are due to Y. Kamiya for his persistent cooperation. All people who contributed to this volume are also acknowledged.

You can jump to the article by clicking its title.

Contents

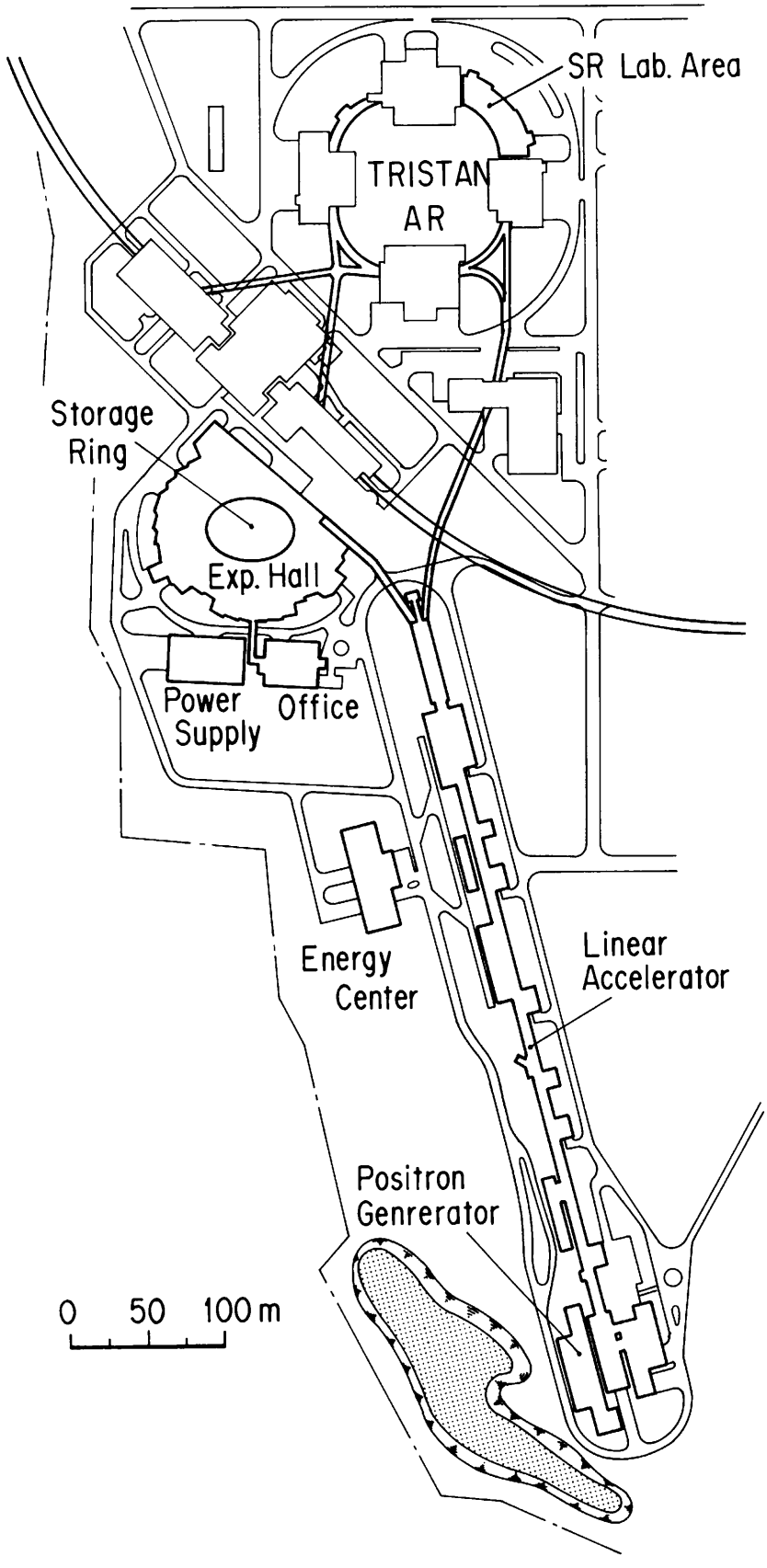

Fig. 1 Plan view of the Photon Factory

OUTLINE OF THE PHOTON FACTORY

A. INTRODUCTION

The Photon Factory (PF) is a national synchrotron-radiation research facility affiliated to the National Laboratory for High Energy Physics (KEK) under the sponsorship of the Ministry of Education, Science and Culture. It consists of a 2.5 GeV electron linac, a 2.5 GeV storage ring as a dedicated synchrotron light source, and beamlines and experimental stations to serve users with the synchrotron radiation for research fields such as physics, chemistry, biology, medical sciences, pharmacology, geology, and lithography. All of the facility is open to researchers from universities and research institutions belonging to the government, public organizations, private enterprises and those of foreign countries. Institutions affiliated to the Ministry are given the first priority as users. Applications from other organizations are also admitted with or without charge, depending upon the categories of their objectives.

The Photon Factory is located northern most of Tsukuba Science City, about 60 km north-east of Tokyo.

B. OVERVIEW OF THE FACILITY

The general view of the facility is shown in Fig. 1. The 2.5 GeV linac housed in a 450 m long enclosure is used as an injector for both the PF storage ring and the accumulation ring (AR) of TRISTAN. The PF storage ring has recently been facilitated with the flexibility of storing positrons in place of electrons. The AR has been partly used as high energy synchrotron radiation source from its bending magnet and partly augmented with a new insertion device to produce elliptically polarized radiation. It has been operated for synchrotron radiation users at an energy from 5 to 6 GeV.

C. ORGANIZATION AND STAFF

The organization structure of KEK is shown in Fig. 2. The PF consists of three departments; the Injector Linac, Light Source and Instrumentation. The organizational structure of PF including its personnel is shown in Fig.3. The Advisory Council for the PF was established to discuss scientific programs and management of the PF. This council consists of twenty-one of learned and experienced persons including ten non-KEK members (Table 1). The term of the membership is two years; half of the outside members are changed every year. The Program Advisory Committee (PAC) consisting of the members listed in Table 2 accepts proposals from users and sets priorities for the experiments.

In Table 3, the names of the staff members are listed to help make direct and quick contact. Also, the number of staff members and visiting scientists are summarized in Table 4.

D. BUDGET

The budgets of the Photon Factory during the construction period and after commissioning of the PF facility are shown in Table 5 and 6. Financial support for the PF is obtained from the government. During FY 1988, 8.8 % of the budget was spent for the construction of the AR beamlines and two new insertion devices. More beamlines have been constructed as shown in Table 7.

E. OPERATION TIME AND PROPOSAL

There are three machine operation terms scheduled for 1988 (Table 8). The operation timetable is summarized in Table 9. Fig. 4 shows the annual ring operation time of the PF. This indicates that the ring operation time has remarkably increased; the portion of user time has become larger in the ring operation time.

About 25 % of the operation time is used for machine studies. Such studies have been effective in improving stability, beam lifetime, low emittance operation, and positron accumulation.

There are three ways of access to the PF beamlines. The first category is for scientists from universities, research institutes belonging to the government or public organizations who can use the beamlines without charge if their proposals are accepted by the PAC. The deadlines for the applications are January 14 and July 15 every year. Proposals in urgency are also accepted any time. We call such accepted scientists "general users" and each subject is effective for two years. The number of proposals approved by the PAC since commissioning of the PF is listed in Table 10.

The second category is for scientists of private corporations which pay all the expenses. No approval by the PAC is required.

The third category is for collaboration between staff members of the PF and scientists from private corporations; no charge and no approval by the PAC are required but renewed every year starting April.

All the proposals belonging to the three categories approved during FY 1988 are listed at the end of this section.

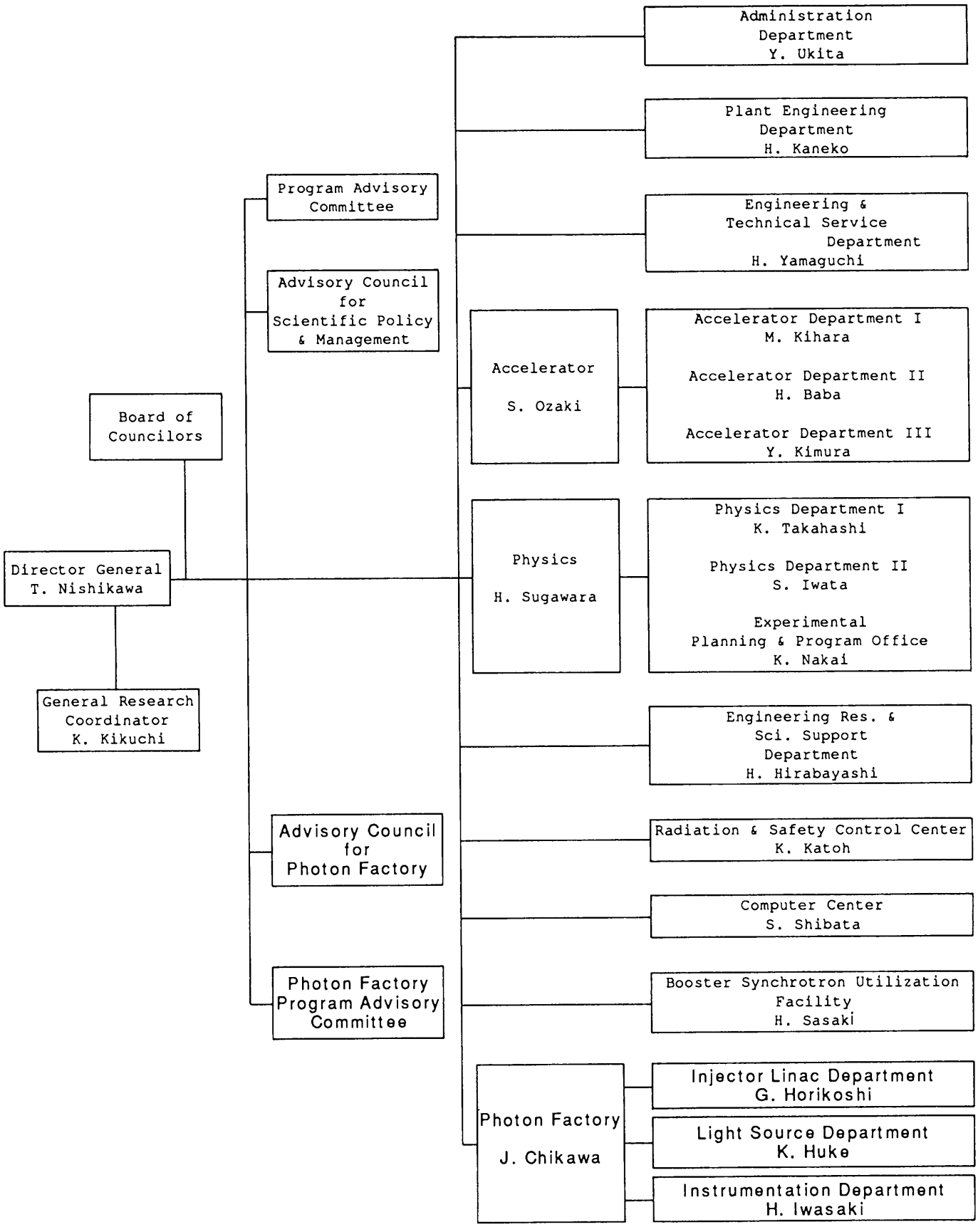

Fig. 2 Organization of KEK

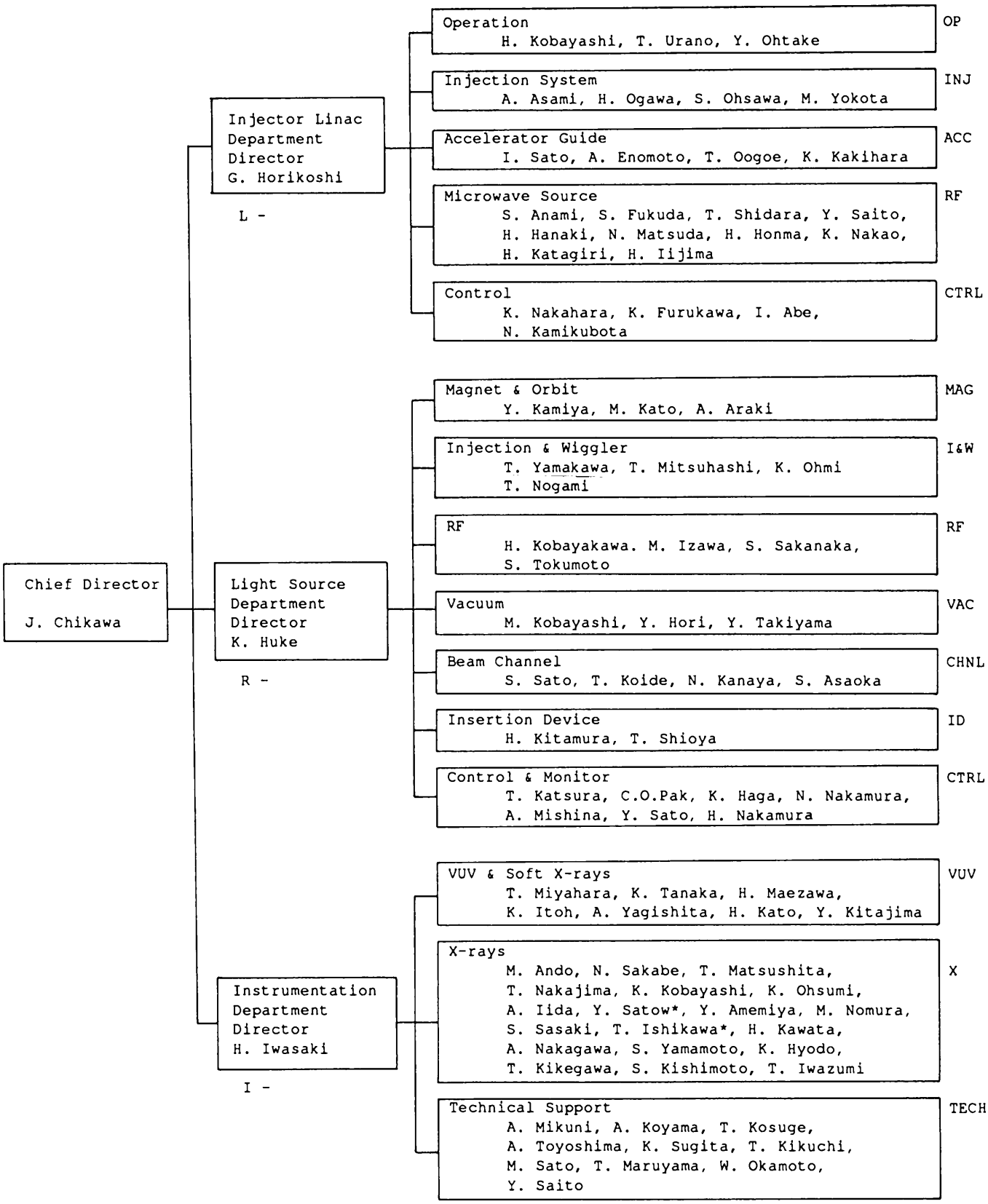

Fig. 3 Organization and Members of Photon Factory

* Present address : University of Tokyo

Table 1 Members of Advisory Council * Chairman ** Vice-Chairman

Prof. ANDO, Masami	PF Instrumentation Department, KEK
Prof. ASAMI, Akira	PF Injector Linac Department, KEK
Prof. FUJII, Yasuhiko	Institute of Materials Science, University of Tsukuba
Prof. HIEDA, Kotaro	Faculty of Science, Rikkyo University
Prof. HORIKOSHI, Gen-ichi	Head of PF Injector Linac Department, KEK
Prof. HUKE, Kazuo*	Head of PF Light Source Department, KEK
Prof. IIJIMA, Takao	Faculty of Science, Gakushuin University
Prof. ISHII, Takehiko	Institute for Solid State Physics, University of Tokyo
Prof. IWASAKI, Hiroshi	Head of PF Instrumentation Department, KEK
Prof. KASUYA, Tadao	Faculty of Science, Tohoku University
Prof. KATSUBE, Yukiteru	Institute for Protein Research, Osaka University
Prof. KIKUTA, Seishi	Faculty of Engineering, University of Tokyo
Prof. KOBAYAKAWA, Hisashi	PF Light Source Department, KEK
Prof. KOBAYASHI, Masanori	PF Light Source Department, KEK
Prof. KURODA, Haruo**	Faculty of Science, University of Tokyo
Prof. OHTA, Toshiaki	Faculty of Science, Hiroshima University
Prof. SAKABE, Noriyoshi	PF Instrumentation Department, KEK
Prof. SATO, Isamu	PF Injector Linac Department, KEK
Prof. SATO, Shigeru	PF Light Source Department, KEK
Prof. TOKONAMI, Masayasu	Faculty of Science, University of Tokyo
Prof. YAMAKAWA, Tatsuya	PF Light Source Department, KEK

Table 2 Members of Program Advisory Committee * Chairman

Prof. ASHIDA, Tamaichi	Faculty of Engineering, Nagoya University
Prof. HATANO, Yoshihiko	Faculty of Science, Tokyo Institute of Technology
Prof. HIEDA, Kotaro	Faculty of Science, Rikkyo University
Prof. HORIKOSHI, Gen-ichi	Head of PF Injector Linac Department, KEK
Prof. HUKE, Kazuo	Head of PF Light Source Department, KEK
Prof. IWASAKI, Hiroshi*	Head of PF Instrumentation Department, KEK
Prof. KIKUTA, Seishi	Faculty of Engineering, University of Tokyo
Prof. KOTANI, Akio	Faculty of Science, Tohoku University
Prof. KURODA, Haruo	Faculty of Science, University of Tokyo
Prof. MORI, Nobuo	Institute for Solid State Physics, University of Tokyo
Prof. MURATA, Yoshitada	Institute for Solid State Physics, University of Tokyo
Prof. NIHEI, Yoshimasa	Institute of Industrial Science, University of Tokyo
Prof. SUGI, Haruo	Faculty of Medicine, Teikyo University
Prof. SUZUKI, Hiroshi	Faculty of Science and Technology, Sophia University
Prof. TOKONAMI, Masayasu	Faculty of Science, University of Tokyo

Table 3 Name list of all staff members at the PF

ABE, Isamu	Tech.	L-CTRL	ABEI@JPNKEKVM
AMEMIYA, Yoshiyuki	Res. Ass.	I-X	AMEMIYA@JPNKEKVM
ANAMI, Shozo	Ass. Prof.	L-RF	
ANDO, Masami	Prof.	I-X	ANDO@JPNKEKVM
ARAKI, Akira	Tech.	R-MAG	
ASAMI, Akira	Prof.	L-INJ	
ASAOKA, Seiji	Tech.	R-CHNL	
CHIKAWA, Jun"ichi	Prof.	Chief Director	
ENOMOTO, Atsushi	Res. Ass.	L-ACC	ENOMOTOA@JPNKEKVX
FUKUDA, Shigeki	Ass. Prof.	L-RF	
FURUKAWA, Kazuro	Res. Ass.	L-CTRL	FURUKA@JPNKEKVX
HAGA, Kaiichi	Res. Ass.	R-CTRL	HAGA@JPNKEKVM
HANAKI, Hirofumi	Res. Ass.	L-RF	HANAKI@JPNKEKVX
HONMA, Hiroyuki	Tech.	L-RF	
HORI, Yoichiro	Res. Ass.	R-VAC	
HORIKOSHI, Gen"ichi	Prof.	L-Director	HORIKOSH@JPNKEKVX
HUKE, Kazuo	Prof.	R-Director	HUKE@JPNKEKVM
HYODO, Kazuyuki	Res. Ass.	I-X	
IIDA, Atsuo	Ass. Prof.	I-X	
IIJIMA, Hitoshi	Tech.	L-RF	
ISAWA, Masaaki	Res. Ass.	R-RF	ISAWA@JPNKEKVX
ISHIKAWA, Tetsuya	Res. Ass	I-X	ISHIKAWA@JPNKEKVM
ITO, Kenji	Res. Ass.	I-VUV	ITO@JPNKEKVM
IWASAKI, Hiroshi	Prof.	I-Director	
IWAZUMI, Toshiaki	Res. Ass.	I-X	

KAKIHARA, Kazuhisa	Tech.	L-ACC	
KAMIKUBOTA, Norihiko	Res. Ass.	L-CTRL	KAMI@JPNKEKVX
KAMIYA, Yukihide	Ass. Prof.	R-MAG	KAMIYA@JPNKEKVM
KANAYA, Noriichi	Res. Ass.	R-CHNL	KANAYA@JPNKEKVM
KATAGIRI, Hiroaki	Tech.	L-RF	
KATSURA, Tomotaro	Ass. Prof.	R-CTRL	KATSURA@JPNKEKVM
KATO, Hiroo	Res. Ass.	I-VUV	
KATO, Masahiro	Res. Ass.	R-MAG	
KAWADA, Hiroshi	Res. Ass.	I-X	
KIKEGAWA, Takumi	Res. Ass.	I-X	KIKEGAWA@JPNKEKVM
KIKUCHI, Takashi	Tech.	I-TECH	
KISHIMOTO, Syunji	Res. Ass.	I-X	KISHIMOTO@JPNKEKVM
KITAJIMA, Yoshinori	Res. Ass.	I-VUV	
KITAMURA, Hideo	Ass. Prof.	R-ID	KITAMURA@JPNKEKVM
KOBAYAKAWA, Hisashi	Prof.	R-RF	
KOBAYASHI, Hitoshi	Ass. Prof.	L-OP	
KOBAYASHI, Katsumi	Ass. Prof.	I-X	KOBAYASI@JPNKEKVM
KOBAYASHI, Masanori	Ass. Prof.	R-VAC	
KOIDE, Tsuneharu	Res. Ass.	R-CHNL	
KOYAMA, Atsushi	Tech.	I-TECH	
MAEZAWA, Hideki	Ass. Prof.	I-VUV	MAEZAWAH@JPNKEKVM
MARUYAMA, Tadashi	Tech.	I-TECH	
MATSUDA, Namio	Res. Ass.	L-RF	
MATSUSHITA, Tadashi	Prof.	I-X	MATSUS@JPNKEKVM
MIKUNI, Akira	Tech.	I-TECH	
MISHINA, Atsushi	Tech.	R-CTRL	MISHINA@JPNKEKVM
MITSUHASHI, Toshiyuki	Res. Ass.	R-I&W	
MIYAHARA, Tsuneaki	Ass. Prof.	I-VUV	MIYAHARA@JPNKEKVM
NAKAGAWA, Atsushi	Res. Ass.	I-X	NAKAGAWA@JPNKEKVM
NAKAHARA, Kazuo	Prof.	L-CTRL	
NAKAJIMA, Tetsuo	Ass. Prof.	I-X	NAKATETS@JPNKEKVM
NAKAMURA, Hajime	Tech.	R-I&W	
NAKAMURA, Norio	Res. Ass.	R-CTRL	
NAKAO, Katsumi	Tech.	L-RF	
NOGAMI, Takashi	Tech.	R-CTRL	
NOMURA, Masaharu	Res. Ass.	I-X	
OGAWA, Yujiro	Res. Ass.	L-INJ	OGAWA@JPNKEKVX
OHMI, Kazuhito	Res. Ass.	R-I&W	OHMI@JPNKEKVX
OHSAWA, Satoshi	Res. Ass.	L-INJ	OHSAWA@JPNKEKVX
OHSUMI, Kazumasa	Ass. Prof.	I-X	
OKAMOTO, Wataru	Tech.	I-TECH	
OOGOE, Takao	Tech.	L-ACC	
OTAKE, Yuji	Tech.	L-OP	
PAK, Cheol On	Ass. Prof.	R-CTRL	PAK@JPNKEKVM
SAITO, Yoshio	Res. Ass.	L-RF	
SAITO, Yuuki	Tech.	I-TECH	
SAKABE, Noriyoshi	Prof.	I-X	SAKABE@JPNKEKVM
SAKANAKA, Shyogo	Res. Ass.	R-RF	SAKANAKA@JPNKEKVM
SASAKI, Satoshi	Res. Ass.	I-X	SASAKIS@JPNKEKVM
SATO, Isamu	Prof.	L-ACC	
SATO, Masato	Tech.	I-TECH	
SATO, Shigeru	Prof.	R-CHNL	
SATOW, Yoshinori	Prof.	I-X	SATOW@JPNKEKVM
SATOH, Yoshihiro	Tech.	R-CTRL	
SHIDARA, Tetsuo	Res. Ass.	L-RF	SHIDARA@JPNKEKVM
SHIOYA, Tatsuro	Tech.	L-ID	
SUGITA, Kenji	Tech.	I-TECH	SUGITA@JPNKEKVX
TAKIYAMA, Youichi	Tech.	R-VAC	
TANAKA, Ken"ichiro	Ass. Prof.	I-VUV	TANAKA@JPNKEKVM
TOKUMOTO, Shuichi	Tech.	R-RF	
TOYOSHIMA, Akio	Tech.	I-TECH	
URANO, Takao	Res. Ass.	L-OP	
YAGISHITA, Akira	Res. Ass.	I-VUV	
YAMAKAWA, Tatsuya	Prof.	R-I&W	
YAMAMOTO, Shigeru	Res. Ass.	I-X	
YOKOTA, Mitsuhiro	Tech.	L-INJ	

Table 4 Annual number of staff & visiting scientists

Position	Department	1978	1979	1980	1981	1982	1983	1984	1985	1986	1987	1988
Chief Director		1	1	1	1	1	1	1	1	1	1	1
	Injector Linac	1	2	3	3	3	3	3	3	4	4	4
Professor	Light Source	1	4	4	4	4	4	4	3	4	4	4
	Instrumentation	0	0	0	1	1	1	1	2	3	4	5
Associate	Injector Linac	0	1	1	1	2	2	2	2	1	2	3
Professor	Light Source	1	5	4	4	4	3	5	5	3	3	3
	Instrumentation	0	0	1	3	4	5	5	8	7	9	7
Research	Injector Linac	1	3	4	6	7	8	9	10	11	10	10
Associate	Light Source	0	1	4	6	7	7	6	8	9	12	12
	Instrumentation	0	0	3	2	7	10	10	10	13	13	14
Technical	Injector Linac	0	0	2	3	5	5	6	6	7	8	9
Staff	Light Source	3	3	3	4	6	6	6	6	7	7	8
	Instrumentation	0	0	0	0	1	2	4	4	8	9	11
Visiting	Injector Linac	2	2	2	2	2	2	2	2	2	2	2
Scientist	Light Source	2	6	4	4	4	4	4	4	4	4	4
	Instrumentation	0	0	6	6	6	6	6	6	6	6	6
Total		12	28	42	51	64	69	74	80	90	97	103

Table 5 Construction budget (in million yen)

Item	1978	1979	1980	1981	1982
Salary	10	82	179	269	
Injector Linac	245	815	1,456	1,152	
Storage Ring	259	582	792	754	
Instrumentation	30	73	379	822	977
Civil Engineering	868	2,546	4,561	2,529	
Accelerator Operation	0	7	60	177	
Computer Rentals	0	0	34	135	
Cooling system & Electric Plant Operation	0	0	0	60	
Electricity	0	1	26	52	
Miscellaneous	29	95	154	233	126
Total	1,441	4,201	7,641	6,173	1,103

Table 6 PF-Budget in each fiscal year (in million yen)

Item	1982	1983	1984	1985	1986	1987	1988
Salary	402	474	484	510	561	561	642
PF Storage Ring (channel, insertion device, etc.)	0	0	0	153	131	1,045	267
PF Experiments	140	153	134	184	190	196	137
PF Operation & Maintenance	412	477	552	653	820	907	962
Computer Rentals	136	135	135	135	136	136	141
Positron Source & Electric Plant Operation	120	111	124	180	211	214	217
Electricity	209	226	257	338	381	331	355
PF-Industrial Cooperative Experiments	0	94	84	95	185	166	302
AR Construction and Experiments						398	259
Miscellaneous	115	134	115	127	162	120	301
Total	1,534	1,804	1,885	2,397	2,864	4,282	2,941

Table 7 Yearly account of beam channels

Fiscal	1981	1982	1983	9184	1985	1986	1987	1988
PF	6	8	8	8	10	12	13	13
Institutes	0	0	0	1	1	1	3	4
Industry	0	0	1	2	4	4	4	4
Total	6	8	9	11	15	17	20	21

Table 8 Summary of Operation Schedule in FY 1988 (Apr. 1988 - Mar. 1989) (hours)

Cycle	Linac	PF Ring	User's time	AR Ring	Dedicated to SR
1	1736	1496	1148	1632	240
2	1616	360	0	1584	240
3	1680	1328	1080	1648	0
Total	5032	3184	2228	4864	480

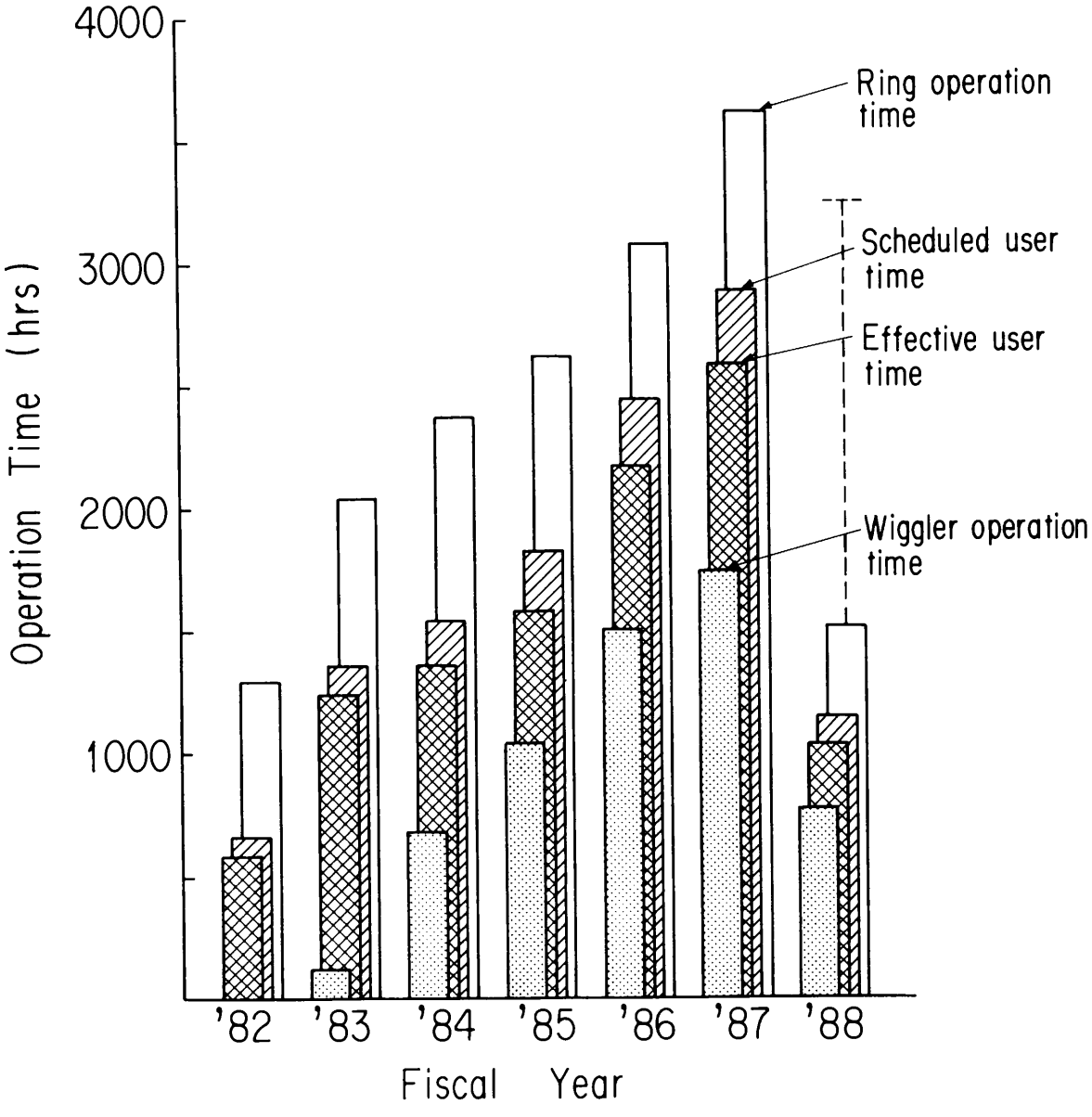

Fig. 4 Ring operation statistics

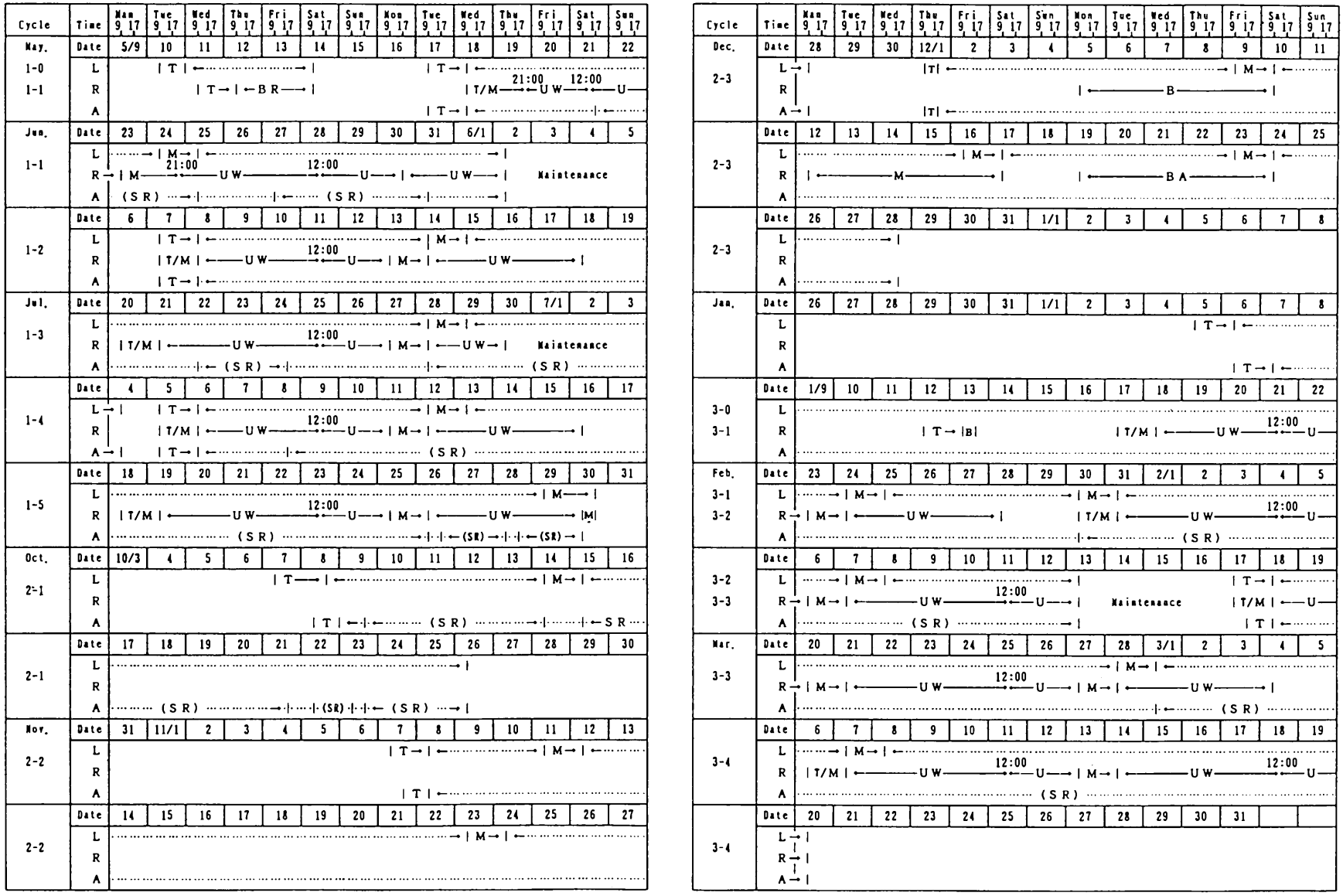

Table 9 Operation Schedule in FY 1988. L: Linac, R: PF Ring, A: Accumulation Ring, T: Machine Tuning, M: Machine Study, U: User's Beam Time without Vertical Wiggler, UW: User's Beam Time with Vertical wiggler, SR: Dedicated SR Use of AR, (SR): Parastic SR Use of AR, B: Photo-Baking of PF Ring and Beamline, BA: Beamline Alignment.

F. SEMINARS, MEETINGS AND PUBLICATIONS

In FY 1988, four seminars were given by foreign as well as domestic visiting scholars. Meetings were held for an annual symposium and for perspective views of possibilities in the coming generation utilizing the existing TRISTAN rings. The Factory publishes its monthly News in Japanese for communication between the users and the staff.

The Third International Conference on Synchrotron Radiation Instrumentation (SRI-88) was successfully held from August 29 to September 2 at the Auditorium of the Agency of Industrial Science and Technology (affiliate of the Ministry of International Trade and Industry) in Tsukuba. The number of participants was 480, including 167 foreign participants from 15 countries (71 from U.S.A., 28 F.R.G., 16 U.S.S.R., 14 U.K., 12 Italy, 10 France, 4 China, 3 Sweden, 2 Brazil, 2 Netherlands, and one each from Australia, Austria, Finland, Korea and Taiwan). All the participants enjoyed not only scientific sessions but also evening programs including receptions and a banquet. Next SRI meeting will be hosted by the SRC, Daresbury Laboratory, U.K. in 1991.

PF seminars

Vachette, P. (LURE)
Assembly of Brome Mosaic Virus Capsid: A Static and Kinetic Study by Solution X-ray Scattering.
December 14, 1987

Thui, H. (Hefei)
Present Status of Hefei National Synchrotron Radiation Laboratory.
December 9, 1987

Ikezawa, M., Namba, T. (Tohoku Univ.) and Fujimori, J. (NIRIM)
Far-Infrared Spectroscopy Using Synchrotron Radiation.
March 7, 1988

Wilkins, S.W. (CSIRO)
A New Class of Condensing-Collomating Channel-Cut Monochromators for SAXS, XRPD and Other Applications at SR Source.
April 8, 1988

Meetings

Workshop on SR Research Using TRISTAN Main Ring
March 23, 1988

3rd. International Conference in Synchrotron Rardiation (SRI-88)
August 29 - September 2, 1988

Workshop on High Pressure-High Temperature Studies at the TRISTAN
October 13-14, 1988

Synchrotron Radiation for the Study of Sstructural Phase Transition, Fluctuation and Disorder in Solids
October 21-22, 1988

6th Photon Factory Symposium
December 13-14, 1988

Publications

PHOTON FACTORY NEWS ISSN 0288-691 Vol.6, No.1-4

Table 10 Number of Proposals approved by PAC.

Research Field	1983	1984	1985	1986	1987	1988
(A) EXAFS	42	26	35	40	61	66
(B) Biology	18	18	28	28	32	38
(C) X-Ray	24	29	75	54	73	65
(D) VUV & Soft X-Ray	19	12	27	26	28	28
Total	103	85	165	148	194	197

List of Proposals Accepted in Fiscal 1988

Proposal Number	Spokesperson	Title
88-001	F. Marumo Research Laboratory of Engineering Materials, Tokyo Institute of Technology	Local structures around Fe^{2+} and Mn^{2+} ions in silicate glasses
88-002	T. Onishi Research Laboratory of Resources Utilization, Tokyo Institute of Technology	The study on the state of Indium in In_2O_3-CeO_2
88-003	T. Onishi Research Laboratory of Resources Utilization, Tokyo Institute of Technology	The study on the structure of intercalated CdS within layered $K_4Nb_6O_{17}$
88-004	H. Morikawa Research Laboratory of Engineering Materials, Tokyo Institute of Technology	EXAFS study of glasses in the system ZrF_4-BaF_2-CsF
88-005	M. Hirobe Faculty of Pharmaceutical Sciences, Univ. of Tokyo	EXAFS study on active intermediates of cytochrome P-450 models
88-006	H. Ino Faculty of Engineering, Univ. of Tokyo	Study of Fe-B amorphous alloys by EXAFS
88-007	H. Sakurai Faculty of Pharmaceutical Sciences, Tokushima Univ.	Structure analysis of vanadium binding substance in blood cells of ascidians by EXAFS method
88-008	T. Imura Faculty of Engineering, Hiroshima Univ.	Valence state of Cu in Cu-containing oxide superconductive thin films deposited by spinner coating techniques
88-009	K. Tanabe Faculty of Science, Hokkaido Univ.	Study of the structural change of Fe and Ni catalysts for coal liquids upgrading by means of EXAFS
88-010	K. Tanabe Faculty of Science, Hokkaido Univ.	Structural analysis of supported chromium oxide catalysts by EXAFS/XANES
88-011	K. Tanabe Faculty of Science, Hokkaido Univ.	Study of structure of TiO_2-ZrO_2 binary oxide using model thin films
88-012	K. Kunimori Institute of Materials Science, Univ. of Tsukuba	Rhodium-Niobia interaction on silica by air calcination at high temperature
88-013	T. Imura Faculty of Engineering, Hiroshima Univ.	EXAFS study on amorphous and metastable crystalline films containing tellurium
88-014	H. Nasu Faculty of Engineering, Hiroshima Univ.	Structure and stability of the infrared transmitting new glasses studied by K-edge absorption of the components
88-015	T. Yokoyama Faculty of Science, Hiroshima Univ.	Investigation of the spherical-wave and multiple-scattering effects in EXAFS spectroscopy
88-016	K. Kaneko Faculty of Science, Chiba Univ.	Two-dimensional development of active solids and their molecular adsorptivity

88-017	H. Yamazaki Faculty of Science, Okayama Univ.	Local structure of Fe-single crystal on the phase transitions
88-018	S. Ogasawara Faculty of Engineering, Yokahama National Univ.	EXAFS study of highly dispersed gold on supports
88-019	Y. Iwasawa Faculty of Science, Univ. of Tokyo	EXAFS studies on the design of surfaces by step-wise attachment with acetylacetonato metal complexes
88-020	Y. Iwasawa Faculty of Science, Univ. of Tokyo	EXAFS studies on the structure of Nb-dimer attached catalyst
88-021	Y. Iwasawa Faculty of Science, Univ. of Tokyo	EXAFS studies on the structure of one atomic layer super fine metal particle under the reaction condition
88-022	Y. Iwasawa Faculty of Science, Univ. of Tokyo	EXAFS studies on the quasi-phase transition of the surface structure of the SiO_2-supported noble metal super fine particle
88-023	T. Funabiki Faculty of Engineering, Kyoto Univ.	Elucidation of structure of catecholdioxygenase-model complexes and mechanism of oxygenqtion of aromatic ring
88-024	T. Nasu Faculty of Education, Yamagata Univ.	EXAFS study of amorphization process of Pd-Si alloy by mechanical alloying and mechanical grinding
88-025	H. Arashi Research Institute for Scientific Measurements, Tohoku Univ.	XANES of Tb-L_{III} in ZrO_2-Tb_2O_3 mixed conductors
88-026	M. Sano College of General Education, Nagoya Univ.	Systematic measurements of XANES spectra of copper-enzymes and their model compounds
88-027	M. Ichikawa Research Institute for Catalysis, Hokkaido Univ.	EXAFS and XANES studies on dynamic behavior of two-site promotion of CO catalyzed by bimetal clusters
88-028	T. Ohta Faculty of Science, Hiroshima Univ.	Surface EXAFS and surface XANES study on the structure of CS_2 molecule adsorbed on the surface of the single-crystal nickel
88-029	Y. Iwasawa Faculty of Science, Univ. of Tokyo	Polarized total-reflectant EXAFS studies on the change of shape in nickel fine particles
88-030	Y. Iwasawa Faculty of Science, Univ. of Tokyo	Fluorescence EXAFS studies of the local structures of Se added on Rh/ZrO_2
88-031	Y. Ujihira Faculty of Engineering Univ. of Tokyo	EXAFS study of Fe-Zr and Fe-Hf amorphous hydrogen-storing alloy
88-033	K. Shinohara Tokyo Metropolitan Institute of Medical Science	Biological application of X-ray microscopy
88-034	I. Nakai Department of Chemistry, Univ. of Tsukuba	Nondestructive X-ray fluorescence and absorption spectroscopic imaging of trace toxic elements doped in animal tissues
88-035	M. Hoshi Research Institute for Nuclear Medecine and Biology, Hiroshima Univ.	Yield of H_2O_2 in water with synchrotron X-ray radiation

88-036	M. Sasaki Radiation Biology Center, Kyoto Univ.	Studies on the mechanism of chromosome aberration formation by the use of monochromatic soft X-rays
88-037	M. Fukuda Fukui Medical School	Detection of the damaged and fragile sites irradiated with mono X-ray on a chromosome
88-038	M. Watanabe School of Medicine, Yokohama City Univ.	Neoplastic cell transformation by SR
88-039	H. Maezawa School of Medicine, Tokai Univ.	Action spectra for killing, genetic changes and DNA damages in mammalian cells irradiated with monochromatic X-rays (1-14 keV)
88-040	K. Kobayashi Photon Factory, National Laboratory for High Energy Physics	Survey of inner shell ionization-specific products in monochromatic soft X-ray irradiated biomolecules
88-041	K. Shinohara Tokyo Metropolitan Institute of Medical Science	Mechanisms of cell killing induced by Auger effect in cultured mammalian cells
88-042	N. Munakata National Cencer Center Research Institute	Action spectra for inactivation and mutagenesis of bacterial spores by exposure to monochromatic soft X-rays
88-043	A. Takenaka Faculty of Science, Tokyo Institute of Technology	Structural studies of protein crystals by rapid measurement of high resolution X-ray diffraction data
88-044	N. Kato School of Medicine, Nagoya Univ.	Analysis of crystals of bacterial lipopolysaccharides
88-045	T. Yamane Faculty of Engineering, Nagoya Univ.	Crystal analysis of protease and its inhibitor complex produced by streptomyces erythraeus
88-046	A. Suzuki Faculty of Engineering, Nagoya Univ.	Crystal structure analyses of Bowman-Birk type protease inhibitor
88-047	Y. Mitsui Faculty of Pharmaceutical Sciences, Univ. of Tokyo	Crystal structure analyses of protein inhibitor SSI and β-interferon
88-048	T. Tsukihara Faculty of Engineering, Tottori Univ.	Crystal structural analysis of biological macromolecular assembly
88-049	N. Yasuoka Basic Research Laboratory, Himeji Institute of Technology	X-ray diffraction studies of hydrogenase and high-molecular weight cytochrome in sulfate redusing bacteria
88-050	A. Nakagawa Photon Factory, National Laboratory for High Energy Physics	Phase determination of the crystal of proteins from sulfate-reducing bacteria using native anomalous scattering effect
88-051	P.B. Sigler Univ. of Chicago	High-resolution crystal structure of a specific protein/DNA complex
88-052	K. Kobayashi Photon Factory, National Laboratory for High Energy Physics	Study on the repair process of molecular damage produced by inner-shell ionization using repair deficient yeast
88-053	F. Yatagai The Institute of Physical and Chemical Research	Identification of soft-or ultrasoft-X-ray Induced mutations by DNA base sequence analysis

88-054	F. Marumo Research Laboratory of Engineering Materials, Tokyo Institute of Technology	A study on electron-density distribution in ilmenite-type crystals by short wave-length X-rays
88-055	F. Tokunaga Faculty of Science, Tohoku Univ.	Study on folding mechanism of bacteriorhodopsin peptide chain by X-ray diffraction
88-056	T. Mitsui Faculty of Engineering Science, Osaka Univ.	X-ray diffraction studies on molecular mechanism of muscle contraction by sinusoidal length changes
88-057	T. Mitsui Faculty of Engineering Science, Osaka Univ.	X-ray diffraction studies of the photointermediates of detergent treated purple membrane
88-058	Y. Tajima Faculty of Science, Tokyo Metropolitan Univ.	Medium angle X-ray diffraction of thin filaments of a tonically contracted muscle
88-059	M. Akiyama Department of Physics, Sapporo Medical College	X-ray diffraction study of phase transition in glucolipids
88-060	H. Kihara Department of Physics, Jichi Medical School	Dynamic study of oligomeric proteins, detected by stopped-flow X-ray scattering
88-061	H. Takeda Faculty of Science, Univ. of Tokyo	Distribution of trace elements in planetary materials with reference to their formation processes
88-062	H. Suematsu Faculty of Science, Univ. of Tokyo	Kinetic process of phase transitions in graphite intercalation compounds
88-063	A. Iida Photon Factory, National Laboratory for High Energy Physics	Evaluation and application of zone plates for hard X-ray
88-064	M. Ishikawa National Institute of Radiological Sciences	Quantitative determination of ultra-trace elements in marine samples by SR excited X-ray fluorescence analysis
88-065	H. Morikawa Research Laboratory of Engineering Materials, Tokyo Institute of Technology	Structural analysis of GeO_2-P_2O_5 glasses employing anomalous dispersion
88-066	K. Ohno National Research Institute for Metals	X-ray diffraction analysis of Ni-base superalloys
88-067	M. Kurahashi National Chemical Laboratory for Industry	Structure analysis of organic compounds by X-ray powder diffraction
88-068	Y. Kitano Faculty of Science, Hiroshima Univ.	Diffraction study of phase transition of Mg-Cd alloys
88-069	N. Hamaya Faculty of Engineering Science, Osaka Univ.	Novel sequence of commensurate-incommensurate phase transitions in ferroelectrics
88-070	Y. Fujii Faculty of Engineering Science, Osaka Univ.	Elastic anomaly in metallic superlattices
88-071	J. Harada Faculty of Engineering, Nagoya Univ.	Study of structual fluctuation at surface and interface of crystals from crystal truncation rod

88-072	H. Terauchi School of Science, Kwansei Gakuin Univ.	Synchrotron radiation research of artificial crystals
88-073	H. Oyanagi Electrotechnical Laboratory	Structural studies of high Tc oxide superconductors La_2CuO_4 and $Ba_2YCu_3O_y$ by EXAFS and X-ray diffraction
88-074	Y. Waseda Research Institute of Mineral Dressing and Metallurgy, Tohoku Univ.	Determination of the environmental structure around a specific atom in disordered materials by the anomalous X-ray scattering
88-075	S. Kagoshima College of Arts and Sciences, Univ. of Tokyo	X-ray study of structural changes under pressure in organic superconductors
88-076	T. Nakajima Photon Factory, National Laboratory for High Energy Physics	Alternate abstraction of circular polarization with different helicity and its utilization study
88-078	H. Sawada Photon Factory, National Laboratory for High Energy Physics	The detection of localized excited states in crystal structures by the single crystal X-ray diffraction method
88-079	Z. Barnea School of Physics, Univ. of Melbourne	Observation of the effects of anharmonicity and bonding on bijvoet intensity ratios
88-080	D.C. Creagh Physics Dept., Univ. N.S.W. (Australia)	Studies of the structural and magnetic properties of the light rare earth elements, their intermetallic compounds and their hydrides
88-081	H. Morikawa Research Laboratory of Engineering Materials, Tokyo Institute of Technology	Structural analysis of pyroxene melt
88-082	T. Nose Faculty of Engineering, Tokyo Institute of Technology	Concentration fluctuations within chain dimension in phase separation of polymer blends
88-083	S. Isoda The Institute for Chemical Research, Kyoto Univ.	Crystallization and melting in polymer single crystals
88-084	K. Hasegawa Faculty of Engineering, Univ. of Tokyo	Development of an amorphous silicon position-sensitive X-ray detector and its application
88-085	H. Hashizume Research Laboratory of Engineering Materials, Tokyo Institute of Technology	Structure analysis of crystal interfaces and surfaces by grazing-incidence X-ray diffraction
88-086	J. Yoshimura Faculty of Engineering, Yamanashi Univ.	Study of crystal moiré
88-087	K. Gohhara Faculty of Engineering, Nagoya Univ.	Photon counting in X-ray diffraction
88-088	A. Kamio Faculty of Engineering, Tokyo Institute of Technology	Dynamical structures of ordering in Al-Li alloys
88-089	T. Masujima Inst. Pharmaceutical Sci., Hiroshima Univ.	Development of synchrotron radiation photoacoustic spectroscopy

88-090	M. Hidaka Faculty of Science, Kyushu Univ.	Crystallographical study of condensed matters in un-equilibrium structures
88-091	M. Akaogi Faculty of Science, Kanazawa Univ.	Accurate determination of the phase boundary in TiO_2 at high pressures and high temperatures
88-092	A. Matsumuro Faculty of Engineering, Nagoya Univ.	Measurements of P-V-T relation on aluminum
88-093	A. Matsumuro Faculty of Engineering, Nagoya Univ.	Measurements of debye temperature of supersaturated aluminum solid solution
88-094	K. Hyodo Photon Factory, National Laboratory for High Energy Physics	Fundamental studies on high resolution computed tomography
88-095	Y. Endoh Faculty of Science, Tohoku Univ.	Search for correlation between structure and superconductivity, magnetism in oxide superconductors
88-096	J. Mizuki Fundamental Research Laboratories, NEC Corporation	Surface and interface studies of semiconductor with a grazing incidence X-ray diffraction
88-097	T. Kikegawa Photon Factory, National Laboratory for High Energy Physics	Development of the precise diffraction intensity measurement at high pressure and high temperature with high-energy synchrotron radiation and MAX80 system
88-098	T. Miyahara Photon Factory, National Laboratory for High Energy Physics	Polarimetric characterization of optical elements in VUV and soft X-ray region
88-099	K. Tanaka Photon Factory, National Laboratory for High Energy Physics	Development of experimental techniques for the study of photochemical reactions on a surface
88-100	Y. Hatano Faculty of Science, Tokyo Institute of Technology	A study of dissociation processes of hydrocarbon and other organic molecules by means of the pulse structure of synchrotron radiation
88-101	K. Ueda Research Institute for Scientiffic Measurements, Tohoku Univ.	High-resolution absorption spectroscopy of alkaline-earth and rare-earth metal vapors
88-102	K. Maeda Faculty of Education, Kumamoto Univ.	Absorption cross sections of rare gases near the photoionization threshold energy
88-103	K. Nakagawa College of Arts and Sciences, Univ. of Tokyo	Test of the irradiation system for biological materials by means of radiation-chemical reaction in solids
88-104	H. Namba Faculty of Science, Univ. of Tokyo	Characterization of metal mirrors by reflectivity measurement in soft X-ray region
88-105	K. Seki Faculty of Science, Hiroshima Univ.	Study of the polymerization process of diacetylene long-chain compounds by inner shell polarized spectra
88-106	T. Hayaishi Institute of Applied Physics Univ. of Tsukuba	Dissociation processes after inner-shell ionization of molecules

88-107	T. Koide Photon Factory, National Laboratory for High Energy Physics	Study of circular dichroism in photoelectron angular distributions from adsorbates on Ni(100) surface
88-108	T. Takahashi Faculty of Science, Tohoku Univ.	Photoelectron spectroscopy of high-Tc superconductor single crystals
88-109	T. Hattori Musashi Institute of Technology	Valence band spectra near Si-SiO_2 interface for oxides prepared using superclean methods
88-110	T. Suzuki Faculty of Science and Technology, Sophia Univ.	Soft-X-ray p. A scattering by light element solids
88-111	K. Kaneko Faculty of Science, Chiba Univ.	Local structure of ultrafine and amorphous oxyhydroxides
88-112	H. Ino Faculty of Engineering, Univ. of Tokyo	Study of Al-Si-(Mn, Fe, V) amorphous and quasicrystalline phase by EXAFS
88-113	K. Shibata Faculty of Engineering, Univ. of Tokyo	Observation of interaction between alloying elements in steels by using EXAFS
88-114	T. Yagi The Institute for Solid State Physics, Univ. of Tokyo	Measurement of density using X-ray absorption under high pressure
88-115	T. Murata College of Liberal Arts and Sciences, Kyoto Univ.	Srudy of relaxation of Cu^+ impurities in alkali halides by fluorescence EXAFS
88-116	I. Watanabe Faculty of Science, Osaka Univ.	Study of the debye-waller factor in EXAFS of transition metal complexes
88-117	G. Adachi Faculty of Engineering, Osaka Univ.	EXAFS studies on local structure of amorphous $LaNi_5$ films
88-118	S. Kagawa Faculty of Engineering, Nagasaki Univ.	EXAFS and XANES studies on the coordination of copper ion in zeolites
88-119	K. Kikuchi Faculty of Science, Tokyo Metropolitan Univ.	EXAFS of conductive organosilicon compounds
88-120	T. Yamamura Science Univ. of Tokyo	EXAFS and XANES study of the models for hydrogenase active site (Ni) : study of NiS_xN_y (Ni^{2+} and Ni^{3+}) mixed coordination systems
88-121	T. Yokokawa Faculty of Science, Hokkaido Univ.	EXAFS study on borogermanate glasses
88-122	T. Yokokawa Faculty of Science, Hokkaido Univ.	EXAFS and XANES investigations of oxide glasses containing iron
88-123	H. Hattori Faculty of Science, Hokkaido Univ.	Study of crystallization process of binarymetal oxides including Fe
88-124	M. Ichikawa Research Institute for Catalysis, Hokkaido Univ.	EXAFS and XANES studies on characterization of electron-donor-acceptor metal phthalocyanin complexes entrapped in zeolite supercages

88-125	H. Arashi Research Institute for Scientific Measurements, Tohoku Univ.	Investigations of electronic conduction mechanisms in electron-ion mixed conductor CeO_2-Tb_4O_7 by using XANES
88-126	A. Tomita Chemical Research Institute of Non-Aqueous Solutions, Tohoku Univ.	EXAFS studies on the local structures of metals dispersed on carbon
88-127	T. Kawashima Department of Chemistry, Univ. of Tsukuba	EXAFS studies of Cu(I, II)-NH_3, py, phen, bpy, complexes in aqueous solution
88-128	H. Kuroda Faculty of Science, Univ. of Tokyo	XANES of low-dimensional complexes with highly oxidized Ni and Cu
88-129	M. Misono Faculty of Engineering, Univ. of Tokyo	EXAFS analysis of supported mixed oxide thin films
88-130	T. Onishi Research Laboratory of Resources Utilization, Tokyo Institute of Technology	Structural study of ruthenium cluster supported catalyst for nitrogen activation
88-131	T. Onishi Research Laboratory of Resources Utilization, Tokyo Institute of Technology	Structure of ammine complexes of noble metals intercalated in $K_4Nb_6O_{17}$
88-132	T. Fukushima Faculty of Engineering, Yokohama National Univ.	Changes in local structure of supported metal catalysts by O_2 and CO
88-133	M. Koiwa Faculty of Engineering, Kyoto Univ.	Nature of oxide particles in alloys formed by internal oxidation
88-134	K. Sumiyama Faculty of Engineering, Kyoto Univ.	Structure of nonequilibrium alloys produced by vapor quenching
88-135	A. Yoshiasa Faculty of Science, Hiroshima Univ.	Local structure of melilite groups, $(Ca, Sr)_2$ (Mg, Mn, Co, Zn) Si_2O_7
88-136	Y. Yoshikawa Faculty of Science, Okayama Univ.	EXAFS studies in oxide films on metal fine-particles
88-137	H. Maeda Faculty of Science, Okayama Univ.	Study of the debye-waller factors in EXAFS
88-138	M. Hida School of Engineering, Okayama Univ.	Experimental examination in "phase shift transferability" on EXAFS analysis
88-139	Y. Miura School of Engineering, Okayama Univ.	Structure of 110K-phase of the Bi, Pb-Sr-Ca-Cu-O system
88-140	T. Yokoyama Faculty of Science, Hiroshima Univ.	EXAFS and XANES studies on Br-adsorbed small metal particles
88-141	I. Nakai Tottori Univ.	The structure of amorphous Gd-based alloys
88-142	T. Tanase Faculty of Science, Toho Univ.	An EXAFS study on Bi- and poly-nuclear transition metal complexes

88-143	A. Nishijima National Chemical Laboratory for Industry	EXAFS and XANES study on the crystallization of pentasil zeolites
88-144	K. Sakurai National Research Institute for Metals	EXAFS study on the amorphous alloy by mechanical alloying
88-146	K. Koto Tokushima Univ.	Local structures of SiO_2 polymorphs and amorphous state
88-147	T. Earnest Dept. of Biochemistry and Biophysics, Univ. of California, San Francisco	Crystal structure of transmembrane ion channels: colicin Ia and the nicotinic acetylcholine receptor
88-148	L. Zheng-jiong Institute of Biophysics, Academia Sinica	The collection of diffraction data of P. versicolor D-glyceraldehyde-3-phosphate dehydrogenase and the modified enzyme carrying the fluorescent derivative
88-149	Y. Muroga Faculty of Engineering, Nagoya Univ.	Conformational change of poly-N^5-(2-hydroxyethyl) L-glutamine
88-150	Y. Hiragi The Institute for Chemical Research, Kyoto Univ.	Kinetic observation of denaturation-renaturation process of ribonuclease and analysis of its intermediate structure
88-151	K. Tanaka Nagasaki Univ.	Studies on aggregation of proteoglycan and hyaluronic acid by small angle X-ray scattering
88-152	Y. Sano National Institute of Agrobiological Resources	Reconstitution process of tobacco mosaic virus by time-resolved small-angle scattering
88-153	K. Takakura International Christian Univ.	NMR study of molecular damage in nucleic acid induced by SR-soft X-ray Irradiation
88-154	F.S. Mathews Washington Univ. Medical School	Crystallographic studies of the amicyanin methylamine-dehydrogenase complex by synchrotron radiation using image plate
88-155	M.G. Rossmann Dept. of Biological Science, Purdue Univ.	Structure of viruses
88-157	H. Tagawa College of Science and Technology, Nihon Univ.	Dynamical SAXS investigations on micro-phase segregated structures of segmented polyurethanes
88-158	A. Iida Photon Factory, National Laboratory for High Energy Physics	Surface characterization by grazing incidence XRF
88-159	R. Uno College of Humanities and Sciences, Nihon Univ.	Independent measurement of temperature factor of individual atoms in diatomic crystals
88-160	I. Shirotani Muroran Institute of Technology	Phase transitions of phosphorus and phosphorus-arsenic alloy at very low temperatures and high pressures
88-161	K. Ohshima Institute of Applied Physics, Univ. of Tsukuba	Study on the precursive phenomena of phase transion from two-dimensional layer compounds and sodium
88-162	H. Iwasaki Photon Factory, National Laboratory for High Energy Physics	Study of phase transitions in alloys by time resolved two-dimensional recording of diffuse scattering

88-163	K. Ishida Faculty of Science and Technology, Science Univ. of Tokyo	X-ray magnetic scattering of hexagonal ferrite
88-164	K. Tsuji Faculty of Science and Techology, Keio Univ.	Low temperature and high pressure X-ray study on the pressure-induced phase transition of amorphous semiconductors
88-165	H. Suzuki Tokyo Engineering Univ.	Construction of eqiupments for X-ray topography of solid helium at ultra low temperatures and observation of lattice defects by the equipment
88-166	Y. Oka College of Liberal Arts and Sciences, Kyoto Univ.	Crystal structure analysis of a new vanadium oxide $V_2O_{4.8}$
88-167	O. Nittono Faculty of Engineering, Tokyo Institute of Technology	Microstructure and lattice distortions of porous silicon layers studies by means of X-ray diffraction techniques
88-168	F. Itoh The Research Institute for Iron, Steel and Other Metals, Tohoku Univ.	Study of electron momentum density in matters by means of high resolution comptom scattering
88-169	Y. Sugita Faculty of Science, Toyama Univ.	Section topography with high order reflection and its application to micro-defects in Si crystals
88-170	S. Nanao Institute of Industrial Science, Univ. of Tokyo	Measurements of the pair distribution functions of quasi-crystalline alloys with high spatial resolution
88-171	S. Nanao Institute of Industrial Science, Univ. of Tokyo	Structural study of Fe-Tb amorphous thin films with use of anomalous X-ray scattering
88-172	H. Hirayama Radiation & Safety Control Center, National Laboratory for High Energy Physics	Experiments on the energy deposition of X-rays to matter
88-173	H. Ino Faculty of Engineering, Univ. of Tokyo	XSAS study of formation process of clusters in liquid-quenched La-Fe alloy
88-174	K. Komaki College of Arts and Sciences, Univ. of Tokyo	Study on polarization channeling radiation
88-175	C. Masuda National Research Institute for Metals	Damage and fracture analysis for composite materials by X-ray CT using monochromated synchrotron radiation
88-176	Y. Fujinaga The Research Institute for Iron, Steel and Other Metals, Tohoku Univ.	A direct observation of pressure-induced transformations in Au-Ge and Au-Si alloys
88-177	N. Mohri The Institute for Solid State Physics, Univ. of Tokyo	Orthorhombic to tetragonal phase transition in high T_c superconductors $RM_2Cu_3O_{7-8}$ under high pressure
88-178	T. Yagi The Institute for Solid State Physics, Univ. of Tokyo	Phase relations and equations of state of calisium baring silicates
88-179	N. Hamaya Faculty of Engineering Science, Osaka Univ.	Kinetics of phase transitions of long period structures

88-180	S. Endo Research Center for Extreme Materials, Osaka Univ.	Lattice parameters of $R_2Fe_{14}B$ (R=Nd, Y, Ce)under high pressure and temperature
88-181	E. Ohtani Faculty of Science, Ehime Univ.	In situ observation of the phase transition in Mg_2SiO_4 by double stage multi anvil system
88-182	K. Tsuji Faculty of Science and Technology, Keio Univ.	Structure of liquid cesium and liquid tellurium under pressure
88-183	S. Tagawa Nuclear Engineering Research Laboratory, Faculty of Engineering, Univ. of Tokyo	Picosecond synchrotron radiation pulse radiolysis
88-184	H. Maezawa Photon Factory, National Laboratory for High Energy Physics	XES and XPS study of 3d shell in all rare-arth elements
88-185	T. Sasaki National Laboratory for High Energy Physics	Inner-shell photodissociation processes of small linear molecules
88-186	H. Tawara Institute of Plasma Physics, Nagoya Univ.	Production mechanisms of multiply charged ions from rare gases and their frozen layers by hard X-rays and their applications
88-187	T. Takahashi Faculty of Science, Tohoku Univ.	Soft X-ray spectroscopy of high-T_c superconductor single crystal
88-188	H. Kuroda Faculty of Science, Univ. of Tokyo	Study of sulfur adsorption on stepped surface of Ni single crystals
88-189	T. Ohta Faculty of Science, Hiroshima Univ.	Structural studies on S- or Cl-adsorbed metal surfaces by use of soft X-ray standing-wave method
88-190	A. Nishijima National Chemical Laboratory for Industry	Study on S $_{KLL}$ Auger electron spectra by X-ray excitation near S K-edge
88-191	T. Tomiki Faculty of Science, Univ. of Ryukyus	VUV spectra of single crystals of α-Al_2O_3, YAG and YAP
88-192	H. Kato Photon Factory, National Laboratory for High Energy Physics	Angle resolved photoelectron spectroscopy of rare gas on Mo surfaces
88-193	S. Suga The Institute for Solid State Physics, Univ. of Tokyo	UPS studies of Kondo states in Yb and Sm compounds
88-194	E. Miyazaki Faculty of Science, Tokyo Institute of Technology	Angle-resolved photoemission study of NbC (111) clean and O_2, CO-adsorbed surface
88-195	M. Kitajima National Research Institute for Metals	UPS study on electronic state of material surface irradiation-stimulated with proton
88-196	M. Yanagihara Research Institute for Scientific Measurements, Tohoku Univ.	Study on the thermal resistivity and radiation damage of soft X-ray multilayers

88-197	H. Hashizume Research Laboratory of Engineering Materials, Tokyo Institute of Technology	Development of X-ray standing-wave method for surface/interface structures on mosaic crystals
88-198	N. Nagashima College of Engineering, Nihon Univ.	Analysis of structure and electronic states in SiO_2-Si system by soft X-ray spectroscopy
88-U002	Y. Sakisaka Faculty of Science, Kyoto Univ.	Angle-resolved photoemission spectroscopy of high-Tc superconducting $YBa_2Cu_2O_{7-x}$ single crystal thin films
88-U003	M. Funaki National Institute of Polar Research	Study on internal structure of meteorites with SR-CT
88-Y001	K. Wada The Institute of Physical and Chemical, Mitsubishi Kasei Co.	The EXAFS study of catalysts and thin films
88-Y002	T. Hisatsugu Fujitsu Laboratories Ltd.	Synchrotron radiation test for exposure system in BL-17C and BL-17A
88-Y003	C. Uemura NTT Applied Electronics Laboratories	Analysis, lithography and photo-reaction using SR
88-Y004	J. Matsui Fundamental Research Laboratories, NEC Corporation	X-ray optics, X-ray lithography and photo-chemical reaction experiments
88-Y005	N. Sato Honda Research & Development Co., Ltd.	Relationship between XANES-EXAFS spectra and structure modification of Hopeite films by manganese component
88-Y006	K. Hayakawa Advanced Research Laboratory, Hitachi Ltd.	BL-8A: Soft X-ray diffractometry, B; InSb (111) monochromatized Si-K EXAFS, C; X-ray digital radiography experiment and irradiation of X-rays to semiconductor devices
88-Y007	S. Maeyama NTT Applied Electronics Laboratories	EXAFS measurements on superconducting material and electrode material
88-Y008	T. Hisatsugu Fujitsu Limited	Exposure tests by synchrotron radiation in BL-17A and BL-17C
88-Y009	K. Wada The Institute of Physical and Chemical Mitsubishi Kasei Co.	The EXAFS study of catalysts and thin films
88-Y010	T. Takyuu Central Research Laboratories, Idemitsu Kosan Co., Ltd.	An EXAFS study of platinum and iron zeolite
88-Y011	S. Maeyama NTT Applied Electronics Laboratories	EXAFS measurements on superconducting materials
88-Y012	K. Hayakawa Advanced Research Laboratory, Hitachi Ltd.	BL-8A; Soft X-ray diffractometry, B; InSb (111) monochromator test, C; X-ray digital radiography and X-ray lithography
88-C001	M. Matsumoto LSI Laboratories, NTT	Study on UHV materials by photodesorption measurements
88-C002	T. Murashita LSI Laboratories, NTT	Study on photo-stimulated desorption using synchrotron radiation

88-C003	T. Kitano Central Research Laboratories, NEC Corp.	Characterization of semiconductor materials by high precision X-ray optics
88-C004	N. Yoshioka LSI Research & Development Laboratory,.Mitsubishi Electric Corp.	Industrial application of soft X-ray spectroscopy
88-C005	T. Ito Fujitsu Laboratories Ltd.	Study of new method in vapor-phase epitaxial growth using synchrotron radiation
88-C006	T. Takigawa ULSI Research Center, Toshiba Corp.	Study of new method in photochemical etching with synchrotron radiation
88-C007	T. Kojima Takatsuki Research Laboratory, Sumitomo Chemical Co., Ltd.	Dynamic structure of synthetic polymer materials using X-ray small angle scattering
88-C008	S. Yasuami Research & Development Center, Toshiba Corp.	Characterization of semiconductor materials using soft X-ray EXAFS and X-ray diffraction
88-C009	M. Kakuchi LSI Laboratories, NTT	Technology of soft X-ray holography using undulator radiation
88-C010	M. Ohmura Technical Research Center, NKK Co.	Study of impurity effects on crystal quality by means of X-ray topography
88-C011	T. Ohtsubo R & D Laboratories, Nippon Steel Corp.	Photoemission study of surfaces using synchrotron radiation
88-C012	S. Suzuki Tsukuba Research Center, Sanyo Electric Co., Ltd.	Micro patterning by synchrotron radiation
88-C013	S. Kawado Research Center, Sony Corp.	Development of ultrafast X-ray detector system
88-C014	H. Hashimoto Toray Research Center	Structural studies of thin films and surfaces by means of grazing incidence X-ray diffraction
88-C015	H. Ayato Research Laboratories, Ashigara, Fuji Photo Film Co., Ltd.	Structure analysis of halogen compound by EXAFS method with SR
88-C016	Y. Muramatsu Applied Electronics Laboratories, NTT	Monochromator technologies for highly brilliant insertion device radiation
88-C017	S. Fujie Mitsubishi Heavy Industries, Ltd.	Study of high gradient accelerator structure
88-C018	M. Funabashi Research Development Corp. of Japan	Study of photochemical processes on surfaces using synchrotron radiation
88-C019	H. Nagata Research Development Corp. of Japan	Analytical studies on fabricated surfaces using synchrotron radiation
88-C020	Y. Asatake Mitsubishi Kasei Corp.	Intensity measurement of X-ray diffraction from bio-macromolecular small crystals
88-C021	K. Katayanagi Protein Engineering Research Institute	X-ray crystal analysis of amirase inhibitor for drug design

88-C022	Y. Fukuda Canon Research Center, Canon Inc.	Studies on the optical properties of focusing multilayer soft X-ray mirrors
88-C023	T. Ohtsubo Nippon Steel Corp.	Dynamic observation of materials processing by synchrotron radiation
88-C024	T. Yagi Development Center, Konica Co.	Structure analysis of halogen compound by powder diffraction method with synchrotron radiation

U: approved by PAC in urgency,
Y: approved for charged beam time,
C: collaborations between the Photon Factory and institutes of private companies.

Injector Linac Department

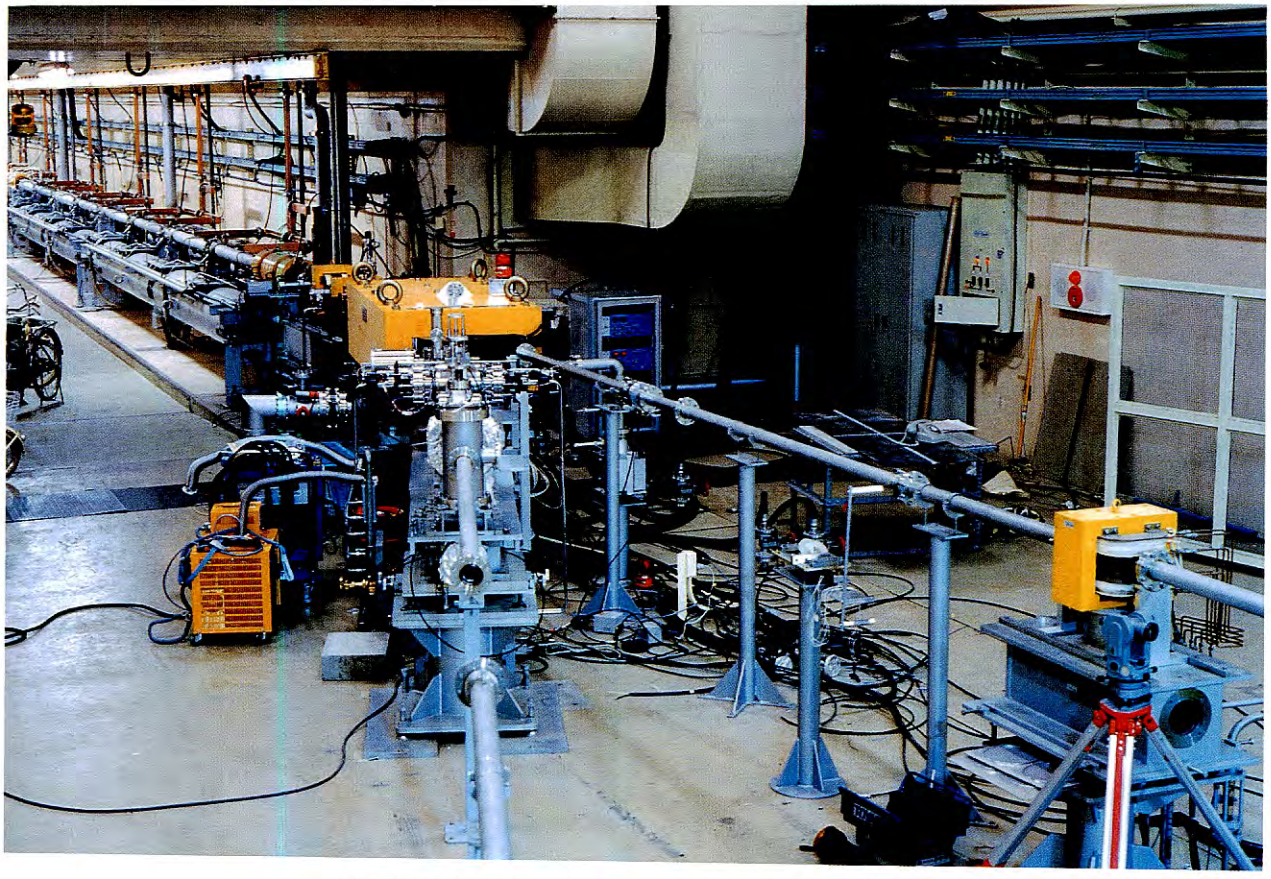

The 2.5 GeV energy-analyzing station at the end of the linac.

INJECTOR LINAC DEPARTMENT

A. INTRODUCTION

With an increase of activity in both the Photon Factory (PF) and TRISTAN, the total operation time of the electron linac has been largely increased up to 4500 hours during this period, which is the largest operation time among accelerators at KEK. This increase of operation time demands much manpower for operation, and results in a decrease in the available time for the machine maintenance. To cope with such a situation, several proposals have been made to improve accelerator performance and to reduce the necessary manpower for operation as well. We initiated the following plans.

Work to reinforce the control system has been started. A new super mini-computer was added to the system. The installation is presently in the final stage of adjustment. It is expected to increase the ability of the system; capacity of the memory for the data taking and storing; and the working area for the program developments.

Work to improve the beam monitoring system was started. The old monitoring system was insufficient for tracing such beam parameters as the emittance, profile, energy and position along the length of the linac. Efforts were made to bring all beam current monitors, some of which were being left unfinished, into operation. The beam energy analyzing systems at four key locations ((1) in front of the electron-positron conversion target of the positron generator; (2) at the low energy side (35 MeV) of the 2.5 GeV main linac; (3) at the 30 degree deflection point of beam transportation line from the positron generator to the main linac; and (4) at the end of the 2.5 GeV linac) will be completed by adding some components which had been lacking. This work will be completed by the end of this fiscal year and is expected to make the operation and adjustment of the accelerator very easy.

The high-power rf system was reinforced in the electron linac part of the positron generator. It is very important to obtain an intense electron beam of short pulse focused on the conversion target. For this purpose, the adjustment of the injection system of the electron part of the positron generator is very important. It has been pointed out that the rf power is insufficient for the injection system to obtain its optimum condition for the beam with an increase in electron beam intensity. In the old rf system, the rf output from one klystron unit was divided into the buncher section and following accelerator guides. In the new version, a new klystron unit has been installed to feed the accelerator guides independently. This allows an easy adjustment of the buncher section and has increased the beam energy.

In the last issue we reported on a very serious problem concerning high-power klystrons. Arcing at the oxide cathode assembly in the klystrons occurred very frequently, and this shortened the lifetimes of the tubes. It was observed that contamination on the electrode surfaces in the vicinity of the cathode was very large. It may have had something to do with the material quality and treatment procedure in the manufacturing process of the oxide cathode assembly. We are continuing R & D of a high-current oxide cathode to clarify the cause of this problem. At the same time, we newly introduced BI (barium impregnated) cathode into our high-power klystrons. Six klystrons with BI cathodes are presently operating well with a very small downrate. A statistical estimation gives us more than 20,000 hours as the average lifetime of the new klystron.

G. Horikoshi

B. OPERATION

1. OPERATIONAL STATUS

During the period from October 1987 to September 1988, the linac has been successfully

Table 1 Operation and failure time of each cycle

term-cycle	date	operation time (minutes)	failure time	operation rate (percent)
FY 1987				
2-1	10/13-10/31	25920	479	98.15
2-2	11/04-11/18	20040	288	98.56
2-3	11/25-12/07	17230	2843	83.5
2-4	12/07-12/23	22995	819	96.44
3-0	01/13-01/18	5215	111	97.87
3-1	01/18-02/04	24480	1198	95.11
3-2	02/09-02/29	28800	337	98.83
3-3	03/03-03/20	24290	214	99.12
FY 1988				
1-0	05/10-05/14	4170	40	99.04
1-1	05/17-06/02	23015	197	99.14
1-2	06/07-06/20	18660	5603	70.00
1-3	06/20-07/04	20160	85	99.58
1-4	07/05-07/18	18720	186	99.01
1-5	07/18-07/30	17880	264	98.52
total		271575 (4526.25 hours)	12664	95.34

and stably operated. No severe failure has occurred. Operation statistics during this period are listed in Table 1. An operation time of 4526 hours achieved during this period is about three times that during 1982 when operation started.

H. Kobayashi

1a. Injection system

The output current of the electron gun for the positron generator decreased below its certain limited value during operation in December 1987. The gun was immediately replaced with a new one. It took 41 hours of scheduled operation time to replace the electron gun, including baking the gun and its vacuum chamber and the conversion process of its oxide cathode. This gun was replaced again with a new one because of a decrease in its emission in July 1988. Although most of this replacement work had been done during scheduled maintenance time an additional 14 hours of scheduled operation time had to be used to complete the work.

The grid modulator assembly comprises a pulse generator for grid modulation and a contactor. Failure of the contactor for heater power of the electron gun occurred in January 1988 and the grid modulator assembly was replaced.

A. Asami

1b. Beam transport

Two remarkable problems occurred among the magnets powered by about 300 sets of power supplies. On March 26, the excitation coil burned out in the 30° bending magnet, which bends the 250 MeV beam from the positron generator into the PF 2.5 GeV linac. The cause turned out to be a misconnection of the cables for the interlock system (cooling-water, coil temperature).

On June 8, the positron pulsed solenoid failed. It had been used for about one year since April 1987. Though the coil, made of copper tube, had burst and much cooling-water overflowed, the damage to the accelerator could be avoided since it had been improved to be installed outside the accelerator vacuum. One possible cause of the breakdown was a deterioration of the coil insulator due to water-leakage from the connector as well as radiation damage. These coils were immediately replaced by spare ones.

A. Enomoto

1c. Microwave source

During the period between October 1987 and September 1988 the microwave system was operated stably with a total operating time of about 5000 hours.

The high-power klystron modulators were successfully operated. During this period 360 PFN capacitors of the improved type, which had been tested last year, were installed in the 18 modulators.

Seventeen high-power klystrons were replaced during this period. Sixteen of them had failed owing to internal arcing, and one was returned from the klystron gallery for retesting. Table 2 shows the operational performance of the tubes during the past 7 years up to July 1988. One hundred and eighteen tubes have been used since 1982 and 67 of them have failed during this period. Their averaged mean age was 4,500 hours and the mean time before failures (MTBF) was 13,500 hours. The mean lifetime of tubes is 11,400 hours.

An important factor concerning linac operation is the klystron fault rate, since faults lead to interruptions of the beam injection into the PF ring or the TRISTAN accumulation ring. In Table 3 the averaged fault rate of working tubes in each operating period of the recent 6 years is listed. The value of 1.0 per day for a tube is not so unsatisfactory.

Y. Saito

Table 3. Averaged fault rate and averaged applied voltage to klystrons.

period	Fault rate (/day*tube)	Applied voltage (kV)	Total operation (tube*day)
1982/8-1983/7	2.5	238	4470
1983/8-1984/7	1.6	242	4150
1984/8-1985/7	1.2	240	4420
1985/8-1986/7	1.0	238	5600
1986/8-1987/7	1.0	239	7740
1987/8-1988/7	1.0	240	9990

2. POSITRON INJECTION TO THE PF-RING

The positron generator has been used so far for TRISTAN, and only electron beams have been used for the Photon Factory. As for the electron beams in the storage ring for synchrotron radiation research, the instability of the beam is more or less inevitable arising from ion or charged dust trapped by the beam. Therefore, it

Table 2 Cumulative usage hours during the past years.
* Unused tubes are those which have never been used in the klystron gallery and will be used there.

Period	Total No. of tubes	Unused* No. of tubes	Failed No. of tubes	Failed Mean Age (hours)	Living No. of tubes	Living Mean Age (hours)	MTBF (hours)
up to '83/3	53	0	11	1,300	42	2,900	12,500
up to '84/3	66	3	20	2,300	43	4,200	11,200
up to '85/3	79	9	25	3,100	45	5,800	13,600
up to '86/3	91	14	32	4,000	45	7,500	14,400
up to '87/3	106	9	47	4,300	50	8,600	13,400
up to '88/3	120	4	67	4,500	49	10,900	12,400
up to '88/7	120	2	67	4,500	51	11,400	13,500

has been planned to use positrons instead of electrons in the PF ring in order to completely overcome this difficulty.

Recently, positrons were actually accumulated in the PF storage ring, and synchrotron radiation from the beam was test used for research, aiming at obtaining more stable lights from positrons than those from electrons. One of the problems was that the time required for accumulating the beam was too long, e.g., it took ~ 90 minutes to accumulate 300 mA. In order to make this time shorter, it is necessary to increase the total charge, which may be achieved by using a beam with a longer pulse width. In the acceleration of a certain amount of charge, it is usually more advantageous to use a longer pulse as long as it is allowable for the rf pulse width, because a lower peak current weakens the space-charge effect as well as the wake-field effect.

At first, therefore, a long pulse beam of 500 ns width was tested; it turned out, however, that the measurement of the positron beam was difficult because of the very low peak current. Then, 20 and 40 ns beams were chosen for the test and achieved good results. Meanwhile, for TRISATN, a 4 ns beam is necessary which is finally reduced to less than 2 ns by a subharmonic buncher. Therefore, a selection system is necessary to switch over these two beams remotely.

A long pulse pulser was prepared in addition to the short one used so far. A beam width selection system has been made to exchange the beams by selecting one of the pulsers with a coaxial switch which is located between the electron gun and the pulsers, as shown in Fig. 1. Selection signals are tansferred through optical fibers which are also used to isolate the gun at high voltage from the ground potential.

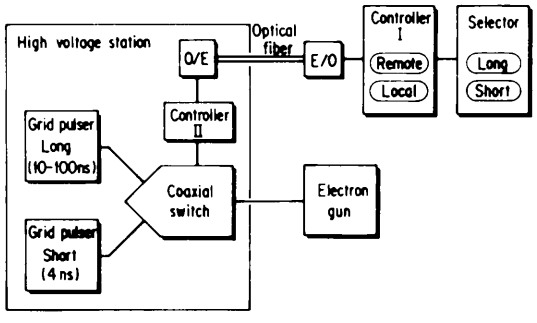

Fig. 1 Block diagram of the beam width selection system.

The result of the 40 ns beams is summarized in Fig. 2. The positron beam current which was finally obtained is roughly proportional to the injection current from the gun for any case, and half of the positrons is spilled in the 30° beam transport line as in the 2 ns beam.

Upon using this beam, positron injection into the PF ring was attempted after matching the beam optics of the transport line from the 2.5 GeV linac to the ring. The beam had an energy spread of ±0.25 % and an emittance of 1 ~ 8 × 10^{-6} m·rad, which are similar to those of the 2 ns beam. An injection rate of 0.2 ~ 0.25 mA/s was obtained, which was larger than 0.05 ~ 0.07 mA/s for a 2 ns beam by a factor of three to four.

S. Ohsawa

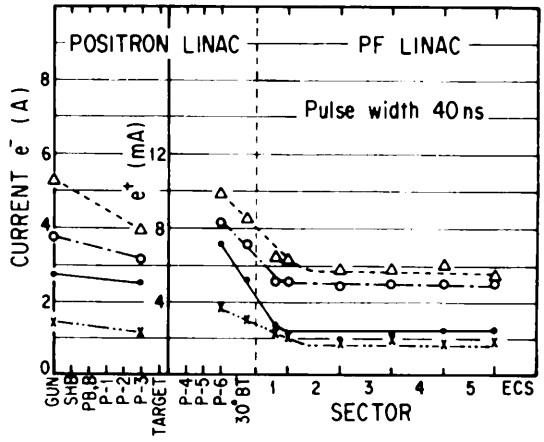

Fig. 2 Beam currents along the accelerator for a 40 ns beam.

c. PROGRESS AND IMPROVEMENTS

1. INJECTION SYSTEM

1a. Reinforcement of an rf Power to the Injection Unit

In FY1986, the waveguide system of the injector was modified from the one shown in Fig. 3(a) to that in Fig. 3(b), and an improvement was made in obtaining higher acceleration currents. However, the electron-positron conversion efficiency decreased slightly (0.05%), probably because of a decrease in the the electron energy, as described in the previous PF activity report.

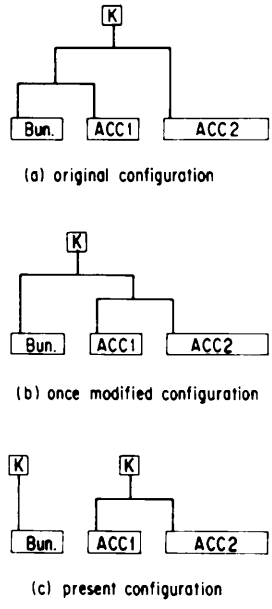

Fig. 3 Modification of the injection rf system.

Therefore, it was decided to reinforce the rf power to the injector, as shown in Fig. 3(c), and a new high-power klystron and the associated equipment were prepared and installed. This was completed in April, 1988, and test operation was subsequently carried out. The results are summarized in Table 4, where the electron beam current from the gun, that just before the positron producing target, and the positron current at the end of the positron generator are listed.

Table 4 Comparison of e^-/e^+ current

	Before Modification	After Modification
Gun	8.6 A	8.2 A
Targer (e^-)	10.0 A	10.4 A
Generator End (e^+)	21.0 mA	31.2 mA
e^+/e^-	0.21 %	0.30 %

With this reinforcement a considerable improvement was achieved. The increase in the conversion ratio was more than expected from a simple energy increase, and was probably due to an improvement in the beam emittance. Beam waveforms observed in the test are shown in Figs. 4(a) to 4(c).

A. Asami

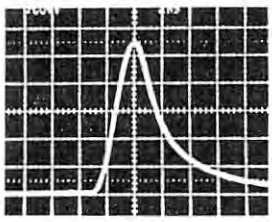

(a) gun (e^-), 8.2 A

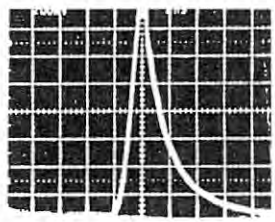

(b) target (e^-), 10.4 A

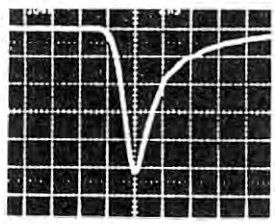

(c) generator end (e^+), 31.2 mA

Fig. 4 Electron and positron beam waveforms.

1b. Control of the Gun System

One of the crucial problems for the gun vacuum system is to maintain a good vacuum by confidential operation of vacuum components, since the characteristic of oxide coated guns are very sensitive to any deterioration of the vacuum. Under this connection, a vacuum interlock system was introduced utilizing a programmable sequencer, which is rapidly developing now in respect to factory automation.

The system consists of two parts: a control unit and a power unit, which assures their confidential operations against environmental noise. The control unit reads the various status of vacuum components: two kinds of vacuum gauges, four kinds of vacuum pumps, and six gate valves, and gives the power unit appropriate instructions to protect the gun vacuum. The power unit supplies power to gate valves and has a hard interlock circuit for a power shutdown.

The program on the sequencer was elaborated by making use of the simulator of a gun system, which is designed to receive and send all kinds of simulated signals of the system. The whole system has worked well without any problems.

The high-voltage station involves power units for the gun heater, bias, and pulse voltages, which are remote-controlled to adjust an emission current of the gun. The analogue voltage on the high-voltage station is transformed to frequency. Then, after optical transmission between the high-voltage station and the ground based equipments, it is retransformed to a voltage which is read out by microcomputer.

Two systems are connected through a factory microcomputer (FC-9801V), which collects the input data from both systems and displays the information of the vacuum status and the high-voltage station status on a CRT. At present, the CRT image is transmitted as a video signal to the linac main control room. In the near future, it will be connected to the computer network for linac control.

Y. Ogawa

1c. Prebuncher for the 2.5 GeV Electron Linac

A new prebuncher was manufactured and installed in 1987 for replacing the old one in which a slow leakage of air had been found. It is an accelerating-type prebuncher of traveling waves and 2/3 π mode, which is the same as the old one. This type was adopted since it is advantageous in accelerating electrons while making bunches that prevent a deterioration of the beam quality, such as bunch length and emittance. A fundamental policy of the design was that when using the new prebuncher with the buncher, it must be possible to achieve the same beam characteristics as before. Several improvements satisfying the requirement were made: the cavity number was increased from 6 to 7 including input and output couplers for easier rf tuning of the couplers, and the β-value (phase velocity/ speed of light) was also changed from 0.5 to 0.6 to enable an increase of the gun voltage in the future. The new prebuncher was made by the electroplating method instead of the demountable type as the old one.

A typical example of the beam trajectory with the final a and b values is shown in Fig. 5. In the calculation, the prebuncher, drift space and buncher were included. The beam phase at the output of the buncher is plotted as a function of the beam phase at the input in Fig. 6. The result of the calculation indicates that 2/3 of the electrons are concentrated in a small bunch less than $\pm$ 2°. Cavity dimensions are listed in Table 5. The inner diameter of the

disk was made larger than before since larger diameter weaker the wake field effect.

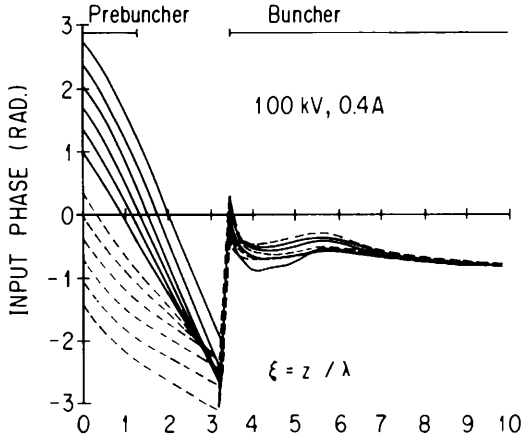

Fig. 5 A typical example of the beam bunching in the new prebuncher and buncher including a drift space between them.

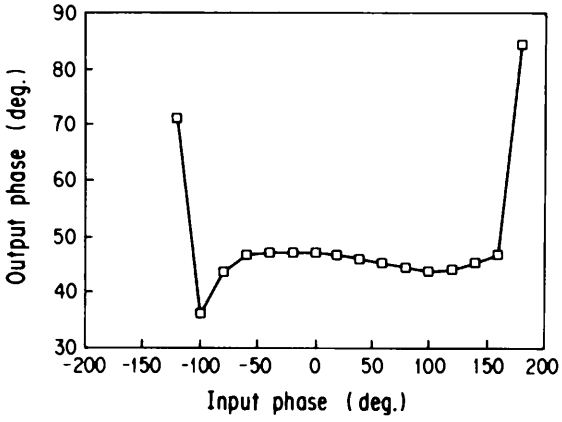

Fig. 6 Input-output phase relationship for a bunched electron beam. The phase of the electron is defined with respect to the rf wave in the prebuncher or buncher.

Table 5. The cavity dimensions of the new prebuncher (2a and 2b) in addition to parameters α and β_w used in beam bunching calculations. 2a: inner diameter of the disk, 2b: inner diameter of the cavity, α: $eE\lambda/m_0c$, β_w: the rf phase velocity/ the speed of light c.

No.	α	β_w	2a	2b
1	0.034	0.6		
2	0.036	0.6	29.48	86.703
3	0.038	0.6	28.80	86.372
4	0.040	0.6	28.15	86.071
5	0.042	0.6	27.56	85.793
6	0.044	0.6	26.97	85.526
7	0.046	0.6		

Figure 7 shows beam currents measured along the 2.5 GeV linac. This result was obtained using the new prebuncher with a micro-second beam. The capture efficiency, defined as the ratio of accelerated beam current to anode current from the gun, is 67 % as expected from the beam trajectory calculation.

S. Ohsawa

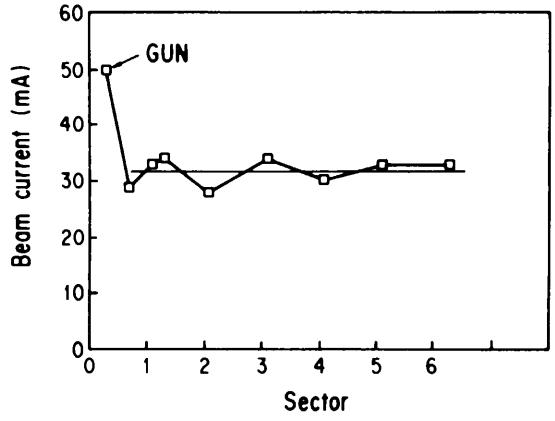

Fig.7 Currents of a micro-second beam measured along the 2.5 GeV linac.

1d. New Gun

The electron gun of the positron generator has a problem regarding its lifetime. In order to overcome this difficulty, a new type of electron gun was manufactured and is now being tested at a test bench. It has a dispenser cathode which has an advantage in that the emission current is not so sensitive to residual gases in the vacuum, as compared with the oxide-coated cathode now being used in the positron generator. In addition, it also has the feature that the relatively low grid pulse voltage makes it possible to draw a high current because of the short grid-cathode distance. This feature is important, especially in obtaining a beam as short as 4 ns from the gun for TRISTAN.

Figure 8 shows the electron trajectory calculated by the program of W. B. Hermannsfeldt. In the calculation the emission current is assumed to be 9 A, a typical value obtained at present. The calculation then predicts an emittance of $1.69 \times 10^{-2}\ \pi$ (m_0c·cm). When the gun is operated in the space-charge limited region, an maximum anode current would exceed 20 A at an injection voltage of 150 kV.

S. Ohsawa

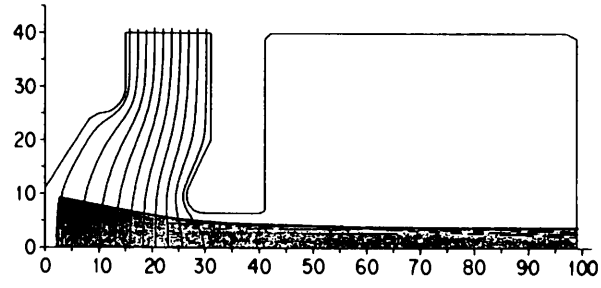

Fig. 8 Computer plot of the gun optics at 150 keV, showing an equipotential surface and beam focusing pattern. The shaded area denotes the electron beam. The emission current is limited to 9 A in the calculation.

1e. Development of a Grid Pulser

The development of a grid pulser utilizing

a hybrid IC has been achieved for the electron gun, and has shown that a pulser with a hybrid IC of 2N222A transistors has shorter rise and fall times than that with the same transistors of the can-type. However, the output voltage obtained with this transistor was limited to a relatively low value.

Recently, we obtained 2N5551 chip transistors, which have a higher avalanche voltage than the 2N222A. By using a hybrid IC made of these 2N5551 transistors, the output voltage was increased by about 50 percent compared to the provious one with the same number of stages. The output pulse waveform of the pulser is shown in Fig. 9, and the resulting electron beam current was 12 A at 150 kV as shown in Fig. 10. The hybrid IC is shown in Fig. 11.

Y. Otake

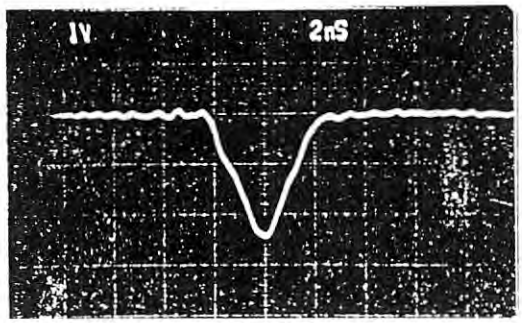

Fig. 9 Output pulse waveform of the grid pulser utilizing a hybrid IC of 2N5551 transistors. A peak voltage of 240 V is obtained with an input impedance of 12.5 Ohm.

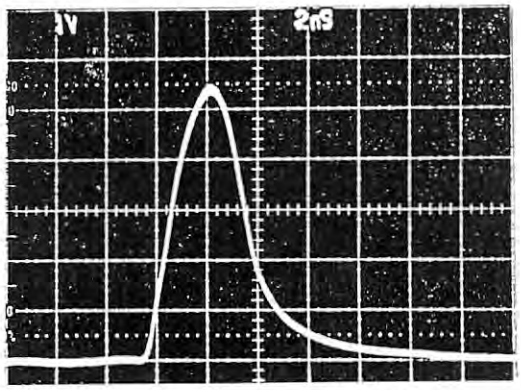

Fig. 10 Electron beam current of the gun. A maximum peak current of 12 A at 150kV of gun voltage is obtained by using a grid pulser with a hybrid IC.

Fig. 11 Hybrid IC made of 2N5551 transistors developed for the grid pulser.

2. ACCELERATOR GUIDES AND BEAM TRANSPORT

2a. Beam Study Using Streak-Camera System

A streak-camera system is a powerful tool for real-time temporal diagnostics of the accelerated electron/positron beam in the range between a few picoseconds and several nanoseconds.

Our streak-camera system has been used only at the end of the positron generator to investigate pulse structures of the high-current primary electron beam (200 MeV, 2 ns, 10 A) and the positron beam (250 MeV, 2 ns, 20-30 mA). Figure 12 shows the configuration of the equipments. The pulse structure is analyzed by measuring Cherenkov light radiated by the electron/positron beam in the air between the accelerator end window and a surface mirror. The Cherenkov angle of the light is about 1.3°. An optical system with surface mirrors and an achromatic lens collects a fraction of the light into the streak camera (HAMAMATSU C1370) with a maximum time-resolution of 2 ps.

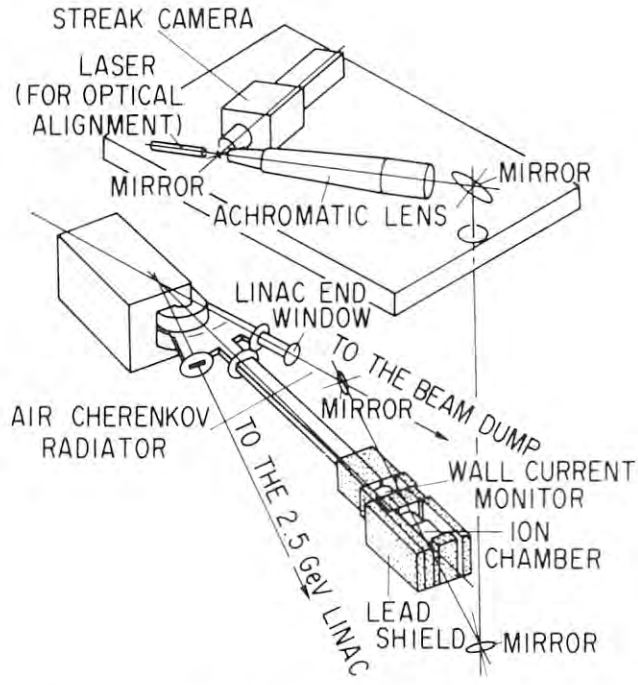

Fig. 12 Equipment for the sreak-camera and energy analyzing systems.

Figure 13 shows an example of a measurement representing the waveform for one of the positron beam pulses accelerated at an repetition rate of 25 Hz. The pulse includes positron bunches (indicated by e^+ in the figure) at intervals of 350 ps which is the rf cycle time of the acceleration field. It should be noticed that electron bunches (e^-) are also involved between the positron bunches.

Among the positrons and electrons which emerge from the positron radiator, only those matching the momentum acceptance ($P_0 \pm \delta P$) of the positron focusing coil may enter the following accelerator section. The electrons are at first

out of phase with the acceleration field, but become in phase as well as the positrons after being decelerated and slipping by 180°.

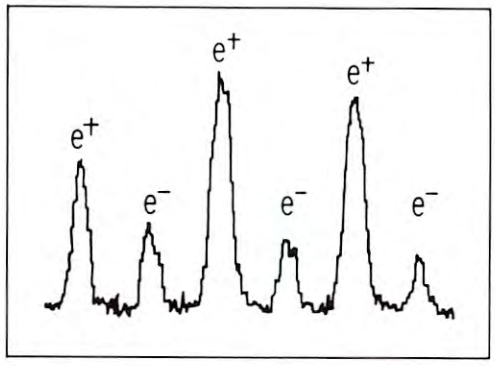

Fig. 13 Display of an analyzed streak image for a 2ns positron beam pulse.

The current ratio between the positrons and electrons depends on the momentum acceptance of the transport system, since the electron momentum is smaller than the positron momentum by an amount of about $2P_0$ after the phase slippage. If the ratio of the electron mixing is high, it is a troublesome problem for beam adjustments because it reduces the signal of positrons from electromagnetic monitors. As shown in Fig. 14, the energy spectra for both of the positron beam and the mixed electron beam were also measured with a bending magnet at the end of the positron generator; the electron energy is lower by about 24 MeV and the current is in the order of 10 percent of the positron beam.

A. Enomoto

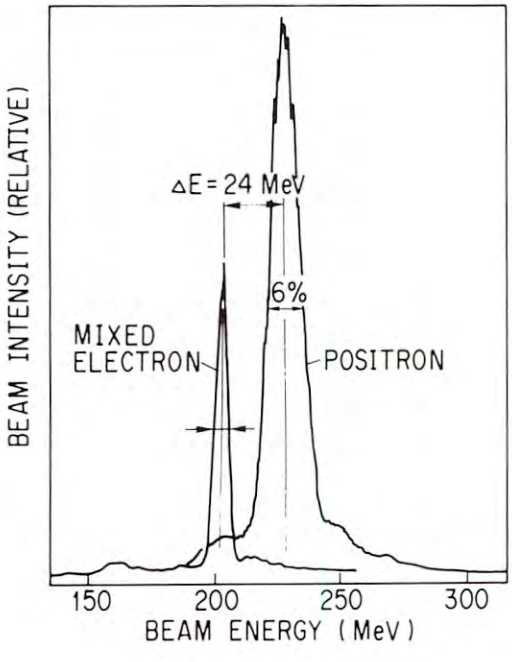

Fig. 14 Energy spectra of the positron and mixed electron beams.

2b. Water-Leakage from the Accelerator Guides

Three accelerator guides had water leakage trouble from the cooling-water jackets (accelerator guides No.2-8#3, 3-6#1 and 5-4#3, which had been used since 1981). These guides were replaced with new ones during the 1987 summer shutdown. The leakage had occurred at the electron-beam-welded (EBW) part of the cooling water jacket as shown in Fig. 15.

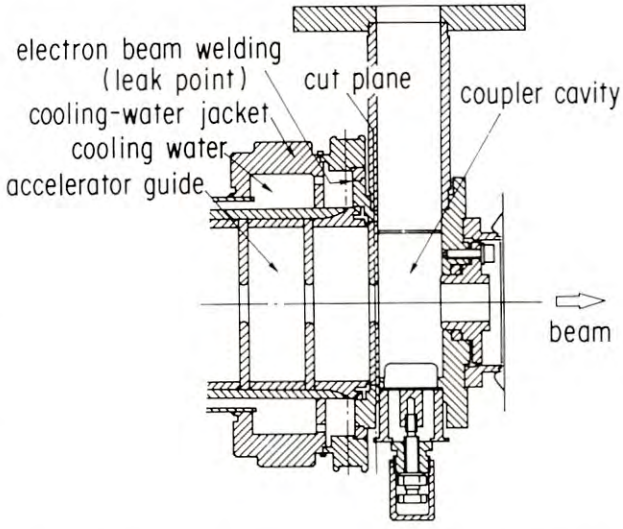

Fig. 15 Cross-sectional view of accelerator guides.

A thorough investigation was made by cutting a piece (indicated by dash-dotted line) out of the guide. It turned out that the welding thickness at the leakage point was not sufficient because the axis of the EBW missed the correct line. Figure 16 shows examples of normal and insufficient welding, respectively.

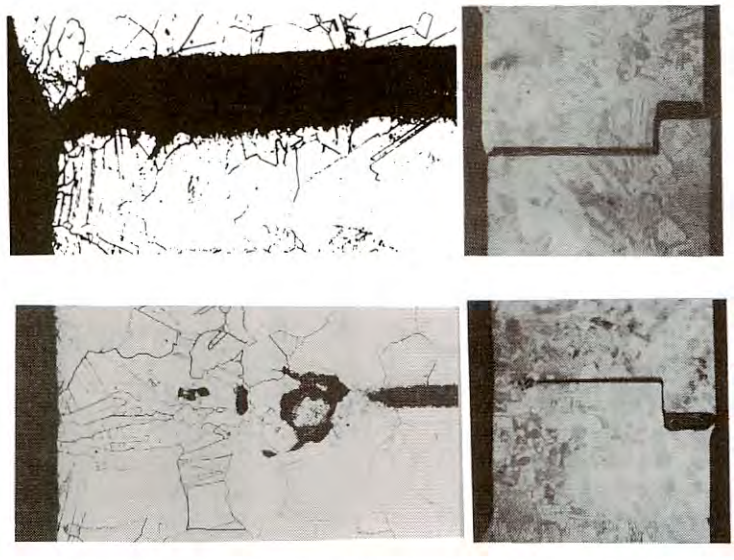

Fig. 16 Magnified cross section of the electron beam welding point: insufficient weld (upper picture); normal weld (lower).

In January 1988, additional water leakages were found at 16 parts in 12 guides. Since they were very small, these guides have not been repaired. No leakage has been found in those used in the positron generator.

A. Enomoto

3. MICROWAVE SOURCE

3a. Klystron Failure Due to Internal Arcing

One hundred and twenty klystrons have been used in the klystron gallery as the microwave source of the PF linac up to July 1988. Their operational status corresponding to the respective tube producting years is shown in Table 6. Up to now, sixty-seven tubes have been replaced by new ones. The causes of failures were mostly due to internal arcing (53 tubes) and window punctures (9 tubes). The window failures could be reduced by research and development since 1983 (Photon Factory Activity Reports of 1984/1985 and 1986). Research concerning the internal arcing phenomena has been also carried out during these several years. Recently, improvements of the electron gun assembly in the tube have been applied and the number of failed tubes due to internal arcing has become smaller. In this report, a brief outline of the R & D for the internal arcing of the klystron is described.

The mean age of the arcing failure tubes is about several thousand hours, and about twenty tubes installed in the gallery must be replaced by new ones every year. Therefore, klystron failure due to internal arcing is a serious problem for accelerator operation and maintenance. To investigate the internal arcing phenomena some failed tubes were opened. Figure 17 shows a schematic drawing of the electron gun assembly of the tube. An oxide barium cathode of 80 mm in diameter is used, and the focus and anode electrode materials are SUS 316L (Vac. Melt) and OFC-Class 1 (ASTM F-68), respectively. The maximum electric field strength on the electrode surface is about 270 kV/cm at an applied voltage of 260 kV. The electrodes of the failed tube are shown in Figs. 18 and 19. Arc marks were found on the focus and the anode electrodes. It was noticeable that the copper anode was contaminated by deposited films which were flaky and of white coloring. These deposited films are barium compounds evaporated from oxide materials of the cathode. Also on the focus electrode, a thin layer of such contamination was observed, though not so flaky or much amount. This is probably due to the lower sticking coefficient of cathode material on the hot focus electrode.

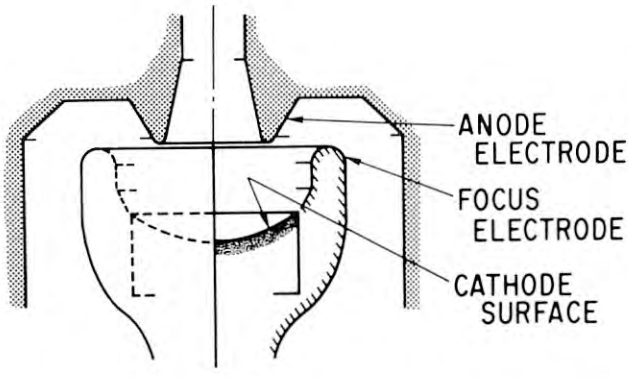

Fig. 17 Schematic drawing of the klystron gun assembly.

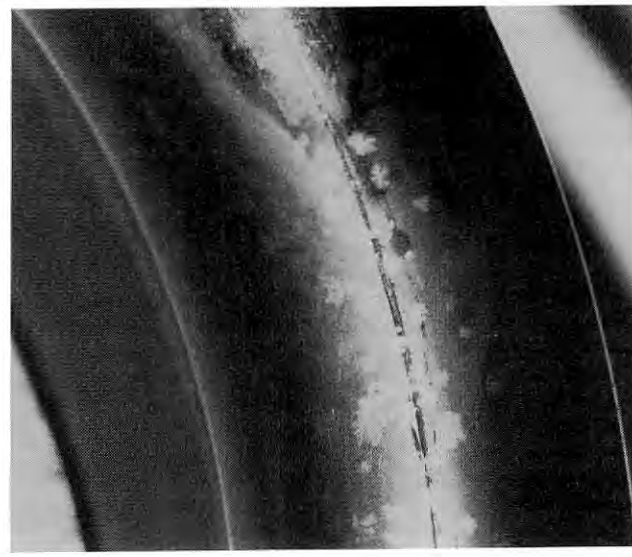

Fig. 18 Arc marks on the focus electrode of a failed klystron.

Fig. 19 Contaminated anode electrode of a failed klystron.

Table 6 Cumulative status of klystrons up to July 1988 according to the year of production

* Unused tubes are those which have never been used in the klystron gallery and will be used there.

** STB (stand by) tubes are those which have been used in the klystron gallery.

*** The averaged fault rate and contribution to the total operating tube*day is counted during the period August 1987-July 1988.

Year of production	Total no. of tubes	Unused*	Living					Failed					Fault rate*** (per day per tube)	Contrb.*** to total opert.
		No. of tubes	No. of tubes	Mean Age (hours)	No. of working tubes		No. of STB** tubes	No. of tubes	Mean Age (hours)	Causes				
					PF	Positron				Arc	Wind.	Other		
1979	4	0	0	-----	0	0	0	4	3902	2	1	1	----	0 %
1980	20	0	4	21192	3	0	1	16	7124	9	5	2	2.6	7.4
1981	20	0	10	20925	9	0	1	10	4663	6	2	2	0.8	18.5
1982	9	0	3	19292	2	0	1	6	5785	5	1	0	2.5	4.2
1983	13	0	10	16195	9	1	0	3	6019	3	0	0	1.2	20.5
1984	13	1	5	9652	3	2	0	7	3971	7	0	0	0.5	11.1
1985	12	1	5	9928	5	0	0	6	4750	6	0	0	0.5	11.9
1986	15	0	3	6539	3	0	0	12	2421	12	0	0	0.7	10.3
1987	14	0	11	2448	7	4	0	3	1502	3	3	0	0.7	16.1
	120	2	51	106171	41	7	3	67	40137	53	9	5	1.0	9994 tube*day

Electrode contamination is the most likely cause of arcing in a tube of ultra-high-vacuum. The arcing mechanism between the focus and anode electrodes is considered to be as follows. Electrons are thermally emitted from the barium compound deposited on the focus electrode, and impinge on the anode electrode. By this electron bombardment the contamination of barium compounds and adsorbed gases on the anode electrode are stimulated to be ionized or desorbed. The ionized molecules then impinge on the focus electrode and produce secondary electron emission. Successively continuing and enhancing multiplication of electrons and ions, these phenomena lead to internal arcing.

Though having the merit of its low working temperature (about 850°C), the barium oxide cathode is necessary to be proceeded by heating in the tube during the production process as called conversion. This would make unfavorable contaminations of gases or barium compounds on the electrodes. On the contrary, having a higher working temperature (about 1050°C), the barium impregnated cathode (dispenser cathode) can be prefired so as to evaporate any excess amount of barium compounds from the cathode materials in another vacuum chamber before installation in the tube. Therefore, in a klystron with the barium impregnated cathode contamination of the electrodes is expected to be reduced and, consequently, the occurrence of the arcing between the electrodes would become harder.

Six tubes with the barium-impregnated cathode of scandium mixed type were produced in 1987 and also tested in the gallery during a period of three thousand hours. Their high-voltage fault rate was about 0.05/day, which is distinguishably less than that of the tubes with the oxide cathode (1.0/day). It is also observed that the amount of x-ray radiation from the impregnated cathode tube is lower than that from the oxide cathode tube (x-rays in the direction of electron gun assembly). This indicates that electron bombardment on the anode is reduced as a result of less contamination of the focus electrode. Therefore, the barium impregnated cathode is considered to have a better performance for tubes compared with those with the oxide cathode.

Y. Saito

3b. Klystron rf Waveform Recording System

The spread and drift of the accelerated beam energy strongly depend on the amplitude and phase stabilities of microwaves traveling in accelerator guides. Therefore, it is quite important for stable beam injection into the storage rings to detect unfavorable variations in the rf system quickly. Periodical monitoring of the amplitude and phase waveforms of the klystron rf power is actually one part of the diagnosis for an rf source and enables prediction of any serious trouble.

In previous operation, the rf pulse shapes were observed at subcontrol rooms or just beside the rf sources, so that the engineer maintaining the rf system was obliged to spend a long time recording all the waves. He had to prepare a measuring system and trail it along the long linac in order to take pictures of rf wave envelopes. This troublesome work, which had been done at the end of every operational period of the linac, was useful for making sure of the reappearance of rf power at the next start of the period. However, it did not help to find a momentary failure and also to follow slow drifts during the long term.

Our new system has been designed to solve the above problems and has the following features:

(1) Three kinds of waveforms, i.e. envelopes of forward and reflected rf power detected at output port of a klystron and phase of accelerating rf waves, are able to be observed and recorded automatically at the main control room. The recorded data is storaged in a hard disk on a LAN (Local Area Network).
(2) The memorized waveforms can be displayed and compared on any CRT connected to the LAN.
(3) A hardcopy of the waveforms can be plotted out.

Especially the second function greatly supports troubleshoot of the rf system.

A block diagram of the system is given in Fig. 20. The forward and reflected waves are picked up at directional couplers (-60 dB) attached to an output port of a klystron. Both of the rf signals are transmitted through low-loss rf cables to a circuit which measures the rf pulse shapes by crystal detectors.

The rf envelope signals from klystron amplifiers are relayed at respective subcontrol rooms. The pair signals for a concerned klystron are selected by coaxial switches. A phasing unit in a subcontrol room detects the relative phase of a concerned rf signal from an acceleration guide by comparing it with a reference rf signal (cw) supplied from a subbooster amplifier. These three signals, which express forward(P_f), reflected(P_b) and phase(ϕ) waveforms, are amplified by 10 and transmitted to the main control room.

In the main control room three coaxial switches select P_f, P_b and ϕ signals. A digital storagescope (TEK 2430A) is installed to record and analyze the pulse shapes of the selected signals. A workstation (FM-R50) is interfaced with the storagescope and an XY-plotter through GP-IB and RS-232C, respectively. This workstation obtains data from the storagescope and outputs data to the plotter in response to requests from another workstation. The collected data are filed in a hard disk under the server workstation. Memorized previous waveforms can be expressed on a computer-display linked with the LAN. For watching an rf power a CCD videocamera is attached to the CRT of the scope, so that the realtime image of a waveform can be monitored on any videodisplay connected to a CATV line in the linac building.

For the recording of waveforms, at first an operator should select "Klystron Rf Monitor" from a function menu on a CRT built in a opera

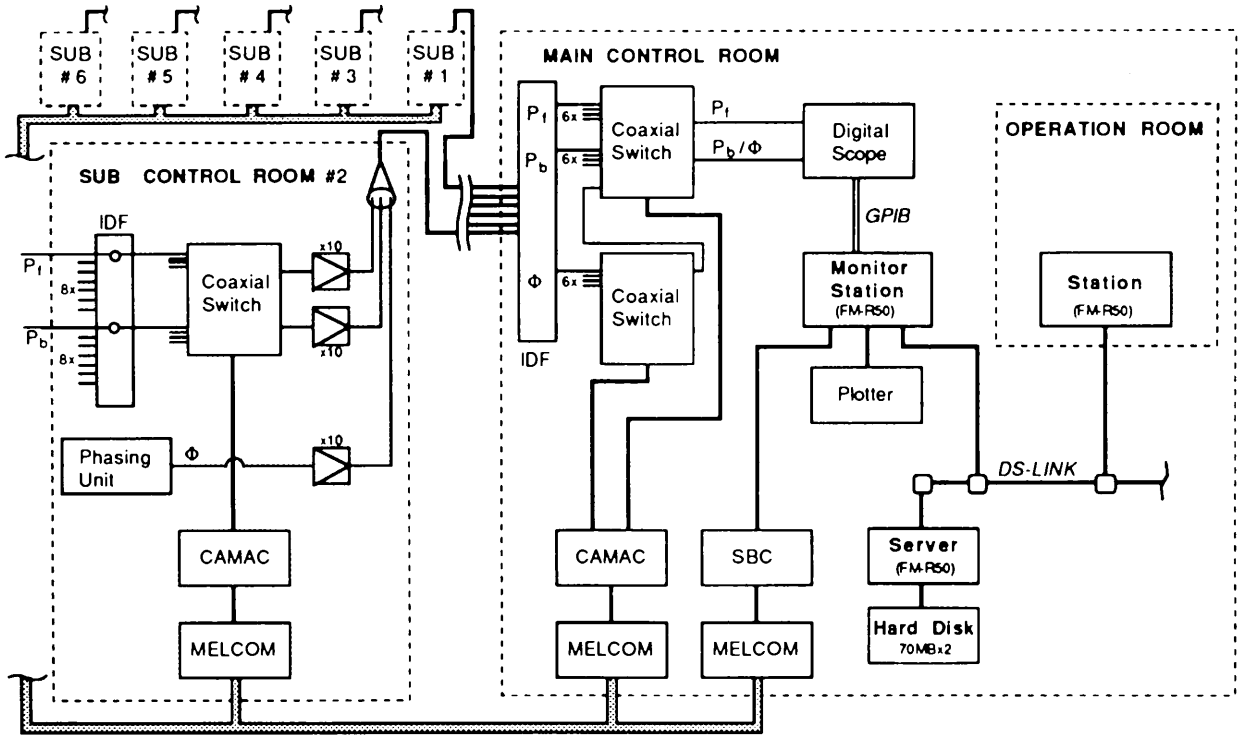

Fig. 20 Block diagram of klystron rf recording system.

tor's console. The first screen shows four icons which express recording, playback, plotter and watching, respectively. By touching the recording icon a second screen guides the operator to select either a sector of the klystrons or all klystrons. A workstation in the console sends a message, which orders the recording of the waveforms, to the rf monitor workstation.

The monitor workstation receiving the message starts the following procedure of recording. Messages to control the coaxial switches are sent to LOOP-3 for selecting P_f and ϕ signals. The selected phasing unit is requested to adjust its reference phase shifter according to the last phasing data. The storagescope is controlled to set the vertical gains, horizontal time base and trigger delay. Both of the signals are digitized and transferred to the workstation. Next, a P_b is selected and processed. Finally, all of the data are saved in a file located on the hard disk. This procedure is repeated for all klystrons of a selected sector.

The storaged data sets are managed by a index file which contains all the names of waveform files. By referring to the index file a workstation can quickly determine whether the hard disk has the concerned data.

This recording procedure is executed automatically at 0:00 every day for periodical monitoring of klystron rf waves.

An operator can select the playback of previous waveforms, plotting out, or realtime watching of the signals by touching the icons on the first screen (mentioned in the above section). In the playback mode six waveforms can be compared on the same screen. P_f and P_b signals can also be magnified by 1.5 on another screen. Figure 21 shows an example of a screen displaying rf envelopes. If the plotter mode is accessed the monitor workstation receives a command through the LAN and executes it to drive the plotter. The waveforms of all klystrons of a selected sector are plotted out on two sheets of paper.

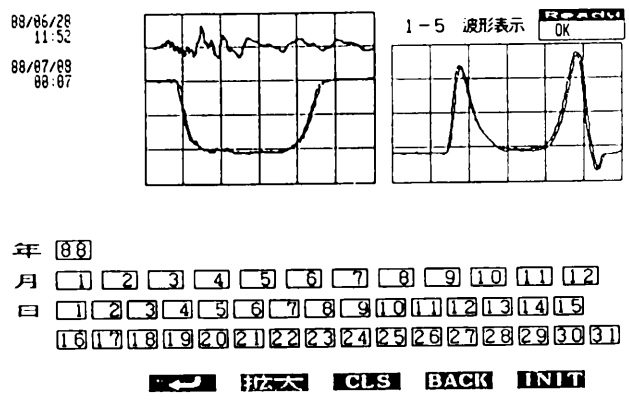

Fig. 21 An example of a screen displaying waveforms. Left waveforms express P_b and P_f. Right one is the ϕ signal.

The watching mode is prepared in order to find any irregular or momentary failure of the

rf power. The monitor workstation only selects signals and adjusts the storagescope. Until it receives a next command the realtime pulse shapes of both P_f and ϕ are kept on the CRT of the scope. An operator can observe them by watching a videodisplay.

H. Hanaki

4. CONTROL

4a. Installation of a New Computer for the Console Station

The linac control system comprises two console stations for operators, seven sub-control stations, hundreds of local controllers for accelerator devices and fiber optic networks between them. When this system was designed, it was intended that it would act as a fast multiplexer between local controllers for linac devices and the main-control stations for operators. So far, it has succeeded and operators have been able to manipulate devices within a reasonable response time.

However, requirements for accelerator controls are increasing. For example, monitoring, history logging and statistical processing of accelerator parameters and communications between other data handling computers are required. In order to meet these requirements the resource capabilities of the current system were too restricted.

The introduction of a new station was planned so as to enhance the console station functions. It was required that the new machine could communicate with local devices and acquire all necessary information in the linac as well as providing a large memory and disk space for statistical and logging software.

A new console station (Mitsubishi's MX3000) was directly connected to one of the main console stations through parallel and serial interfaces. This computer has real-time processing functions while the user interface to the operating system is Unix system V. It can communicate with other systems with TCP/IP, BSC and TTY protocols. Software to emulate the environment of a console station were developed and several software packages are already in operation.

One of the new programs, for example, is for touch panels on the operator's console. In parallel with the project of software development, new touch panels were designed. On the operator's console there are 9-inch touch panels mainly for controls, and 20-inch touch panels primarily for status display. One of the old capacity-sensitive 9-inch panels was replaced with a resistive plate 12-inch panel with a plasma display. Control software libraries for new panels were developed and installed on personal computers. Software to control the linac has been developed for the new console station. Programs were written so as to be independent of hardware configurations of the station, touch panels and accelerator equipments.

Currently, these programs on the new console station are operating well. During the next year, information services of linac operational parameters to groups other than the control group through the MX3000 will be started. It will provide new features for the operator's console.

K. Furukawa

Light Source Department

Meteorological changes distort the PF building.

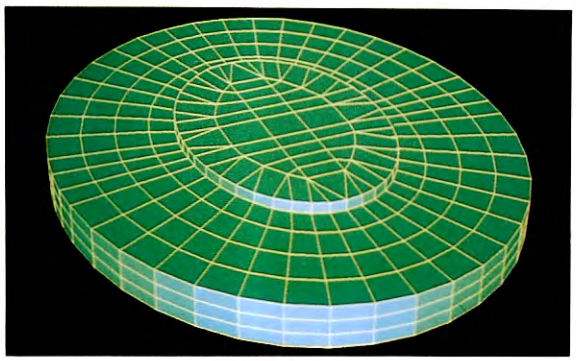

Undistorted

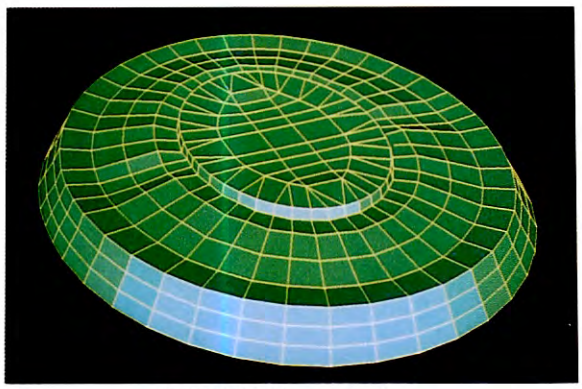

6:00 A.M. Contracted

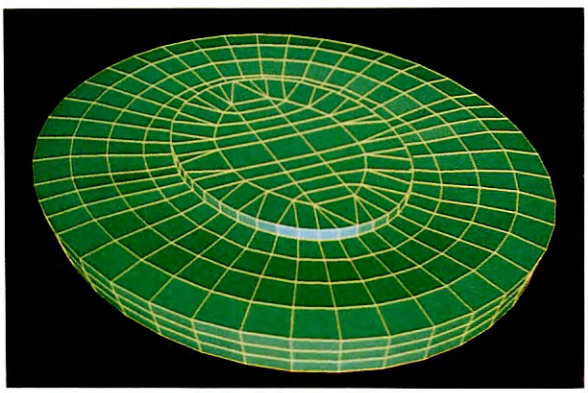

3:00 P.M. Expanded

(Continued to the back.)

Light Source Department title page:

When the weather changes, the Photon Factory building expands or contracts in response. This distortion changes the dimension of the storage ring and the locus of the orbiting particles, thus affecting the photon beams.

A computer simulation, which was used to calculate the thermal distortion of the building, provided useful information. To minimize distortion in the future, we will insulate the top of the roof, rather than underneath as is usually done. In the illustrations, the distortion is magnified by about 1000 times. (The simulated illustrations were prepared courtesy of Shimizu Construction Co.)

LIGHT SOURCE DEPARTMENT

A. INTRODUCTION

The PF ring is a 2.5 GeV electron (or positron) storage ring fully dedicated to synchrotron radiation researches. The ring was commissioned in March 1982, and since then it has been operated quite stably for over six years. The upgrowth of the ring is well shown in Fig. 1.

The Light Source Department was very busy in the fiscal year 1987. Extra budget of about 6×10^8 yen was funded for the construction of three insertion devices including the beam channels. One is a new superconducting vertical wiggler which is able to inject electrons (or positrons) into the ring with neither changing its vertical position nor re-exciting coils. The second is an EMPW which is a multipole wiggler/undulator generating elliptically polarized synchrotron radiation and will be installed into the PF ring. The third is an EMPW which has already been inserted into the Accumulation Ring of TRISTAN.

During the summer shutdown in 1987, four RF cavities were renovated in the way described in the previous Activity Report. More than 100 kW of RF power can be fed to each single cell cavity. At the same time, damping couplers were taken out from the ports of cavities #1, #2 and #4. Each cavity port was covered with a properly shaped blank cap. This renovation perfectly cured longitudinal coupled-bunch instabilities caused by higher-order-mode resonances of the cavities as described in Section C-2. However, the other longitudinal coupled-bunch instabilities were still observed. Spectrum analysis of bunched beams showed that these instabilities were caused by wake fields induced in some parts of the vacuum chambers.

In December 1987, the ring was operated at the energy of 1.5 GeV to examine whether the ring can generate high-brilliant UV synchrotron radiation or not. At low stored currents, the horizontal beam size was reduced by 20% compared to that in the 2.5 GeV operation. However, at 200 mA, the beam size increased by 70% compared to that in the 2.5 GeV operation as described in Section B-1. The cause was found to be the same longitudinal coupled-bunch instabilities related to wake fields. The conversion of the ring into a VUV-ring would therefore require that the vacuum-chamber cross section be much smoother.

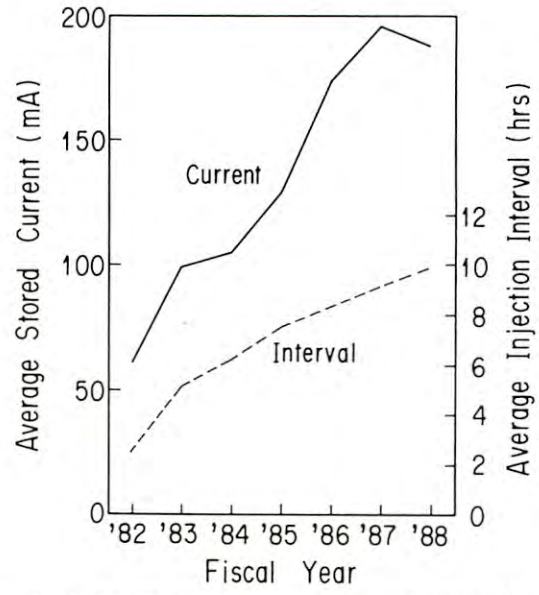

Fig. 1 Average stored current and injection interval v.s. fiscal years.

Since March 1988, operation of positron storage has been tried several times. On July 11, the ring was operated for user time with positrons instead of electrons. We observed that two-stream instability caused by ion trapping perfectly disappeared and the deterioration of beam lifetime caused by dust or micro-particle trapping did not occur.

Table 1 Operational statistics during user time from May 17 until July 30, 1988. Comparison between electron-storage and positron-storage.

	Electron May 17-July 16	Positron July 18-July 30
Scheduled time (hrs)	905.7	238.2
Time used by users : T (hrs)	810.6	221.6
Time used for beam storage (hrs)	65.7	15.2
Integrated current during T (A·hr)	155.5	38.4
Average current during T (mA)	191.8	173.3
Number of injection	93	11
Average injection interval (hrs)	8.7	20.1
Normalized $I_0\tau_p$	0.910	1.015

Table 1 shows the operational statistics of user time from May 16 to July 31 for the comparison between electron and positron storage. From this statistics, we can see that "the normalized $I_0\tau_p$" (τ_p is called "the practical beam lifetime") in the positron storage operation is 1.11 times as long as that in the electron storage operation. Details will be described in Section B-2.

In the previous Report, it was described that the motion of the vertical beam position was correlated to the climatic environment such as atmospheric temperature around the Light Source building and sunlight shining on its roof. A computer simulation made by Shimizu Construction Co. Ltd. shows that temperature change of the roof gives a distortion to the Light Source building. Temperature measurement of the roof was made by covering a part of the roof with urethane foam. The results show that 50 mm-thick urethane-foam plate is enough to decrease the temperature change of the roof. Details will be described in Section C-2.

K. Huke

B. OPERATIONS

1. 1.5 GeV OPERATION

As the horizontal emittance ε_x is proportional to the square of the beam energy, the emittance will be 46 nm·rad at 1.5 GeV, which is smaller by a factor of 2.8 than that at 2.5 GeV. Brilliance of the photon beam in VUV region was expected to become eight times higher at 1.5 GeV.

The storage ring was operated at 1.5 GeV on December 14, 1987. Below 10 mA of stored current, the horizontal beam size σ_x was reduced to 80 % of that at 2.5 GeV and the vertical beam size to 64 %. The resonance frequencies with the high coupling impedances in the RF cavities were carefully trimmed to suppress the instabilities as described in Section C-2. However, at a higher stored current of 200 mA, the horizontal beam size was enlarged to be 1.7 times larger than that at 10 mA, as shown in Fig. 2. The mechanism of this horizontal beam blow-up was found by a spectrum analysis of beam signal; coupled-bunch instabilities were caused by the structure of the vacuum chambers having the high-frequency resonances above 1.5 GHz with low Q-value. Because of widening of the energy deviation by the instabilities, the beam size σ_x was enlarged. Here, the σ_x is expressed as; $\sigma_x = \left\{ \varepsilon_x\beta_x + \eta^2 (\varepsilon/E)^2 \right\}^{1/2}$, where β_x is the betatron function, η the dispersion function, ε/E the beam energy deviation.

Figure 3 shows an enlarged horizontal beam profile observed at the beamline 21 (BL21). This beam profile pulsated at an interval of 1 to 10 msec. Such beam oscillations looked quite complicated, and hence it is very difficult to find the sources of the instabilities. Typical spectrum of the longitudinally oscillating beam is shown in Fig. 4. Some of the spectral lines in the figure are directly related to the chamber structure of the straight section between the bending magnets B4 and B5.

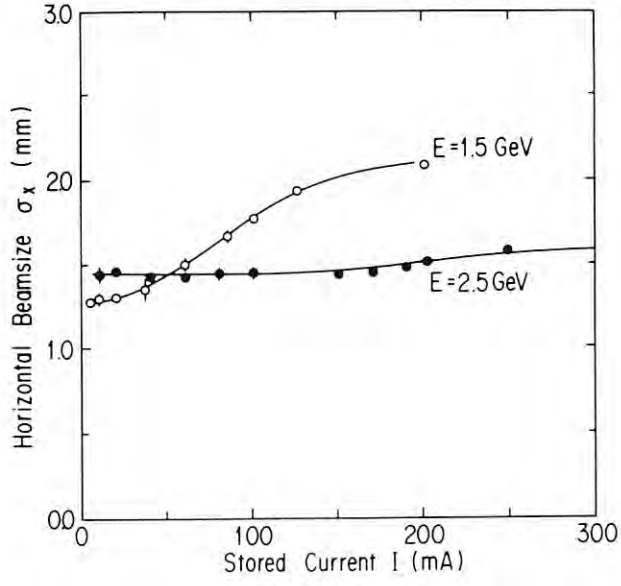

Fig. 2 Horizontal beam sizes (rms) σ_x measured at BL21 with the beam-profile monitor. Beam size at a beam energy of 1.5 GeV (open circles) increased with stored beam current and became larger than that of 2.5 GeV (closed circles) beyond 50 mA.

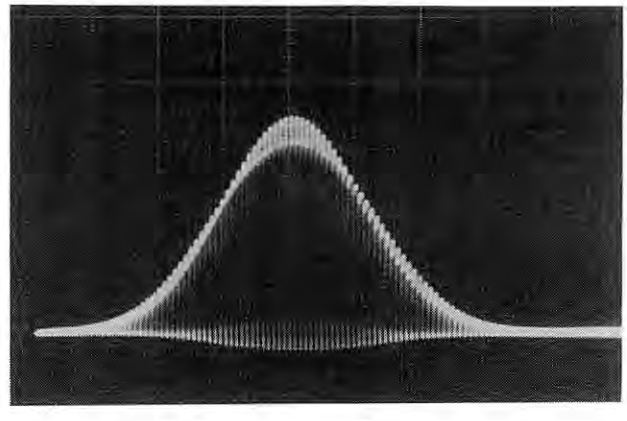

Fig. 3 Horizontal beam profile observed at BL21. The spreading of the trace shows the widening of beam size caused by the longitudinal instabilities. This picture was taken at an energy of 2.5 GeV and a current of 250 mA in the uniform filling of RF buckets.

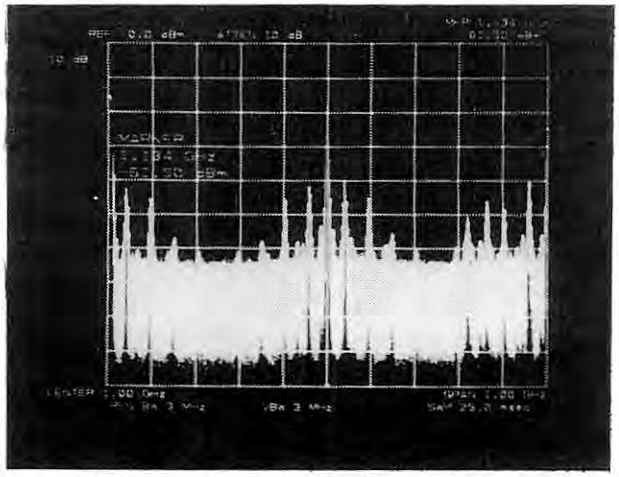

Fig. 4 Typical frequency spectrum of longitudinally oscillating beam with coupled-bunch modes. This picture was taken at 2.5 GeV. The center frequency is 1.0 GHz and the span is 1.0 GHz. Beam current was 94 mA in the uniform filling of RF buckets.

H. Kobayakawa

2. POSITRON STORAGE

Positron storage in the ring was first tried in December 1986. Since then, many preparations for positron storage had been made. The Linac group had tried to get much amount of positron charge in one linac pulse, mainly by changing the pulse length. The Linac and Light Source groups had cooperated to obtain a good matching of optics between the linac and the beam transport line. The Light Source group had paid much effort to get a high injection efficiency by adjusting the position and angle of injected beam at two septum magnets. Details will be described in Section C-1.

On July 11 1988, the polarities of all magnets except insertion devices were reversed, and positrons of 250 mA were successfully stored. The injection rate was about 3 mA per minute with the injection repetition rate of 25 Hz. From just noon of the next day, user time started with positron storage and was continued till July 30. The operational statistics from May 11 to July 30 is described in Table 1 for comparison between electron and positron storage.

In the operation of electron storage, the time for injection is only less than 5 min in average. In addition, it takes 45 min to complete the following procedures: (1) to close beam channels by inserting light absorbers, (2) to sweep out electron beam by the RF knock-out method, (3) to demagnetize the superconducting vertical wiggler and to move it to the injection position with a wide horizontal aperture, (4) to widen the magnetic gap of the multipole wiggler, (5) to store electrons up to a current of 250 mA, (6) to set the multipole wiggler and the vertical wiggler to the working position, (7) to turn on the feedback system to stabilize the beam closed orbit, and (8) to permit users to open the beam channels.

In the operation of positron storage, the injection time for positron is much longer than for electron. Preserving the remaining stored current of about 120 mA, it still took 45 min to store up to 250 mA. This means that the time for injection and completion of the procedures listed above became about 90 min, i.e., just twice as long as that in electron storage.

With positron storage of only 300 hours of user time, we observed many interesting phenomena; (1) two-stream instability due to ion trapping disappeared completely. (2) although abrupt deterioration of beam lifetime occurred three times, it ended shorter than 100 msec, i.e., the time resolution of the measuring system. This implies that a dust or micro-particles may have crossed the beam without being trapped.

The instantaneous beam lifetime of positron storage is just the same as that of electron storage, if the beam was free of abrupt deterioration of beam lifetime. In the case of

Fig. 5 $I_0\tau_p$ normalized by the averaged $I\tau$ compared for electron and positron storage.

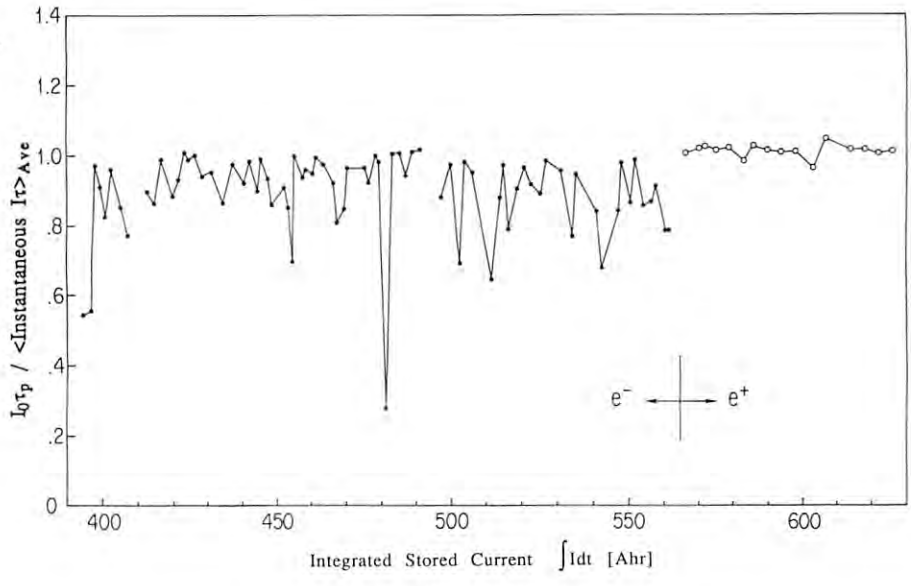

positron storage, a product of current and lifetime $I\tau$ was found to be approximately constant in every run. Thus the following relation holds well between the stored current I and the elapsed time t from the injection, especially when stored current is larger than 100 mA:

$$I = \frac{I_0\tau_0}{t+\tau_0} , \qquad (1)$$

where I_0 is the initial stored current and τ_0 the instantaneous beam lifetime at t=0. With the superconducting vertical wiggler in operation, $I_0\tau_0$ was 6.5 ampere-hours (A·hrs) when multipole wiggler (MPW) was set at its wide gap position, and 5.2 A·hrs when at narrow gap (18 mm) position, respectively. In electron storage, there were abrupt deteriorations of the beam lifetime. So the decay curve of stored current was not smooth but had many downfalls. Nevertheless, the overall decay curve can be expressed with an equation similar to Eq.(1). We can then calculate the stored current averaged over the time T used in one user run,

$$I_{ave} = \frac{I_0\tau_p}{T} \log\left(1+\frac{T}{\tau_p}\right) , \qquad (2)$$

where τ_0 in Eq.(1) was replaced by τ_p. With I_{ave}, T and I_0 recorded for every run, τ_p can be calculated from Eq.(2). $I_0\tau_p$ is more useful than τ_p to evaluate the quality of ring performance. To compare the values of $I_0\tau_p$ between electron and positron storages, the following correction is necessary, because the vacuum pressure had decreased gradually from the middle of May to the end of July. At first, instantaneous $I\tau$ was calculated every hour when there was no abrupt deterioration of the beam lifetime, and averaged over each run. Then, $I_0\tau_p$ was normalized by the averaged $I\tau$. Figure 5 shows the normalized $I_0\tau_p$ versus integrated stored current. In the positron storage, normalized $I_0\tau_p$ is 1.015 in average and the curve is very smooth with the maximum deviation within 0.012. While, in the electron storage, the average is 0.910 and the minimum value is 0.275. This means that, in the electron storage, electron beam traps dust or micro-particles frequently. The inverse of the normalized $I_0\tau_p$ may indicate a degree of dust trapping. We call τ_p as "practical beam lifetime".

K. Huke

C. IMPROVENENTS AND DEVELOPMENTS

1. INJECTION

The injection system was reconstructed for the positron accumulation and it was commissioned at the end of March 1988. The new system has two passive type septum magnets with eddy current screening, and four kicker magnets with ferrite core. These septum and kicker magnets were excited by new power supplies at a repetition rate of 25 Hz. The linac can provide different pulse lengths i.e., a short pulse of 4 nsec and a semi-long pulse of 40 nsec.

Operation with the positron beam for the user's experiments started on July 20 1988.

1a. New Equipment for the Positron Injection

(1) Septum Magnets.

Two septum magnets were constructed for the positron injection. They were passive type magnets made of laminated silicon steel cores with eddy current screening shields. Dimensions of the cores and the coils were decided on the basis of a calculation using the computer code TRIM. The eddy current screens were designed using a test model and a computer simulation. Specifications of the magnets are listed in Table 2. These septum magnets were set in their vacuum chambers. The coils and the eddy current screens were cooled by water.

Table 2 Specifications of septum magnets

Type	Septum 1	Septum 2
Core length	1500 mm	1000 mm
Deflection angle	7.0 degrees	5.0 degrees
Number of turns of coil	1	1
Dimension of window	25 mm x 10 mm	25 mm x 10 mm
Maximum current	6000 A	6000A
Self inductance	6.8 μH	4.8 μH

(2) Power Supplies for the Pulse Magnet.

The power supplies for the septum and kicker magnets consisted of pulsers and charging power supplies. A pulse forming network (PFN) was used in the pulser of each new power supply. The capacitors of PFN were discharged with SCR switches for the septum power supplies and thyratrons for the kicker power supplies. A regeneration circuit was applied to each pulser to save the charging power. With this regeneration circuit, 70 % of the power was saved.

(3) Wall Current Monitors.

Three wall current monitors designed and fabricated in the Linac Department were assembled for the positron injection. Their cutoff frequencies were higher than 500 MHz. Two of them were installed in the beam transport (BT) line. The first one (WCM2) was set near the entrance of the BT line and the second one (WCM3) in the middle. These two monitors observe wave forms and currents of the positron beam passing through the BT line. The third one (RWCM) was installed in the short straight section between B22 and B23 of the storage ring to observe a current decay of the injected beam at every turn around the ring.

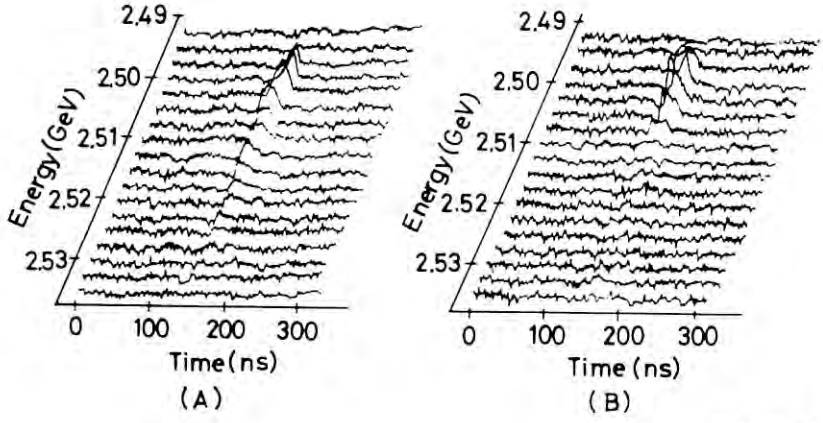

Fig. 6. Energy spectra of the positron beams. RF phases of the positron linac were (A) 0 deg and (B) 6 deg.

1b. The Energy Spectra and the Transportation of the Positron Beam

(1) Energy Spectra of the Positron beams

Energy spectra of the positron beams with the pulse length of 40 nsec were measured by the same method as previously used in the measurement for the electron beams[1]. The energy resolution of 0.1 % was set by a beam slit situated in the BT line. The spectra were then taken by varying the RF phases of the positron linac. Figure 6 shows the beam intensities as functions of time and beam energy. The spectra (A) and (B) correspond to 0 and 6 degrees of the RF phases of the positron linac, respectively. The energy spread obtained in the best condition was 0.5 %.

(2) Transportation of the Positron Beams

Twiss parameters of the optics at the end of the linac strongly depended on the condition of the positron linac. Transportation efficiency of the BT line was only 10 % without adjustment. Therefore, we had to adjust the optics in the matching section[2], which is between the end of the linac and the entrance of the BT line. The steps for the adjustment were; (1) to measure the Twiss parameters, (2) to calculate the optics in the matching section by the computer code MAGIC, and (3) to set the calculated optics on the matching section. After this adjustment, the transportation efficiency became 60%.

1c. Injection of Positron Beam

Figure 7 shows the phase space of the injection beam. The injection bump was set to 20 mm and -1 mrad at the injection point, while positron beam was injected at 34 mm and -2 mrad.

An accumulation rate was about 0.08 mA/sec for the 4 nsec pulse with a peak current of 12 mA at the end of the linac, while it was 0.24 mA/sec for the 40 nsec pulse with a peak current of 1.5 mA. In the latter case, the accumulation time for 300 mA was about 30 min. As a result, about 23% of the linac positrons were accumulated in the ring.

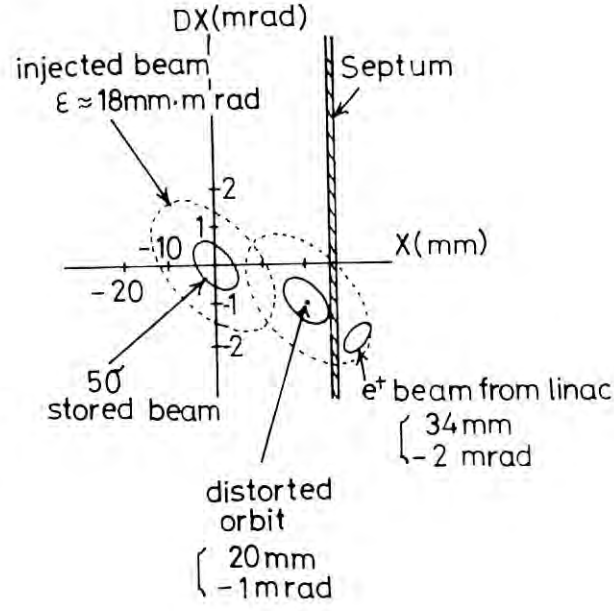

Fig. 7 The phase space of the injection beam.

References

1) T. Mitsuhashi, T. Urano, T. Katsura, K.Haga, A. Enomoto, H. Hanaki and S. Ohsawa: Proceedings of the 12th Linear Accelerator Meeting in Japan, p.129,1987.
2) T. Mitsuhashi, M. Katoh and S. Ohsawa: Proceedings of the 13th Linear Accelerator Meeting in Japan, p.31,1988.

T. Mitsuhashi

2. RF

2a. Elimination of Cavity-Induced Coupled-bunch Instability

Since the horizontal emittance was reduced from 400 to 126 nm·rad to increase the beam brightness, it have inevitably altered the characteristics of the instabilities; the threshold currents were lowered. In the low-emittance optics, a natural bunch length is 1.5 cm (2/3 in the higher emittance optics), leading to an increase of the longitudinal instabilities, because of the reduction of the Landau damping. In fact, the threshold current of TM011-instability (referred to as "758" in

the previous Activity Reports) became smaller from above 300 mA to below 100 mA, as shown in Fig. 8. At the time of this measurement, the cavity#1,#2 and #4 had the higher-order-mode (HOM) couplers to reduce the resonance impedances. However, the spreading of the resonance widths by lowering Q-values caused an overlapping to other resonances, which resulted in a difficulty of avoiding the instabilities.

Then we tried a new method to avoid the instabilities without lowering Q-values. Each HOM coupler was replaced by the blank-cap which was a stainless-steel vacuum flange with a cylindrical copper block (Fig. 9). The resonance frequencies of six dangerous modes were carefully shifted by properly choosing the the lengths of the blank-caps. Table 3 shows the amounts of frequency shifts for the lengths of the blank-caps.

Table 3 Amounts of frequency shifts for the lengths of the blank-caps. The cavity has two openings at upper and side walls. These data were taken by altering the lengths of one blank-cap with the other one and the tuning plunger fixed.

Mode	upper blank-cap (kHz/mm)	side blank-cap (kHz/mm)
TM010	50	50
TM011	-45	-45
TM110H	---	200
TM110V	180	---
TM111H	---	10
TM111V	-170	---
TM013	40	40

In high rf-power operation, the HOM-frequencies are shifted due to the following mechanism. (1) The HOM-frequencies are shifted by the temperature rise of the cavity, and (2) at the same time, they are also shifted due to the tuning mechanism (a tuning planger and a feedback loop circuit) for the accelerating frequency of 500 MHz.

Although it is difficult to directly measure the HOM frequencies under the high power operation, the amount of shifts of these frequencies can be estimated from data obtained with low power measurement as follows. Assuming that the cavity expansion due to the temperature rise is homogeneous, the frequency shift δf of a HOM is expressed as $\delta f/f=\delta f_0/f_0$,where f is the resonance frequency of the HOM, f_0 the frequency of the accelerating mode, and δf_0 its frequency shift. Supposing that Δl_e is the amount of the movement of the plunger when the rf-power is put into a cavity up to the standard operating value(22.5 kW/cavity), δf_0 is expressed as $\delta f_0=-(df_0/dl)\cdot\Delta l_e$, where (df_0/dl) is the frequency dependence on the position of the tuning planger.

On the other hand, the frequency shift due to the tuning mechanism is given by $(df/dl)\cdot\Delta l_e$. Therefore, the total frequency shift Δf of HOM in the cavity operating in high rf-power is approximately expressed as;

$$\Delta f = -\left(\frac{f}{f_0}\right)\left(\frac{df_0}{dl}\right)\Delta l_e + \left(\frac{df}{dl}\right)\Delta l_e \quad , \qquad (3)$$

where (df/dl) is frequency dependance of the HOM on the tuner position. The first term in the right-hand side is the shift due to the expansion of the cavity and the second term is that from the tuning mechanism. Since all these quantities in the right hand side of Eq. (3) are measurable, we can estimate the total frequency shift Δf.

During summer shutdown in 1987, the HOM frequencies of all rf-cavities were trimmed by adjusting the length of blank-caps. Cavity-induced instabilities were then largely suppressed. TM011-instability was completely cured within the operating frequency region as shown in Fig. 10. As for the transverse instabilities, we have never encountered serious problems around the operating betatron tunes, with the help of the octupole magnets.

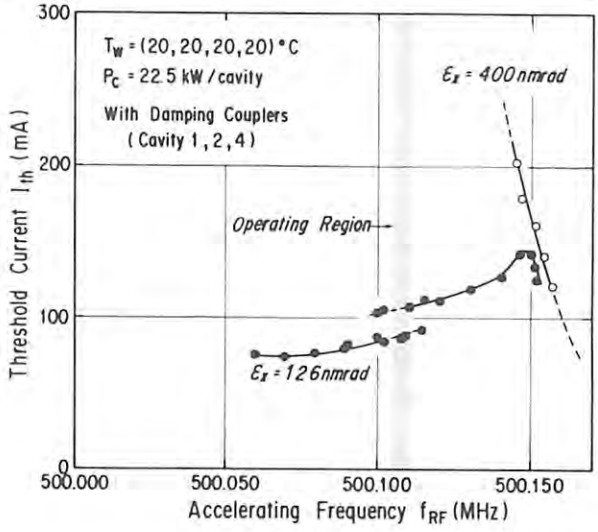

Fig. 8 Two threshold curves of the longitudinal instability due to the TM011-like mode for (a) ε_x=400 nm·rad, and for (b) ε_x=126 nm·rad. The HOM-damping couplers were used in the cavities #1,#2 and #4. Temperature settings of cavity cooling water were all 20 °C. Dissipation power was 22.5 kW for each cavity.

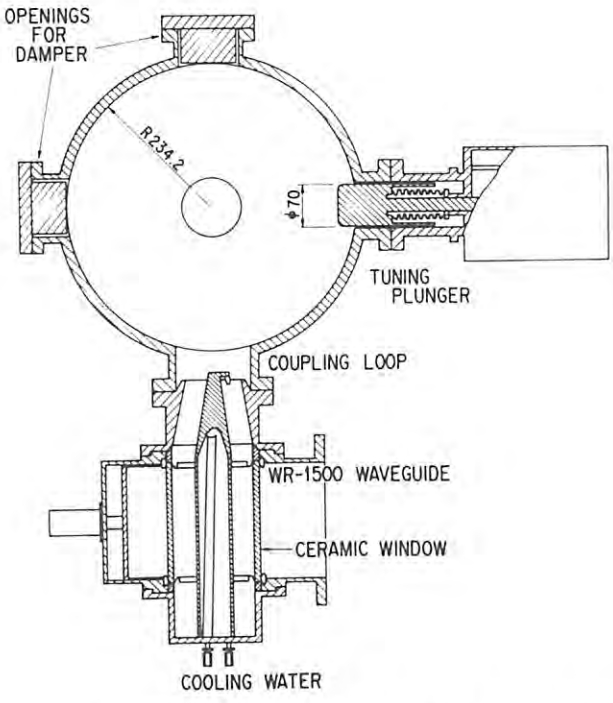

Fig. 9 Schematic view of a cavity with blank-caps in upper and side openings. The circular hole at the center of the cavity shows the beam duct.

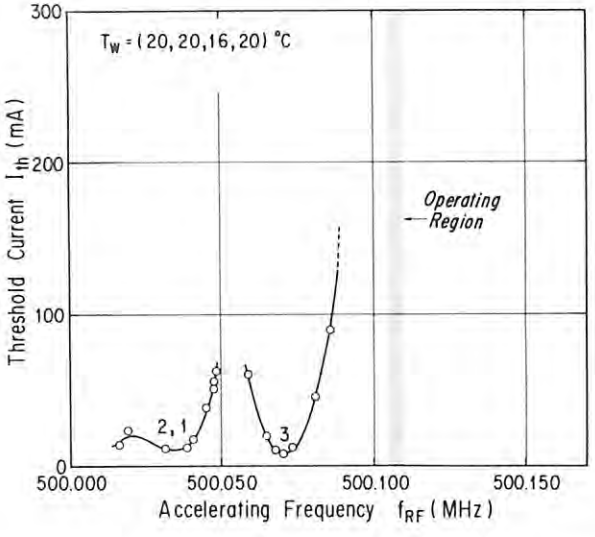

Fig. 10 The threshold currents of the TM011-instability after the improvement by properly choosing the blank-cap length to trim the HOM frequencies. Cavity temperature settings were 20,20,16 and 20 °C. Numbers 1 to 3 in the figure indicates cavity number. The cooling water temperature of the cavity#3 was lowered from the normal value(20 °C) in order to separate the instability due to individual cavity.

M. Isawa

3. VACUUM

3a. Improvements

The following improvements of vacuum system were carried out during 12-week shutdown in summer 1987.

Two vacuum ducts called B-duct at bending magnets B19 and B28 were replaced by new ones. The new B-duct has a port to extract a synchrotron radiation(SR) from an insertion device at the upstream of the bending magnet.

The vacuum chambers at the kicker magnets were modified as the kicker system was improved for positron injection. As reported in the previous Activity Report, one of four kicker chambers at the kicker magnet K3 had been replaced with a ceramic duct in 1986. Since it had been working well in one year operation, the other kicker chambers were replaced with new ceramic ducts as K3 duct.

Three gate valves were newly installed. One of them was located between K2 and K3 in order to bake out their vacuum ducts separately. Other two valves were set at the upstreams of B05 and B19 in order to make easy the maintenance of the insertion devices. Each valve has a shutter plate preventing the Viton seal from being heated by wake fields.

3b. Pressure Change in the Ring

About two thirds of the whole vacuum ducts except B09 to B17 were filled with dry nitrogen on July 20 to keep them from being polluted. These ducts were exposed to the air for 36 days during the improvements. The evacuation started on August 25 and the whole ducts were baked for 2 days. The first beam was injected into the ring on October 7 for degassing vacuum ducts. After the time integration of stored beam current (integrated current) reached 18 A·hr, user run started on October 16. The pressures in vacuum ducts were always monitored by 48 B-A gauges around the ring. Figure 11 shows pressure changes as a function of integrated current until the end of July 1988. Pressures in the figure are normalized by stored beam current. The normalized pressure denoted as P_{av} is the average value over all the gauges. The G#35 and G#47 in the figure are the normalized pressures measured at the downstreams of the new B-ducts B19 and B28, and the G#10 and G#23 at the downstream of the B-ducts B05 and B14. Both B05- and B14-ducts had been irradiated with the SR in the previous ring operations. In this summer shutdown, the B05-duct was exposed to the air for 36 days, while the B14-duct was kept in an ultrahigh vacuum. It can be seen in Fig. 11 that at the beginning of the operation the pressures in the new ducts at B19 and B28 were three orders of magnitude higher than that in the unexposed old duct at B14, and one order of magnitude higher than that in the exposed old duct at B05. However the normalized pressures decreased linearly on log-log plotting, while the value of G#23 at B14 stayed low all the

time. The small fluctuation of data points in Fig. 11 are due to intermittent flashings of Ti sublimation pumps. For the new ducts the following relation holds approximately;

$$\ln(P/I) \;/\; \ln(\int I\,dt) = -1/2. \qquad (4)$$

When the integrated current reached 300 A·hr, almost all the pressures in the ring came close to the pressure in the unexposed section(i.e., B14) and the averaged normalized pressure P_{av} became 1×10^{-12} Torr/mA.

3c. Beam Lifetime

The beam lifetime τ is inversely proportional to the pressure P, and the outgassing in the ring is proportional to the stored beam current I. Since the pressure in the normal operation of the ring is more than one order of magnitude as high as the background pressure, it can be considered to be proportional to the stored current. The vacuum performance of the ring is well evaluated by the product of the lifetime and the stored current(Section B-2). Figure 12 shows the instantaneous value of $I\tau$ as a function of integrated current. Open circles in the figure represent the values for the positron storage. It can be seen from Figs. 11 and 12 that the $I\tau$ increased inversely proportional to the normalized pressure P_{av}, and it became 5 A·hr when P_{av} reached 1×10^{-12} Torr/mA.

The collision cross section can be empirically evaluated using $1/(P\tau)$. Typical value of $1/(P\tau)$ of the ring was 5.5×10^{4} $(\text{Torr}\cdot\text{sec})^{-1}$, and well agreed with the calculated cross section, where we assumed that the main residual gas component is CO and took into account the minimum aperture of the vacuum chamber .

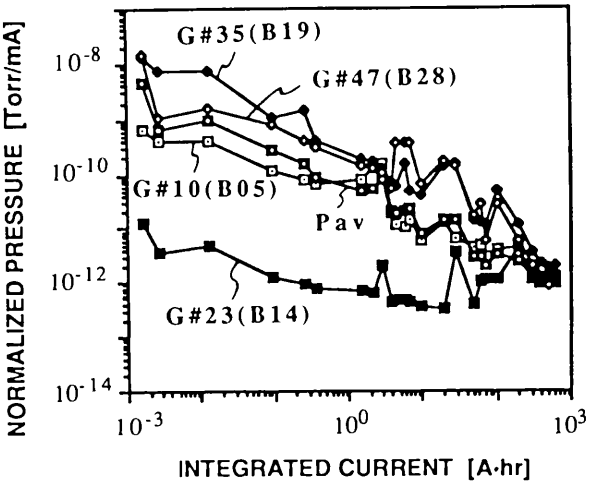

Fig. 11 Pressure changes in PF ring from October 1987 to July 1988.

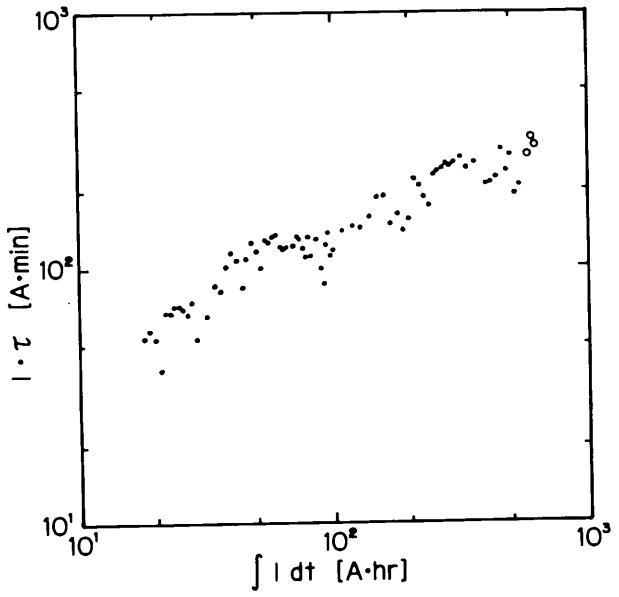

Fig. 12 Change of the product $I\tau$ of PF ring. Solid circles indicate the values in the electron storage and open circles the values in the positron storage.

Y. Hori

4. INSERTION DEVICES

4a. General

At the Photon Factory, seven insertion devices are in operation and under construction. The specifications of each insertion device are described briefly.

(1) *A superconducting wiggler, VW#14*

The 3-pole wiggler which has been operating since 1983 is to produce vertically polarized radiation in the range of photon energy up to 100 keV with a magnetic field up to 6 T in the horizontal direction. However, the present device will be replaced by a new 5-pole wiggler to save consumption of liquid helium and to avoid moving the device. More details are described in the following section.

(2) A 60-period undulator, U#02.

The undulator, which is made of permanent magnets with a period length of 6 cm and is in operation since 1983, is a highly brilliant source in the soft X-ray region with spectral brilliance 100 to 1000 times higher than that of the bend source of the PF ring. The magnets of U#02, which is only one device made of $SmCo_5$ with a pure type structure in the Photon Factory, will be replaced with NdFeB permanent magnets, NEOMAX35H, during the next summer shutdown. The maximum magnetic field will increase from 0.3 T to 0.4 T, so that the limit of the photon energy of the first harmonic will be lowered from 400 to 250 eV.

(3) A 26-period multipole wiggler, MPW#16.

This wiggler with a period length of 12 cm (in operation since 1987) is composed of hybrid-type permanent magnets made of NdFeB and permendur. The wiggler has both undulator and wiggler modes of operation. The maximum magnetic field of 1.47 T is obtained at the gap height of 19 mm. The vacuum chamber of the wiggler has two different apertures for injection and operation mode. In order to select the aperture, only the chamber is moved in the horizontal direction.

(4) A multi-undulator, Revolver#19 (ISSP-KEK)

A multi-undulator (ISSP-KEK) with four different lengths of period (5, 7.2, 10, 16.4 cm) has been constructed and installed in the B18-B19 straight section in April 1988. The details are described in the following section.

(5) A 13-period multipole wiggler, MPW#13 (RIKEN-KEK).

The wiggler with a period length of 18 cm (in operation since Dec. 1988) has a structure similar to that of the MPW#16. The maximum magnetic field of 1.5 T is obtained at the gap height of 27 mm.

(6) Two elliptically polarized multipole wigglers, EMPW#NE1 (21 periods) and EMPW#28 (12 periods).

EMPW#NE1 installed in the Accumulation Ring of TRISTAN is in operation from October 1988, while EMPW#28 will be installed in the PF ring in March 1989. These wigglers have a period length of 16 cm and generate elliptic polarization with higher harmonics. The maximum magnetic fields in the horizontal and vertical directions are 0.2 T and 1.0 T, respectively. With lower field, they can be used as undulators. The details on the performances of EMPW#NE1 are described later.

The calculated spectra of the devices and the bend source are listed in Table E-4 and shown in Fig. E-3 of Section E. The locations of the insertion devices in the PF ring are shown in Fig. E-2 of Section E.

H. Kitamura

4b. Design and Specifications of 5-pole Superconducting Vertical Wiggler

A superconducting vertical wiggler with 3 pairs of magnets has been operated at PF since 1983. This wiggler has to be demagnetized and lifted up at every injection to provide a wide aperture for injection. It takes about 40 minutes for the wiggler to be ready for the experiment and this time loss is not negligible in the operation of PF ring. The new wiggler will be operated more easily without the time loss. The new wiggler consists of 5 pairs of superconducting magnets with iron poles as shown in Fig. 13. The three inner pairs can produce the maximum field of 5 T on the beam orbit and the two outer pairs are used to correct the beam orbit. The gap of a magnet was chosen to be 66 mm in order to get an aperture wide enough for injection. In the low emittance mode, a ratio of the betatron function β_x at the wiggler to β_x at the injection point is about a half of that in normal emittance mode. Then it became possible to have a gap width narrower than the old one.

The magnetic field was calculated by using the 3-dimensional computer codes BOBPOL and JMAG. The field strength of 5 T can be realized with the current density of 123 A/mm^2 in the coil. Then the maximum field in the coil becomes 7.2 T. The superconducting material NbTi is well suited for obtaining such a high field. The coil has 2520 turns of NbTi wire.

Since the beam is wiggled on the vertical y-plane, the effect of edge focusing gives a finite horizontal tune shift $\Delta\nu_x$, but it cancels out for vertical tune shift $\Delta\nu_y$. However, the $\Delta\nu_y$ is produced by the gradient of the nonlinear field on the vertically wiggled orbit. The strength of horizontal magnetic field $B_x(T)$ as a function of y(m) is described as the following equation,

$$B_x = B_0 - 0.113 B_0 y^2 - 263 B_0 y^4. \qquad (5)$$

For the wiggled orbit of 5 mm, $\Delta\nu_x$ and $\Delta\nu_y$ are estimated to be 0.087 and -1.8×10^{-4}, respectively. These tune shifts will be corrected by changing the currents of nearby quadrupole magnets in the same manner as done for the present wiggler.

The wiggler cryostat is shown in Fig. 14. Two layers of thermal shield are put between the wiggler wall and the helium vessel. The thermal shields are cooled by two refrigerators. The outer and inner shields are connected to the first stage (60W at 80K) and the second stage (6W at 20K) of each refrigerator. The helium vessel is connected to a third refrigerator (2.5W at 4.2K) which re-liquefies the evaporated helium.

To avoid a heat inflow from the current lead, the wiggler is operated in a permanent current mode by using superconducting switches. The current gradually decreases with the life time of about 25,000 hours due to the resistance

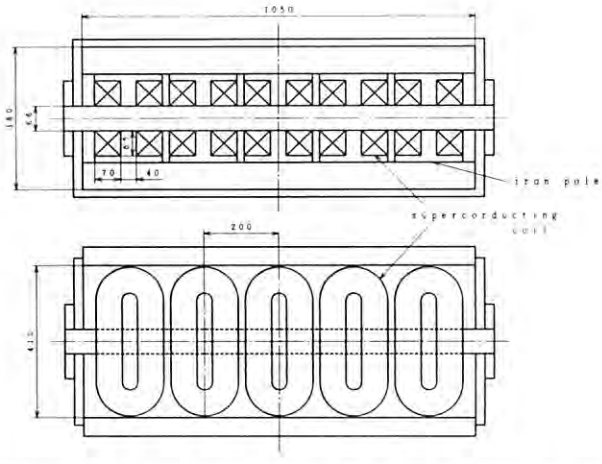

Fig. 13 Schematic view of the superconducting wiggler magnet.

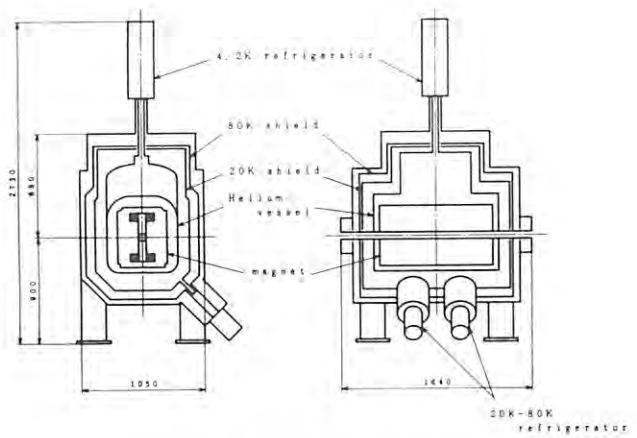

Fig. 14 Schematic view of the wiggler cryostat.

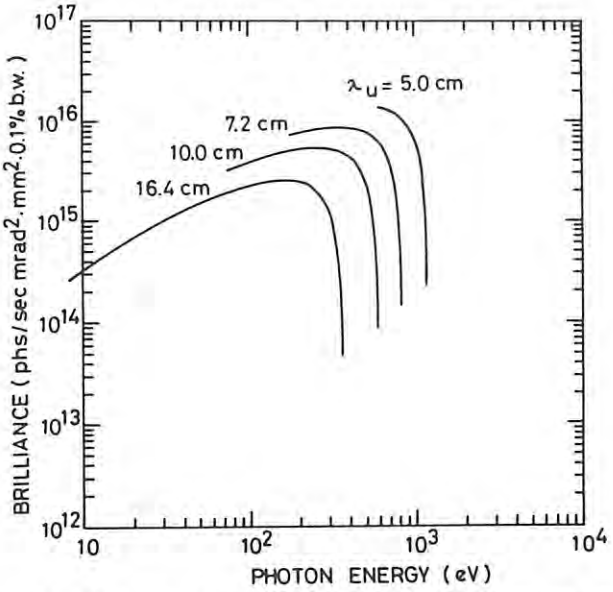

Fig. 15 Energy range and the brilliance at a beam current of 250 mA for the fundamental peaks covered with four undulator magnets.

of the junctions between the coils. The current will be restored every 250 hours, during which the decrease of the current is 1%. The effect of the current decrease on the vertical beam orbit will be corrected by steering magnets.

K. Ohmi

4c. Construction and Commissioning of Revolver #19

The Revolver (multi-undulator) provides high brilliant radiation with a relatively low power in the energy range from 7.8 to 1150 eV for the beamline BL-19 with two experimental stations.

The design is based on the following criteria:

(1) The high brilliant radiation from the insertion device is available in a wide energy range from 10 to 1100 eV.
(2) The radiation power should be as low as possible in order to avoid the heat damage to the pre-mirror and optical elements in a monochromator.
(3) The operation of the insertion device should not affect the stored beam.

In order to cover all the required energy range, we made use of a multi-undulator design with four undulator magnets(A,B,C,D) made of permanent magnet blocks. The maximum magnetic field is 0.62 T at the minimum gap of 30 mm. The energy range and brilliance for the fundamental peak covered by four undulator magnets are shown in Fig. 15. The maximum radiated power from the insertion device was estimated to be 0.88 kW at a beam current of 250 mA.

Figure 16 shows the mechanical design of the revolver. The revolver consists of two rotatable shafts with four base plates, on which the undulator magnets are mounted. A pair of undulator magnets with a desired period length can be selected by revolving the rotatable shafts, and the magnet gap is adjusted by an up- and down-motion of the two shafts. Horizontal steering magnets of an air core type are installed at both ends of the revolver. The vacuum chamber of the device has two different apertures, the narrow one for the circulating beam and the wide one for the pumping system with two sputter-ion pumps of 60 l/s and seven titanium sublimation pumps. The vertical size of the aperture for the beam is 24 mm and the chamber wall is 2 mm thick, so the minimum magnetic gap of 30 mm was achieved with a margin of 2 mm. The undulator chamber is smoothly connected to the ring vacuum chamber at both ends with 4.5 cm transition parts in order to avoid the parasitic mode loss of the beam. The pressure achieved is about 5×10^{-11} Torr without the beam. The undulator parameters are listed in Table E-4 of Section E. The permanent magnet material is NdFeB (NEOMAX35, Sumitomo Special Metals Co.) with B_r = 12.1 kG and iH_c = 12 kOe. The undulator magnet D is of a pure type structure and the other magnets are of a hybrid type with the pole pieces of vanadium permendur.

The longitudinal and transverse distributions of the magnetic field were measured with a Hall probe. Using the measured data, we adjusted the magnetic field in the undulators as follows. First, several magnet blocks were interchanged. Then, for the hybrid type magnets A, B, and C, the magnetic field was corrected by using iron tuning studs so that the electron beam can move on an ideal trajectory. The horizontal steering magnets at its both ends were prepared to eliminate the residual deflection and displacement of the beam going through the whole undulator. At the beginning of its operation, we observed the deterioration of the beam lifetime. This happened only when the magnet gap was being made narrower.

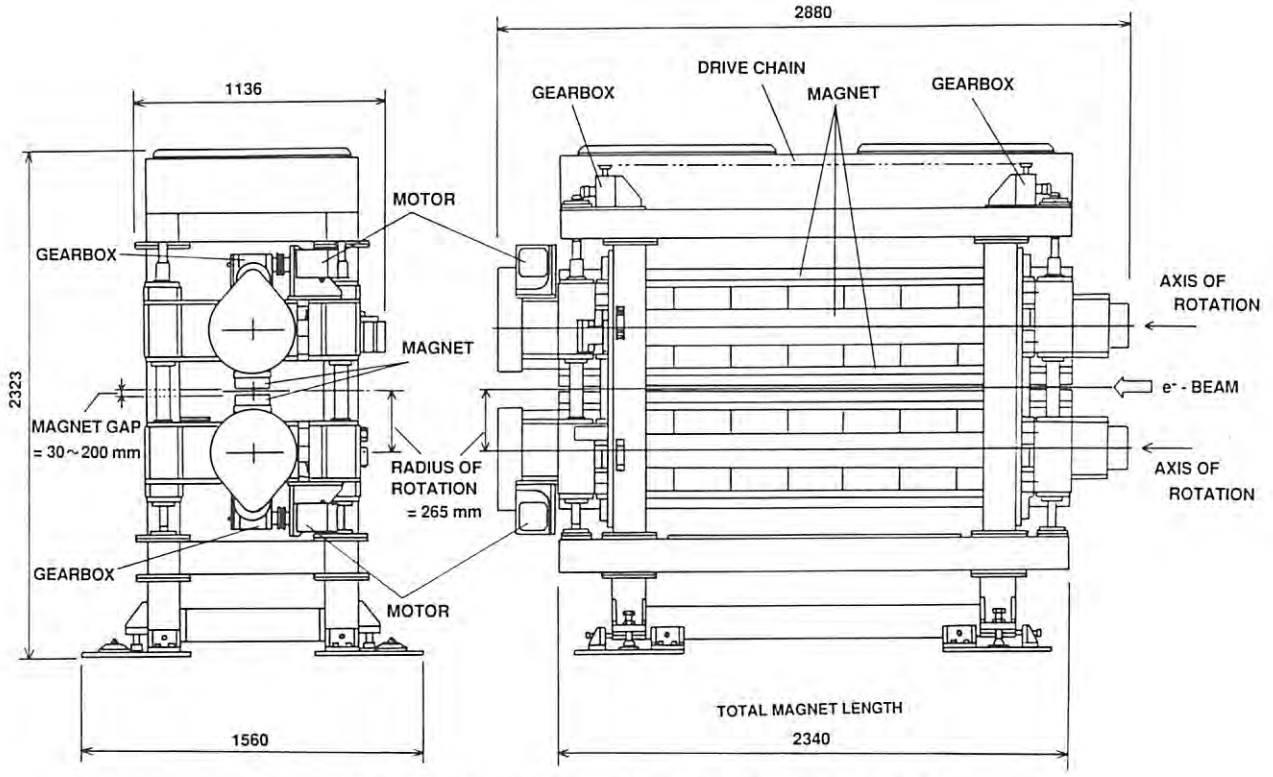

Fig. 16 Mechanical structure of Revolver #19.

The loss rate of the stored beam became smaller and smaller as we continued to operate it. We suspect that the origin of this is dusts falling off from the chamber wall due to vibration of the Revolver.

We measured the closed orbit distortion induced by the Revolver. Although correction currents of the horizontal steering magnets were determined by the magnetic field measurement prior to installation, a small modification in correction currents was required.

H. Ohkuma

5. MONITOR

5a. New Digital Feedback System

A digital feedback system has been used to suppress the diurnal drifting motion of the closed orbit since March 1987. However, performance of this system was limited in resolution with its 12-bit DAC's and in setting speed of about 40 sec for the whole steering magnets (vertical dipoles). In order to achieve a finer resolution in current setting and a faster setting time, we have constructed a new digital feedback system.

The new system is shown in Fig. 17, including the beam orbit measurement system. An HP310 computer is used to control the steering system, while the other HP 310 computer is dedicated to the orbit measurement system. The four HP computers are connected to the server through an SRM (Shared Resource Management) interface to share data on its common 81-Mbyte hard disk. The HP330 and HP350 computers can easily

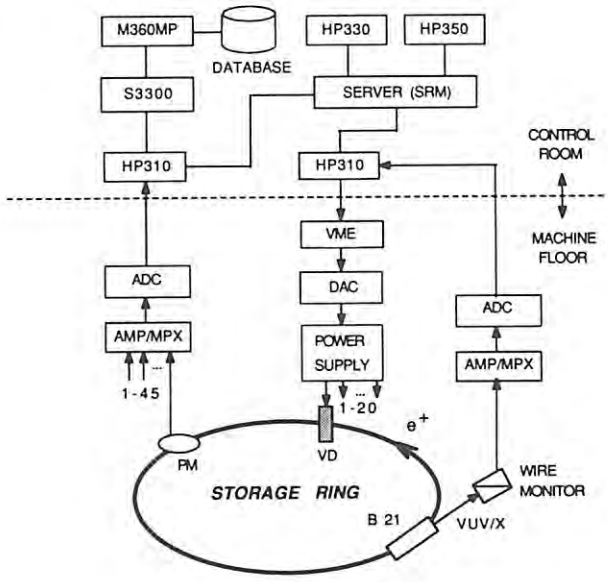

Fig. 17 Block diagram of the new digital feedback system and the orbit measurement system.

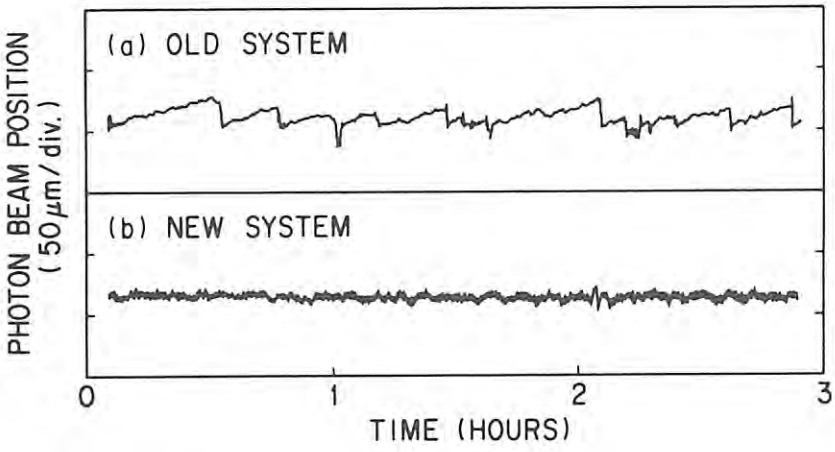

Fig. 18 Photon beam motion at beamline 21 with (a) the old and (b) the new feedback systems.

display and plot the data. Twenty steering magnets with their power supplies were newly installed for the new system. Their deflection angle per current 0.028 mrad/A is eight times as small as that of the steering magnets used in the previous system. The VME computer is connected to the HP310 control computer through an optical RS232C cable. According to a request from the control computer, it quickly sets output data to the 16-bit DAC's through the VME bus. The 16-bit DAC's can perform a finer current setting for the magnet power supplies than the old 12-bit DAC's. The new system completes the feedback process only within 2 sec, including a measurement of the photon beam position at the beamline 21.

Fig. 18 shows the photon beam motion monitored at the beamline 21 with the old and new digital feedback systems. A correction is executed whenever the beam drift from a reference position exceeds 20 and 5 μm for the old and new systems, respectively. The fine correction by the new system is realized due to the fast setting time and the fine resolution of the DAC's.

5b. Renovation of Beam Orbit Measurement System

The beam orbit measurement system consists of 45 position monitors, a signal processing system and a computer control system. Recent modification made it possible to acquire data faster and more accurately and to operate more easily.

The position monitors were previously switched in the order of the position monitor number with the multiplexing time of 120 sec. In the new multiplexing scheme, the position monitors were grouped into 8 stations and switched in parallel. As a result, the multiplexing time reduced to 13 sec.

The position monitor signal is digitized by a digital voltmeter (DVM). The old DVM (HP3487A) was replaced with a faster one (Solartron 7061), which was set to the resolution of 4 digits. The total digitization time became smaller by a factor of two and the digitization accuracy was improved by one order of magnitude.

The new control computer (HP310) is faster in loading and execution time than the old computer (PANAFACOM C-180A), and it has a touch screen with a resolution of 56x43 in order to avoid any keyboard operation. We installed a new plotter and printer with additional 256-kbyte I/O buffers to reduce the transfer time. The beam position data are stored on the common hard disk of the server, and they can also be sent from the control computer to the mini-computer (FACOM S-3300), and finally to a general-purpose computer (FACOM M-360MP).

With these improvements, the total time of a beam orbit measurement was reduced from 120 to 47 sec. Moreover, the position resolutions in the orbit measurement system became as small as 10 μm. The operation of this system has become easier and more flexible due to the touch screen and the SRM network.

N. Nakamura

5c. Distortion of the Light Source Building

Drifting motion of photon beam in the low-emittance operation shows the following characteristics. First, the photon beam moves diurnally with a minimum at 8 o'clock and a maximum at 15 o'clock. Second, the magnitude of the drifting motion is large on a sunny day and small on a cloudy or rainy day. These characteristics suggest a close relation between the drifting motion of the photon beam and the atmospheric environment around the Light Source building.

A computer simulation of the distortion of the Light Source building was made by Shimizu Construction Co. Ltd. The simulation revealed the cause and mechanism of the beam drift to some extent. The building undergoes thermal stress on the roof which expands and contracts as the atmospheric temperature changes.

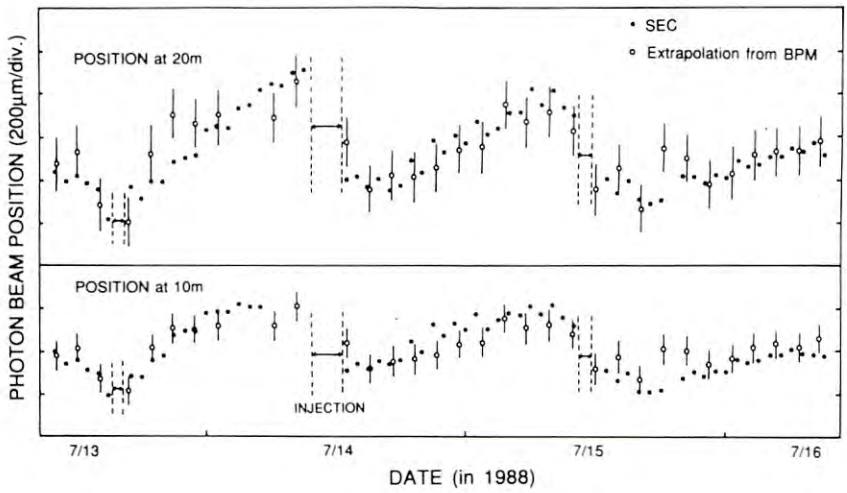

Fig. 19 Comparison of the vertical photon beam positions at BL-4C measured by two independent monitors: two split emission chambers (SEC) and a set of two electron beam position monitors (BPM) in the ring.

The thermal stress propagates from the roof to the ring tunnel floor and causes the closed orbit to be distorted.

In order to examine whether the daily drift of the photon beam came from that of the electron beam, we measured the vertical position of the photon beam by two types of monitors and compared the results (Fig. 19). The first type of monitors was a split emission chamber (SEC). Two SEC's were installed at 10 m and 20 m apart from the source point of the BL-4C to measure the vertical position and angle of the photon beam. The second type was two electron beam position monitors (BPM) mounted in the storage ring. The vertical position of the photon beam was obtained by extrapolating from the positions of the electron beam monitored by the two BPM's. These measurements by SEC's and BPM's gave almost the same results. The results imply that the daily drift of the photon beam may come mainly from that of the electron beam.

In order to get rid of the cause of the beam drift, we made an experiment. The temperature on the roof partly covered with urethane foam was measured for four different thicknesses. The insulator with 50 mm thick was enough to reduce the temperature change of the roof from 15 °C to less than 1 °C.

K. Haga

6. CONTROL

The entire control computers of PF storage ring were replaced by new ones in April 1985. Programs for each control section such as RF system, beam monitoring devices and magnet power supplies have been gradually converted to new control computers (FACOM S-3000 series). By the summer of 1987, we completed the whole conversion work.

Main differences between old and new programs for the magnet control are as follows. The programming language was changed from the BASIC to the FORTRAN77. The old program was a single task of about 3000 steps, and it was difficult to revise or maintain the program. We divided them into 10 independent programs which can run as concurrent tasks. For example, each task changes magnet currents, initializes the magnets, sets up beam transport magnets for injection, adjusts quadrupole currents during exciting the wiggler magnet and so on. The number of subroutines is 168 and the total number of program steps is about 6700.

The hardware and interfaces of the magnet control remained mostly unchanged as before, except a change of CAMAC data link from parallel to byte-serial, because the new control computer was placed about 200 meters away from the CAMAC crate. The computer and the serial crate controller were linked by an optical fiber cable.

In the new system, beam position data of 45 monitors gathered by the local computer HP-310 (Hewlett-Packard) were transferred to the S-3300 through RS-232C. The S-3300 then sends them to the general-purpose large computer (FACOM M-360MP), which stores them into a database and a temporary file. On an interactive terminal of M-360, COD corrections are made and then the result is sent back to the magnet control computer. Finally the magnet system receives the correction data. It takes about 10 sec to transfer a file of the correction data from M-360 to S-3300.

The operator console of the magnet control was also changed. The old one consisted of a board of 70 push buttons and an ASCII terminal. The status of push buttons were read by CAMAC input registers. The new console is a touch screen with 14" color monitor. The touch screen system is locally controlled by a microcomputer which communicates with the control computer through RS-232C. The magnet control program uses about 40 pages of menu which has a tree-like structure. It is easy to add new entries of menu only by changing the data on a configuration and attributes of touch buttons.

C.O. Pak

7. BEAM CHANNEL

7a. General

User's experiments started with 8 beamlines (25 experimental stations) in FY 1983. Up until

the end of FY 1988, sixteen beamlines were in operation and four beamlines (BL-3,5,13,18) were installed for commissioning. In addition to those beamlines, a new beamline AR-BL-NE1 has been commissioned at the TRISTAN Accumulator Ring. Table E-12 of Section E summarizes the beamline status in FY 1988.

A distributed control system with a microcomputer LSI-11/23 has been controlling all the beamlines. Each beamline has the following components: two vacuum valves, beam shutter, water-cooled SR absorber, fast closing valve and interlock system. However, there are some limitations, largely because of the limited address space of the LSI-11/23. The increasing demands for managing and monitoring 20 outlying nodes required the existing central node to be upgraded. The upgrade of the central node by a μVAX-II computer is in progress.

7b. BL-5

The beamline BL-5 has a front end made of components such as mask and light absorber, which must be designed to endure irradiation by the high photon flux from a multipole wiggler/undulator. The peak power density per unit solid angle from the wiggler is one order of magnitude as high as that from the bending magnet. The maximum horizontal divergence of wiggler radiation is ~7 mrad and a vertical opening angle ~2.7 mrad, so that the mask having an opening of 7 mrad will not be struck by wiggler radiation but by upstream bending radiation. The mask was designed to be water-cooled and slanted to the beam in order to tolerate bending radiation and wiggler radiation caused by an accidental orbit distortion. The wedge-shaped absorber with an angle of 18.4 degrees was installed to reduce the power density on its surface.

N. Kanaya

D. TRISTAN ACCUMULATION RING (AR)

1. CONSTRUCTION OF MULTIPOLE WIGGLER, EMPW#NE1

1a. Construction

A new multipole wiggler for elliptically polarized synchrotron radiation has been constructed on the basis of the previous proposal[1], and installed at the north symmetry point in the AR. It has vertical and horizontal pairs of magnet arrays with different field strengths in the pure type configuration as shown in Figs. 20 and 21.

The horizontal and vertical pairs share the same axis with a phase difference of 1/4 magnetic period. Since the magnetic material of the permeability very close to unity and the pure type configuration are chosen, the magnetic field in the device is given as a superposition of vertical and horizontal fields,

$$\mathbf{B} = \pm \mathbf{e}_x B_{xo} \cos \frac{2\pi z}{\lambda_u} - \mathbf{e}_y B_{yo} \sin \frac{2\pi z}{\lambda_u}, \quad (6)$$

where λ_u is the magnetic period length, and the coordinate system is taken as shown in Fig. 21. In Eq.(6), B_{xo} (B_{yo}) and $\mathbf{e}_x$ ($\mathbf{e}_y$) are the field amplitude and a unit vector in the x- (y-) direction, respectively. The direction of rotation of $\mathbf{B}$ along z-axis (i.e. the sign of the first term in Eq.(6)) can be changed by setting the phase difference +1/4 or -1/4 of the magnetic period. A relativistic electron traveling in the field given by Eq.(6) draws an orbit of a deformed helix on the surface of an elliptic cylindroid. The radiation from such an electron has an elliptic polarization with higher harmonics[1]. We call this multipole

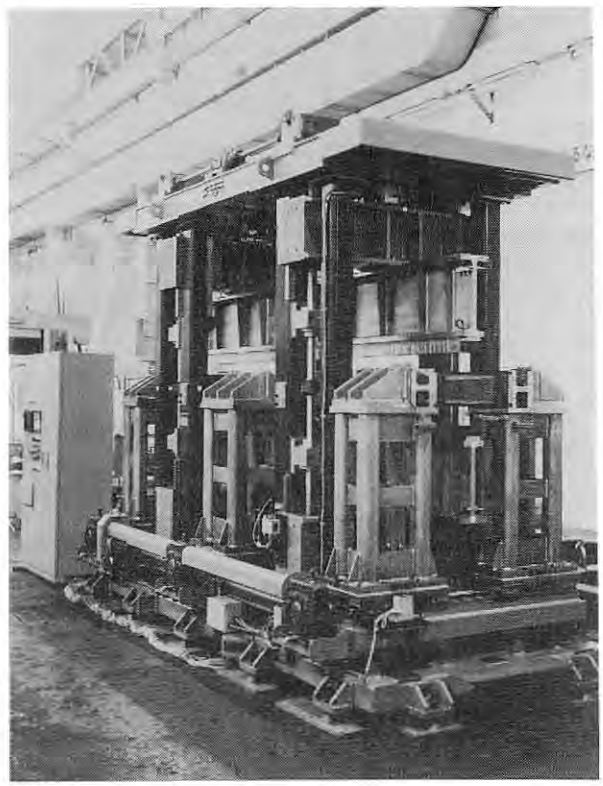

Fig. 20 A photograph of the multipole wiggler EMPW#NE1 constructed for the AR.

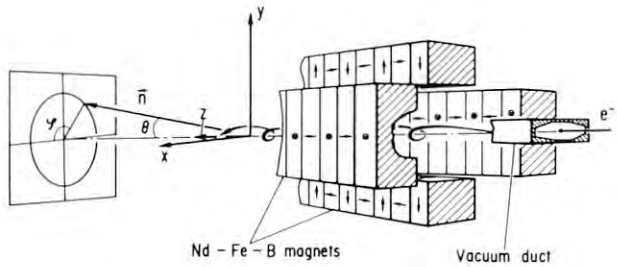

Fig. 21 Schematic illustration of EMPW#NE1. The arrow denotes the magnetization direction of each magnet.

wiggler EMPW#NE1 after an *elliptic* shape of the electron orbit, and the name of beamline *ARNE1*.

Magnetic specifications of EMPW#NE1 are listed in Table E-4 of Section E. The magnets of the multipole wiggler are made of NdFeB alloy which has the remanent field B_r=12 kG, the coercivity iH_c=17 kOe, and the magnetic permeability μ=1.05. The K-parameters are given as,

$$K_{x,y} = 9.34 \times 10^{-5} B_{xo,yo}\ (G)\ \lambda_u(cm), \quad (7)$$

where K_y (K_x) is for the vertical (horizontal) field. A maximum value of K_y=15 (K_x=3) is obtained when B_{yo}=9.7 kG (B_{xo}=2 kG) at a minimum vertical gap of 30 mm (horizontal gap of 110 mm). The field strength B_{xo} (B_{yo}) can be varied with the magnetic gap, from 110 to 400 mm (from 30 to 400 mm) in the horizontal (vertical) direction. The dependence of B_{xo} (B_{yo}) on the gap is shown in Fig. 22.

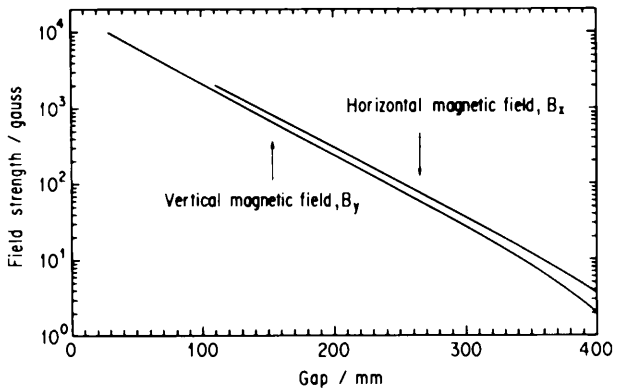

Fig. 22 Dependence of the magnetic field strength B_x (B_y) on the magnetic gap of EMPW#NE1.

The field was optimized with the following procedures. (1) With the data of measured magnetization vectors of individual magnets, magnet arrangement was determined using a similar algorithm proposed by Cox and Youngman[2]. (2) The deflections of the electron orbit at individual magnetic poles were optimized on the basis of precise field measurement so that the orbit corresponding to B_x (B_y) be close to the ideal sinusoidal curve. (3) Finally, the total deflection and deviation of the orbit generated by the whole wiggler were adjusted to be zero by the electromagnets attached at both ends of the devices. As a result, the range of K_x (K_y) from 0.5 to 3.0 (1.0 to 15.0) became available.

An extruded aluminum tube with an aperture of 24 mm high and 100 mm wide was used as a vacuum duct. The duct was suspended by tightly stretched tungsten wires, and evacuated at both ends of the duct by sputter ion pumps with the pumping speed of 200 l/sec.

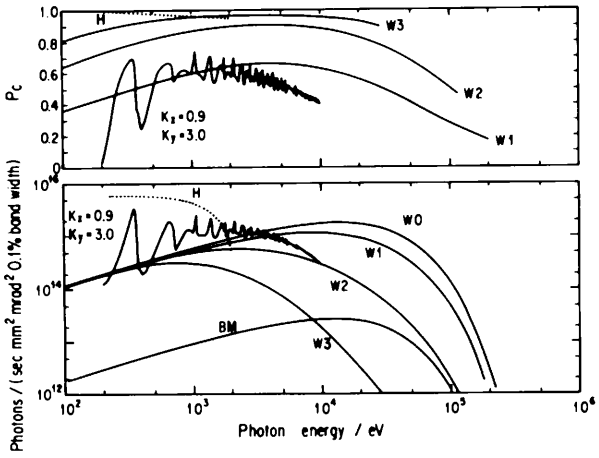

Fig.23 Calculated spectra and polarization characteristics of the radiation from EMPW#NE1. The W0, W1, W2 and W3 denote the wiggler modes (K_y=15) with K_x=0, 1, 2 and 3, respectively. A spectrum in the undulator mode with K_x=0.9 and K_y=3.0 is also shown. The H (dotted line) denotes the peak of the first harmonic with K_x=K_y ≤3.0, and BM the radiation from the bending magnet. The parameters of the low emittance mode are used in the calculation: 6 GeV, 50 mA, ε_x=1.3×10^{-7} mrad and ε_y=4.0×10^{-9} mrad.

The degree of circular polarization P_c and the brilliance[1] were calculated by taking into account the effect of the finite beam emittance. In the undulator mode, quasi-monochromatic radiation is available in the energy range from 40 eV to 5 keV with high P_c≈0.7 if the harmonics up to the 7th order are used. The brilliance is 10^2 to 10^3 times higher than that of linearly polarized radiation from a bending magnet (denoted by BM). In the wiggler mode with K_y =15.0, P_c increases as K_x is varied from 0 to 3.0, but the brilliance decreases. When K_x=1 to 2, we can obtain P_c=0.5 to 0.8 and the brilliance 1 to 100 times higher than that from the bending magnet.

1b. First Operation

After the commissioning of EMPW#NE1, the characteristics of the radiation in the hard X-ray region with K_y=15 were measured in the dedication mode of the AR in October 1988. Figure 24 shows the radiated photons observed at 35 m from the device with a fluorescence screen and a 7 mm-thick attenuator plate of Cu placed in front.

The bright lines on the screen reflected the helical motion of the electron (Fig. 21). The fattening of the elliptic pattern with increasing K_x shows the variation of the electron orbit from a sinusoidal plane motion to an elliptical motion. The pattern was separated into upper and lower parts, since the energy of radiation coming on the axis is not high enough

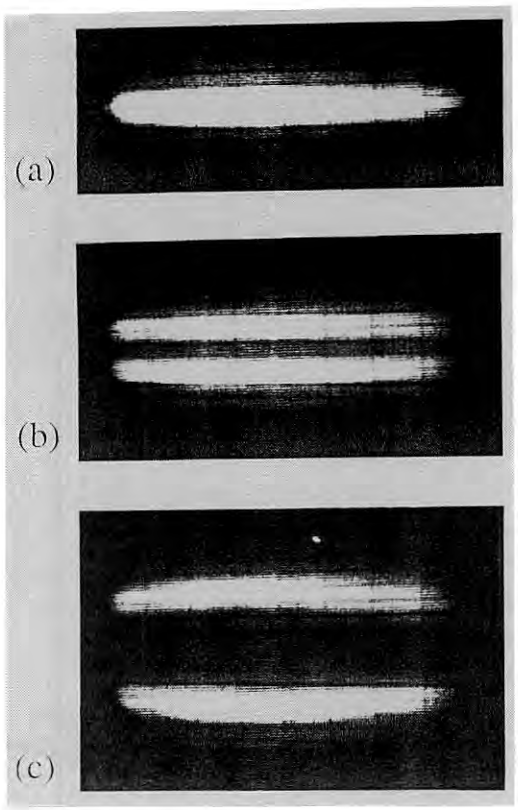

Fig. 24 Results of the exposure experiment of the radiation with K_y=15, and (a) K_x=0, (b) K_x=1.3 and (c) K_x=3.0.

to penetrate the Cu attenuator (Fig. 24 (b) and (c)). After the Cu attenuator was removed, the experiment of the magnetic Compton scattering from Fe[4] was made. It indicates that the radiation with $P_c \geq 0.7$ was obtained on the axis at the energy as high as 60 keV.

References
1) S. Yamamoto and H. Kitamura, Jpn. J. Appl. Phys. **26**, L1613 (1987).
2) A.D. Cox and B.P. Youngman, SPIE **582**, 91 (1985).
3) H. Kawata, this report.

S. Yamamoto

2. BEAMLINE AR-BL-NE1

A second beamline, the AR-BL-NE1 for EMPW#NE1 was constructed at AR. The front end is split into the following three branch lines;

(1) BL-NE1-A for high resolution Compton scattering and magnetic Compton scattering in the region of 50~70 keV.

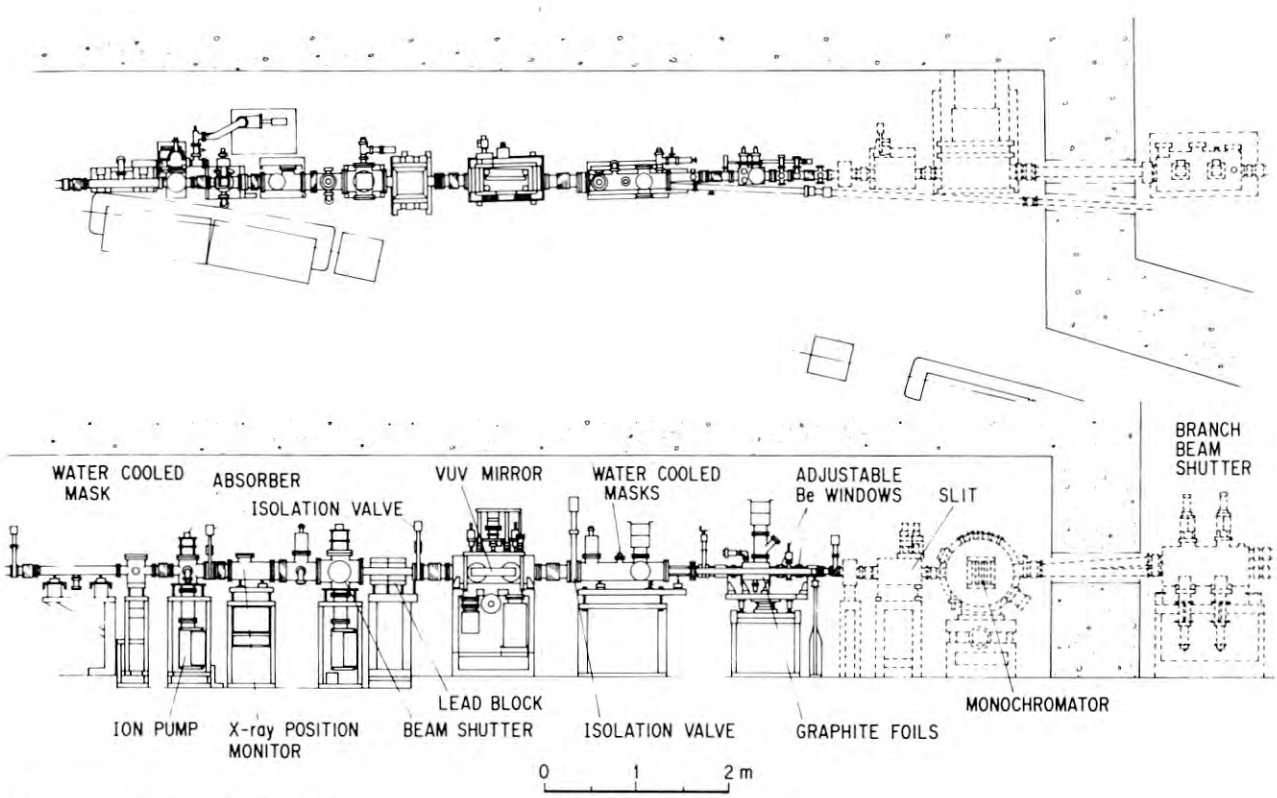

Fig. 25 Beamline AR-BL-NE1

(2) BL-NE1-B for magnetic Bragg scattering and magnetic absorption spectroscopy in the region of 6~100 keV.
(3) BL-NE1-C for monochromatic circularly polarized soft-X-ray in the region of 200 eV ~ 1.5 keV.

The layout of the AR beamline is shown in Fig. 25. Almost all the vacuum chambers are made of aluminum alloy. The beamline utilizes a 2.6 mrad horizontal divergence and 1.1 mrad vertical divergence of radiation with the maximum power of 3.7 kW. The front end consists of a manual gate valve, a water-cooled absorber, a pneumatic gate valve, a water-cooled beryllium window assembly, a beam shutter, a mirror chamber and vacuum components. In contrast to beamlines at the PF ring, an FCV is not necessary because it would take only a short time to recover the normal vacuum pressure ($\sim 10^{-9}$ Torr) from a vacuum failure. The beamline has the same interlock system as that for beamlines at the PF ring.

S. Sato

3. PHOTON BEAM POSITION MONITOR FOR AR-BL-NE1

A monitor of split emission chamber (SEC)[1] was installed in AR-BL-NE1 and located at 5 m away from the source point. The monitor was mounted in an independent small vacuum chamber with an aluminum window for SR beam. The pressure in the chamber was about 1 Pascal. Typical data of the photon beam position are shown in Fig. 26. The vertical position drifted 300 to 500 μm for about 30 min after the acceleration from 2.5 to 5.8 or 6.0 GeV. Sometimes a ripple of 20 to 30 μm on the drift was also observed.

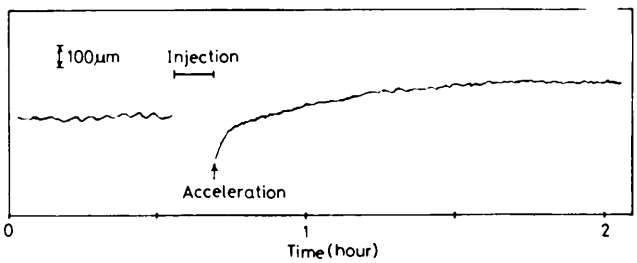

Fig. 26 Photon beam position at AR-BL-NE1.

Reference

1) T. Mitsuhashi, K. Haga and T. Katsura, Proceedings of IEEE particle accelerator conference p.576,1988

T. Mitsuhashi

References to be published in Rev. Sci. Instr. (Proc. SRI'88 Tsukuba, Japan)

1) "Low Emittance and Positron Storage Operation at the Photon Factory", K. Huke.
2) "Insertion Devices at the Photon Factory; Present Status and Future Development", H. Kitamura, S. Yamamoto and S. Kamada.
3) "Beam Position Stabilization at the Photon Factory", T. Katsura, Y. Kamiya, K. Haga, T. Mitsuhashi, N. Nakamura, M. Katoh and I. Abe.
4) "Apparent Displacement of the Synchrotron Radiation Beam on Beamline 4 of the Photon Factory Storage Ring", T. Katsura, Y. Kamiya, T.Mitsuhashi, N. Nakamura, K. Haga and A. Iida.
5) "Differences in Quality of PF Ring Vacuum Between Positron and Electron Storage Mode", M. Kobayashi, Y. Hori and Y. Takiyama.
6) "Suppression of Beam Instabilities Induced by Accelerating Cavities", H. Kobayakawa, M. Izawa, S. Sakanaka and S. Tokumoto.
7) "Construction of Insertion Devices for Elliptically Polarized Synchrotron Radiation", S. Yamamoto, T. Shioya, S. Sasaki and H. Kitamura.
8) "Construction and Operation of the Multipole Wiggler, MPW#16, at the Photon Factory", T. Shioya, S. Yamamoto, S. Sasaki, M. Katoh, Y. Kamiya and H. Kitamura.
9) "Construction of a Multipole Wiggler, MPW#13, at the Photon Factory", S. Sasaki, S. Yamamoto, T. Shioya and H. Kitamura.
10) "Construction of a Multi-Undulator, Revolver #19, at the Photon Factory", G. Isoyama, S. Yamamoto, T. Shioya, H. Ohkuma, S. Sasaki, T. Mitsuhashi, T. Yamakawa and H.Kitamura.
11) "A Beryllium Window Assembly for the 53-Pole Wiggler Beamline at the Photon Factory", S. Sato, S. Asaoka, I. Nagakura and N. Kanaya.
12) "Design and construction of Beam Line-NE1 for circularly polarized synchrotron radiation from the 6 GeV TRISTAN Accumulation Ring", H. Kawata T. Miyahara, S. Yamamoto, T. Shioya, H. Kitamura, S. Sato, S. Asaoka, N. Kanaya, A. Iida, A. Mikuni, M. Sato, T. Iwazumi, Y. Kitajima and M. Ando.

E. LIGHT SOURCE SPECIFICATIONS

This section contains major specifications of the PF and AR rings to provide quick and handy information for users and machine physicists.

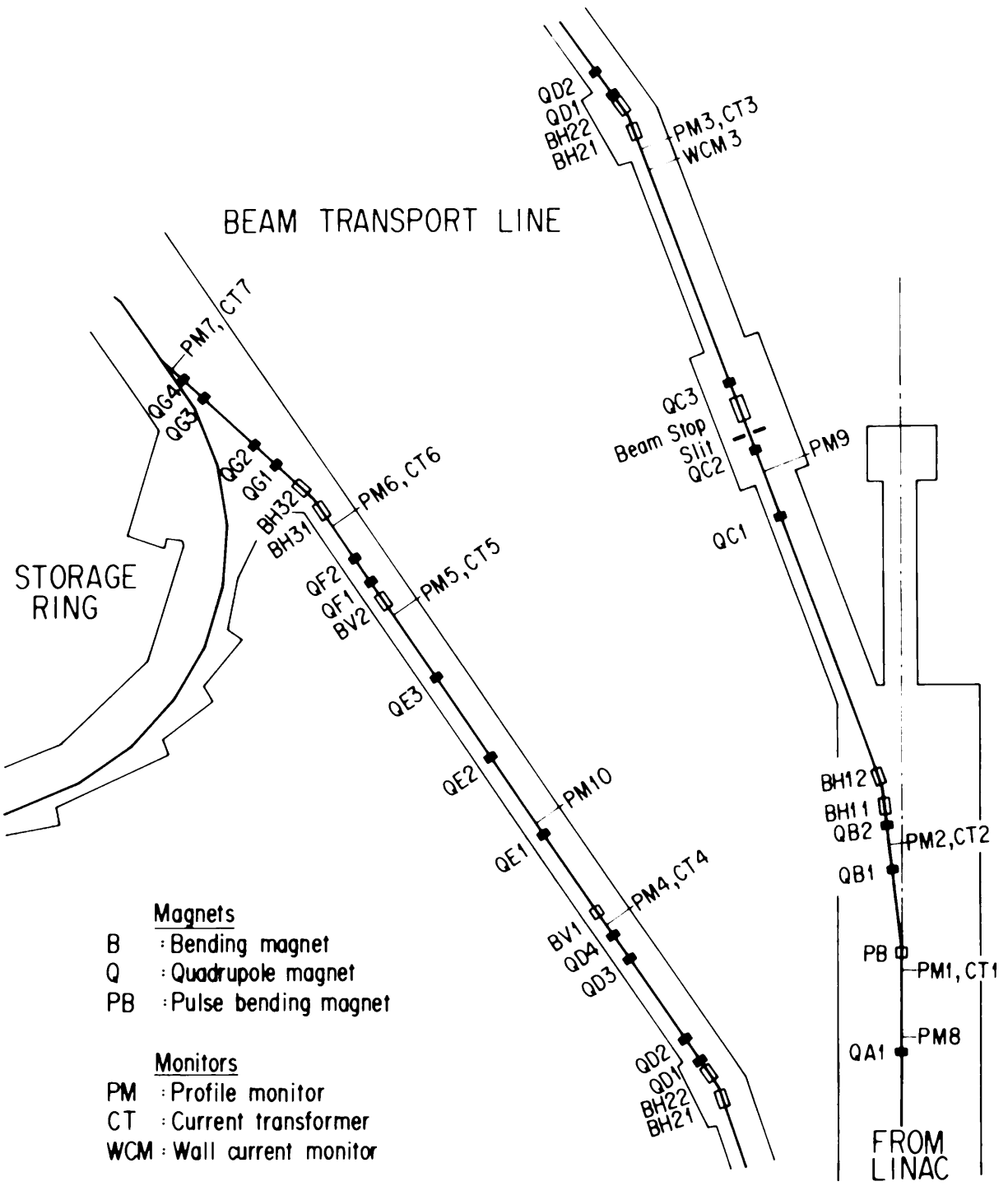

Fig. E-1 Beam transport line

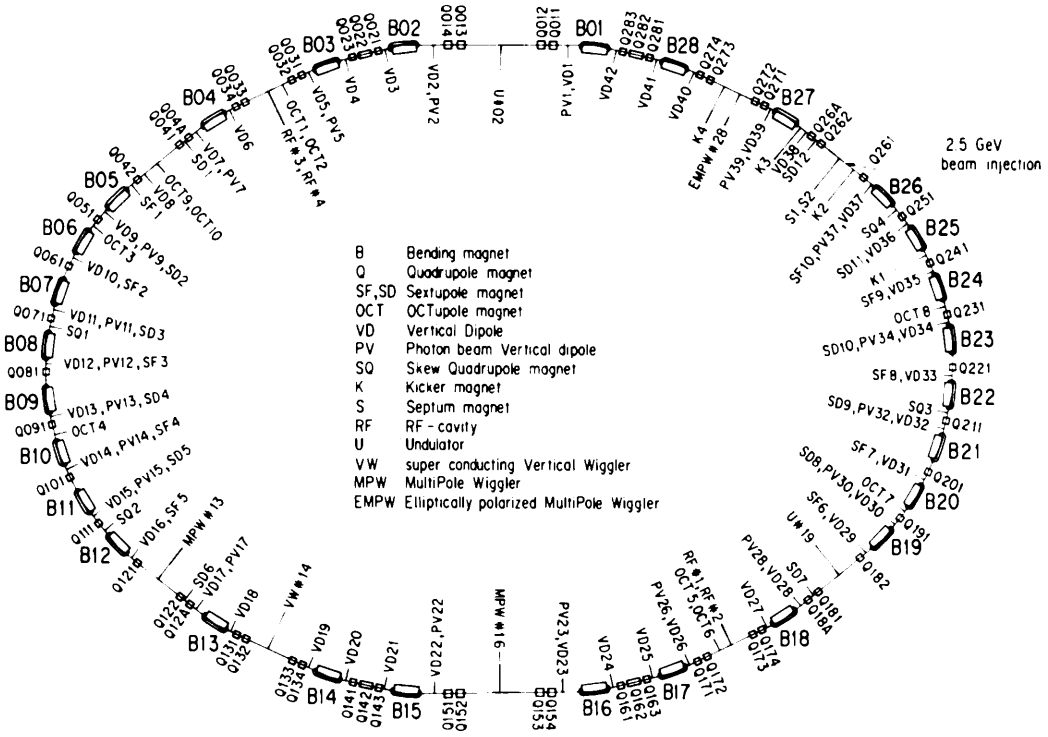

Fig. E-2 Ring lattice components

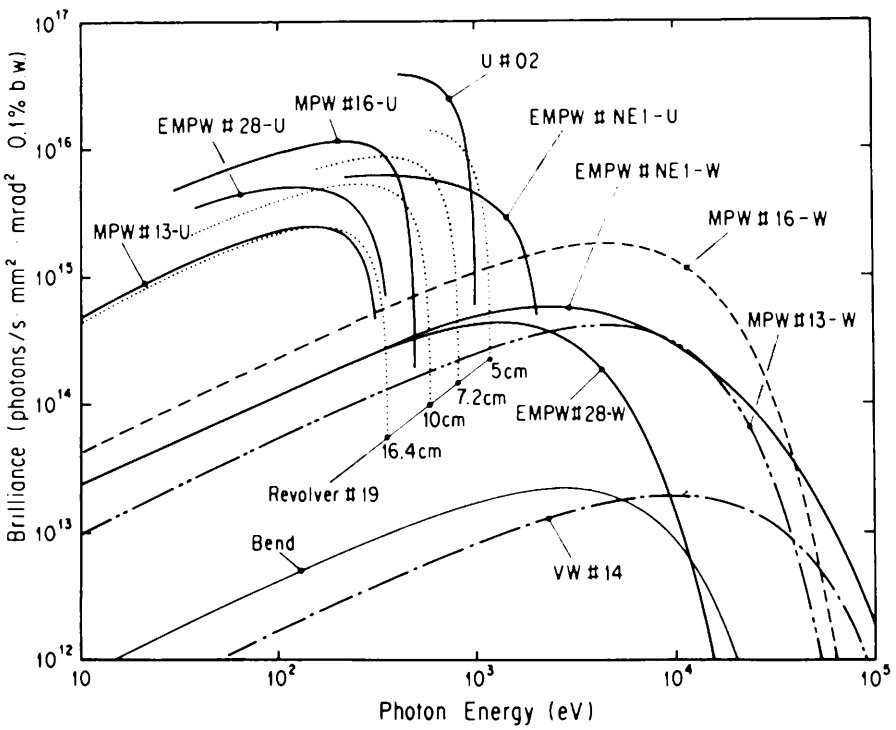

Fig. E-3 Synchrotron radiation spectra

Brilliance of radiation vs. photon energy for the insertion devices (U#02, MPW#13, VW#14, VPW#16, Revolver#19 and EMP#28) and the bending magnet (Bend) of the PF, and for the insertion device (EMPW#NE1) of the AR. The name of each source is assigned in Table E-1. Several insertion devices have both undulator and wiggler modes, which are denoted by U or W, respectively. The spectral curve of each undulator (or undulator mode of multipole wiggler) is a locus of the peak of the first harmonic within the allowable range of K-parameter. Spectra of Revolver#19 are shown for four kinds of period lengths.

Table E-4 Insertion devices

Calculated spectra from the bend source and 6 insertion devices, and one insertion device at the PF E/I: beam energy and current, λ_u: period length, N: number of periods, L: length of undulator or wiggler, $G_y(G_x)$: minimum vertical (horizontal) gap height, $B_y(B_x)$: maximum vertical (horizontal) magnetic field, P: pure configuration, H: hybrid configuration, S.C.: superconducting magnet, $\sigma_{x,y}$: horizontal or vertical beam size, $\sigma_{x,y}$: horizontal or vertical beam divergence, $K_y(K_x)$: horizontal (vertical) deflection parameter, $\varepsilon_1/\varepsilon_c$: photon energy of the first harmonic and critical energy of band source or wiggler, P_c: degree of circular polarization, ℬ: brilliance (photons/s·mm^2·mrad^2·0.1%b.w.), P_T: total radiated power, P_D: angular power density (kW/mrad^2). Different operating modes of undulator and wiggler are denoted by U and W, respectively.

Name	E/I GeV/mA	λ_u cm	N	L m	$G_y(G_x)$ cm	$B_y(B_x)$ T	Type of magnet	σ_x mm	σ_y mm	$\sigma_{x'}$ mrad	$\sigma_{y'}$ mrad	Energy range keV	$K_y(K_x)$	$\varepsilon_1/\varepsilon_c$ keV	ℬ	P_T kW	P_D
Bend	2.5/250							0.75	0.33	0.39	0.047	<30		4.0	2.1E13		0.043
U#02		6.0	60	3.6	2.8	0.3	P($SmCo_5$)	0.63	0.22	0.20	0.017	0.4～3	1.7	0.40	3.7E16	0.33	1.3
MPW#13-W		18.0	13	2.5	2.7	1.5	H(NdFeB)	1.65	0.21	0.15	0.023	<70	25.0	6.2	4.4E14	5.0	2.1
-U												0.03～1	1.0	0.22	2.0E15	0.01	0.042
VW#14					5.0	5.0	S.C.	1.17	0.15	0.19	0.026	<100		20.8	1.6E13	8.8	0.17
MPW#16-W		12.0	26	3.1	1.9	1.5	H(NdFeB)	0.63	0.22	0.20	0.017	<70	16.8	6.2	1.8E15	7.1	4.5
-U												0.03～1	1.0	0.33	9.4E15	0.02	0.12
Revolver		5.0	46	2.3	3.0	0.28	H(NdFeB)	1.65	0.21	0.15	0.023		1.3	0.64	1.3E16	0.18	0.89
#19		7.2	32			0.41	H(NdFeB)					0.007～1.1	2.7	0.18	7.3E15	0.37	1.3
		10.0	23			0.53	H(NdFeB)						5.0	0.044	2.5E15	0.66	1.3
		16.4	14			0.62	P(NdFeB)						9.5	0.0078	4.2E14	0.88	0.97
EMPW#28		16.0	12	1.9	3(11)	1(0.2)	P(NdFeB)	1.17	0.15	0.19	0.026						
-W												<15	15(1)	4.2(Pc=89%)	1.8E14	1.9	1.1
-U												0.04～0.35	1(1)	.18(Pc=99%)	4.0E15	0.02	0.069
EMPW#NE1		16.0	21	3.4	3(11)	1(0.2)	P(NdFeB)	0.95	0.08	0.14	0.053						
-W	6.0/50											<100	15/2	24(Pc=80%)	9.1E13	3.8	8.5
-U												0.2～2	1/1	1.1(Pc=97%)	3.5E15	0.03	0.52

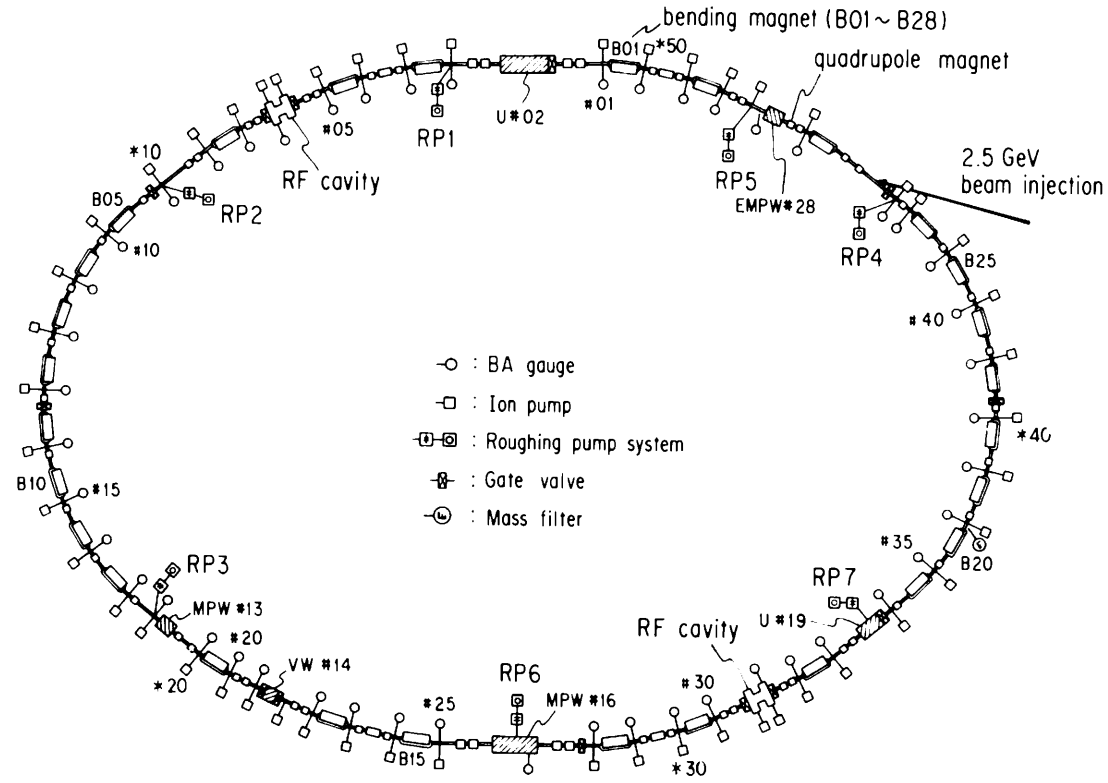

Fig. E-5 Vacuum system components

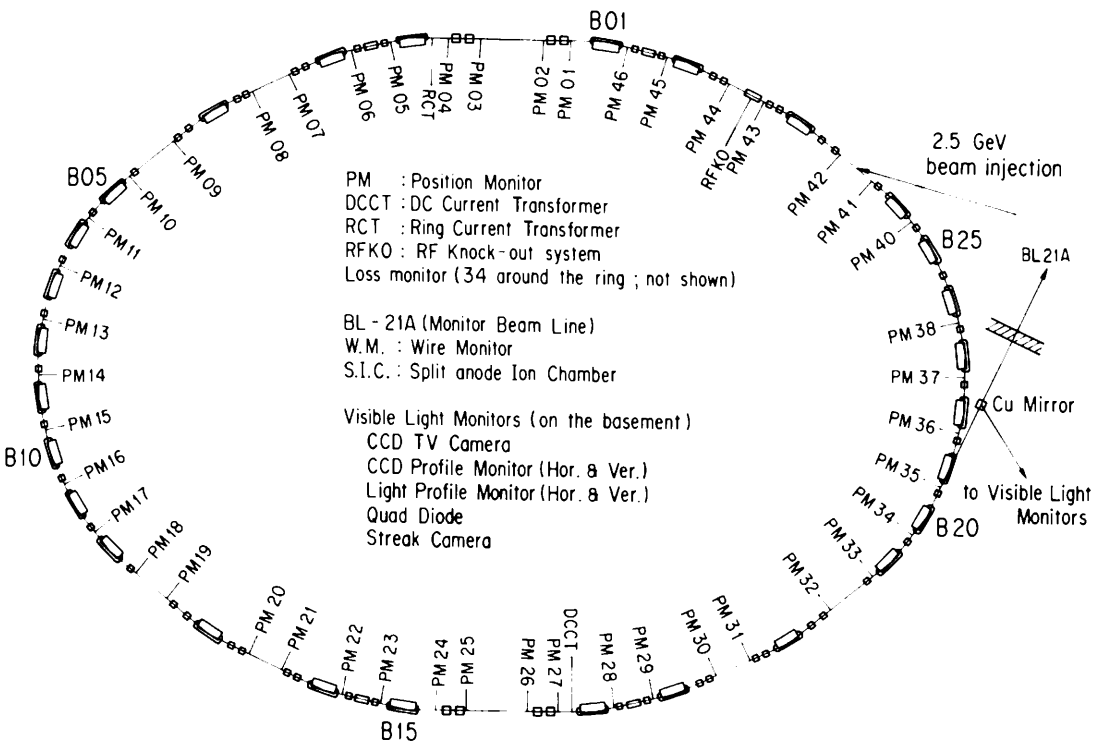

Fig. E-6 Beam monitors

Table E-7 General parameters of the storage ring

Energy	2.5 GeV	(1.6 GeV to 3 GeV)
Initial stored current	300 mA	(250 mA with vertical wiggler) (max. 360 mA)
Emittance	130nm·rad(horizontal) ~2nm·rad(vertical)	
Circumference	187m	(bending radius=8.66m)
RF frequency	500MHz	(harmonic number=312)
Injection	2.5GeV Linac	(positron/electron)
Beam lifetime	20hrs (at 200mA),	30hrs (at 150mA)
Vacuum pressure	2.5×10^{-10}Torr (at 250mA) 1.5×10^{-10}Torr (at 150mA) 3.0×10^{-11}Torr (at 0mA)	
Insertion devices	Superconducting vertical wiggler 5T 60 period undulator K=1.78~0.1 26 period multipole wiggler/undulator 1.5T~0.04T Four way revolver type undulator 14 period multipole wiggler Elliptically polarized multipole wiggler	
SR channels	SR experiment 20 (5 under installation, 1 under design) Beam diagnosis 3	

Table E-8 Beam parameters

Horizontal tune ν_x	8.38
Vertical tune ν_y	3.14
Compaction factor α	0.015
Natural chromaticity ξ_x	-15.8
ξ_y	-8.6
Bunch length σ_z	1.5cm
Transverse damping time	7.8msec
Longitudinal damping time	3.9msec
Energy spread	7.3×10^{-4}
Radiation loss	400keV

Table E-9 Principal parameters of the accelerator system

Magnet system

	number of magnets	number of power supplies
Bending	28	1
Quadrupole	58	12
Sextupole	22	2
Octupole	11	10
Skew quadrupole	4	4
Vertical steering	42	42
Photon beam steering	20	20
Others		
Backleg winding of bending magnet	28	
Electric shunt for tune compensation	8	

RF system

Number of RF stations	2
Number of klystrons	2 (180kW/klystron)
Number of RF cavities	4 (single cell cavity)
Shunt impedance	32MΩ (four cavities)
Unloaded Q	39000
Total power dissipated in cavity wall	89kW
Total cavity gap voltage	1.7MV
Synchrotron frequency	37kHz

Vacuum system

main pumping system

pump	pumping speed	number
SIP (Sputter Ion Pump)	128 l/sec	50
DIP (Distributed Ion Pump)	150 l/sec	28
Ti sublimation	---------	53

total effective pumping speed = 2×10^4 l/sec (for CO)

Rough pumping system

	pumping speed	number
TMP (Turbo Molecular Pump)	300 l/sec	7

Measurement

	number
B-A gauge	48
mass filter	1
cold cathode gauge	12 (for baking)

Sector gate valve

	number
all metal with RF shield	3
all metal without RF shield	4
Viton seal with RF shield	6

Injection system

Septum magnet

name	Septum I (S1)	Septum II (S2)
core material	laminated silicon steel	
length [mm]	1500	1000
maximum current [A]	6000	6000
deflection angle [degree]	7.0	5.0
pulse width [μsec]	88	60

Kicker magnet

name	K1 , K2 , K3 , K4
core material	ferrite (window frame type)
core length [mm]	300
maximum current [A]	5000
maximum deflection angle [mrad]	6.3
pulse width [μsec]	6

Superconducting vertical wiggler

number of poles	3
total length of the magnet	800 mm
length between the coil centers	300 mm
number of turn of the coils	3204 (central coil)
	1113 (lateral coil)
maximum magnetic field	6T
operating magnetic field	5T (current = 121A)
conductor material	NbTi/Cu
helium dissipation rate	4 l/hour

Monitor system

PM(Position Monitor)	45
RCT(Ring Current Transformer)	1
DCCT(Direct Current Current Transformer)	1
RFKO(Radio Frequency Knock-Out system	1
LS(Loss monitor)	43
Visible Light Monitor	
CCD TV Camera	
CCD Profile Monitor (H&V)	1
Light Profile Monitor (H&V)	1
Quad Diode	1
BL-21A(Monitor Beam Line)	
W.M. (Wire Monitor)	1
S.I.C. (Split anode Ion Chamber)	1

Control system

		number	memory
Control computers	FACOM S-3500	1	16 Mbyte
	FACOM S-3300	3	8 Mbyte
Library computer	FACOM M-360MP	1	24 Mbyte
computer network (type : optical token ring)			
number of nodes = 5 (max. 64)			

Table E-10 Beam size and divergence at source point

location	σ_x [mm]	σ_y [mm]	σ'_x [mrad]	σ'_y [mrad]
B15&B01	0.53	0.09	0.35	0.038
B02&B16	0.84	0.07	0.33	0.038
B03&B17	0.54	0.20	0.33	0.013
B04&B18	0.49	0.21	0.37	0.038
B05&B19	1.51	0.21	0.47	0.038
B06&B20	0.78	0.25	0.43	0.039
B07&B21	1.31	0.21	0.40	0.037
B08&B22	0.80	0.25	0.38	0.038
B09&B23	1.21	0.20	0.39	0.038
B10&B24	0.88	0.25	0.39	0.037
B11&B25	1.25	0.21	0.44	0.039
B12&B26	0.99	0.26	0.46	0.038
B13&B27	0.38	0.25	0.39	0.038
B14&B28	0.82	0.21	0.31	0.013

Table E-11 General parameters of the Accumulation Ring

Energy		6.0 GeV (2.5 GeV to 8 GeV)
Initial stored current		20 mA (max. 50 mA)
Emittance		130 nm·rad (horizontal)
		~ 2 nm·rad (vertical)
Circumference		377 m
Long straight sections		2 × (19.5 + 19.1) m
rf frequency		508.6 MHz
Bending radius		23.2 m
Number of bending magnets		72
Energy loss per turn		4.85 MeV
Damping times	τ_x	3.11 ms
	τ_y	3.11 ms
	τ_E	1.56 ms
Partition numbers	J_x	1.0
	J_E	2.0
Natural energy spread		1.06E-3
Momentum compaction factor		7.1E-3
Natural chromaticity	ξ_x	-22.2
	ξ_y	-12.8

Table E-12 Summary of Beamline in FY 1988

Beamline	Affiliation	Source	Spectral range	Status
BL-1	NTT	bending magnet (B1)	VUV and Soft X-ray	in operation
BL-2	KEK-PF	60-period permanent magnet undulator	Soft-X-ray	in operation
BL-3	KEK-PF	bending magnet (B3)	VUV and Soft X-ray	under installation
BL-4	KEK-PF	bending magnet (B2)	X-ray	in operation
BL-5	KEK-PF	permanent magnet wiggler/undulator (under design)	VUV and Soft X-ray	under installation
BL-6	KEK-PF	bending magnet (B6)	X-ray	in operation
BL-7	University of Tokyo	bending magnet. (B7)	VUV and X-ray	in operation
BL-8	Hitachi Ltd.	bending magnet (B8)	VUV and X-ray	in operation
BL-9	Nippon Electrical Co. (NEC)	bending magnet (B9)	VUV and X-ray	in operation
BL-10	KEK-PF	bending magnet (B10)	X-ray	in operation
BL-11	KEK-PF	bending magnet (B11)	VUV and Soft X-ray	in operation
BL-12	KEK-PF	bending magnet (B12)	VUV	in operation
BL-13	The Institute of Physics and Chemical Research*)	27-pole multipole wiggler	Hard X-ray	under installation
BL-14	KEK-PF	superconducting vertical wiggler	Herd X-ray	in operation
BL-15	KEK-PF	bending magnet (B15)	X-ray	in operation
BL-16	KEK-PF	53-pole permanent magnet wiggler/undulator	Soft X-ray	in operation
BL-17	Fujitsu Ltd.	bending magnet (B17)	VUV and X-ray	in operation
BL-18	ISSP and KEK-PF	bending magnet (B18)	VUV and X-ray	under installation
BL-19	ISSP and KEK-PF	permanent magnet multi-undulator	VUV	in operation
BL-21	KEK-PF	bending magnet (B21)	white, visible light and X-ray (branch line)	in operation
BL-27	KEK-PF	bending magnet (B27)	VUV and X-ray	under design
BL-28	KEK-PF	25-pole permanent magnet wiggler/undulator	circularly polarized VUV and Soft X-ray	under installation
AR Test Port	KEK-PF	bending magnet of Accumulation Ring (AR)	Hard X-ray	in operation
AR-BL-1	KEK-PF	41-pole multipole wiggler	Hard X-ray and Soft X-ray	in operation

*) Branch lines are constructed by following national institutes; National Research Laboratory of Metarology, National Institute of Researches in Inorganic Materials, Electrotechnical Laboratory, and National Chemical Laboratory for Industry

Instrumentation Department

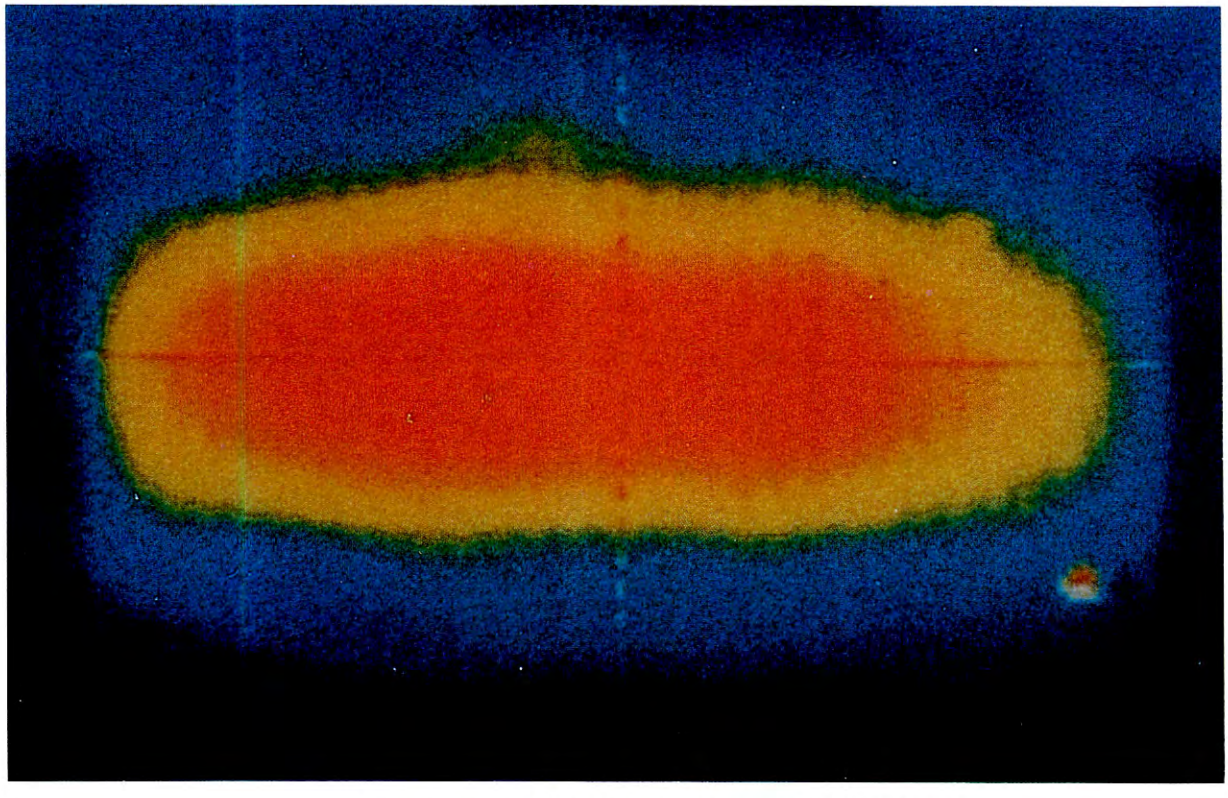

Thermal image of the surface of the directly water-cooled monochromator crystal on BL-16 multipole wiggler beamline.

INSTRUMENTATION DEPARTMENT

A. INTRODUCTION

Nine new beamlines with eighteen experimental stations have been designed, constructed or nearly completed at the 2.5-GeV Photon Factory storage ring and the 6-8 GeV TRISTAN Accumulation Ring. Some of these beamlines were built under collaborations between the Photon Factory and other institutes: beamline 18 and 19 with The Institute for Solid State Physics, University of Tokyo, and beamline 13 with five national institutes of Science and Technology Agency and Ministry of International Trade and Industry. The new beamlines are summarized in Table 1 with their present status, characters and purposes.

Most remarkable is that six of these are beamlines for various kinds of insertion device such as multipole wiggler, undulator and circular polarization multipole wiggler/undulator.

The BL-16 and BL-13 are both high-power multipole wiggler/undulator beamlines with multi-branch system for the time sharing uses of both X-ray and VUV or soft X-ray radiation. The BL-19 is a multi-undulator beamline for use of the VUV and soft X-ray radiation. The beamline AR-NE3 has a special importance because it is the first X-ray beamline for making use of radiation from an undulator installed in the high energy storage ring.

A particular remark should be made about the AR-NE1 and BL-28 because they are the beamlines for making use of the circularly polarized wiggler radiation in the X-ray and VUV regions. Such beamlines will offer new possibilities in studies of magnetic materials with the spectroscopic, diffraction and scattering techniques.

The situation of such expanding forefronts, on the other hand, has given us a chance to review and check the beamlines for normal bending magnet sources. New bending magnet beamlines must be designed, hereafter, with purpose-oriented character. The BL-3 and BL-18 are the first beamlines constructed along this guideline. The branch beamline BL-12C is a multilayer reflector beamline reconstructed for studies of photochemical reactions.

As many insertion device beamlines are commissioned, it has been getting more and more urgent to develop thermo-resistant optical devices in the VUV, soft X-ray and hard X-ray regions. On the BL-16, an effective way of crystal cooling is being pursued to avoid degradation of the monochromator due to thermal deformation. An SiC grating is also being developed for use on the BL-16 undulator branch.

In parallel to the above, improvements of working beamlines have been steadily continued and some new experimental apparatuses have been also developed or completed. Imaging plate detectors are now widely and routinely used by users at the Photon Factory. A fast one-dimensional X-ray detector has been developed by making use of the imaging plates. An electron-ion coincidence spectrometer is an apparatus for use of undulator radiation.

Table 1. New Beamlines at the Photon Factory

Beamline	Status	Source		Range	Remarks
PF-BL-3A	C(PF)	B	X	4-20 keV	4-circle diffractometer.
-3B	C(PF)	B	VUV-SX	10-300 eV	Atomic & molecular spectroscopy, Surface APRES.
-3C	C(PF)	B	X	---	Beam diagnostics.
-12C	RC(PF)	B	VUV-SX	60-90 eV	Multilayer reflector, Photo-CVD.
-13A	C(STA)	MPW	X	4-50 keV	High precision lattice parameter measurement.
-13B1	C(STA)	MPW	X	4-50 keV	EXAFS & surface diffraction.
-13B2	C(STA)	MPW	X	10-50 keV	High pressure diffraction.
-13C	D(STA)	U	VUV-SX	200-1000 eV	Soft X-ray (S)EXAFS.
-16X	C(PF)	MPW	X	4-50 keV	General purpose.
-16U	C(PF)	U	VUV-SX	40-600 eV	High flux & high resolution spectroscopy.
-18A	C(ISSP)	B	VUV-SX	6.5-350 eV	Surface & interface analysis.
-19A	C(ISSP)	U	VUV-SX	12.5-250 eV	Spin polarized PES.
-19B	C(ISSP)	U	VUV-SX	10-1200 eV	PES on phase transition.
-28B	C(PF)	U	CP-V-SX	5-300 eV	PES of magnetic materials.
AR-BL-NE1A1	C(PF)	MPW	CP-X	50-70 keV	Magnetic Compton scattering.
-NE1A2	C(PF)	MPW	CP-X	6-100 keV	General purpose
-NE1U	C(PF)	U	CP-SX	250-1500 eV	Spectroscopy of magnetic materials.
-NE3A1	D(PF)	U	X	10-20 keV	Nuclear Bragg scattering.
-NE3A2	D(PF)	U	X	5-20 keV	Surface diffraction.

C: Under construction, D: In designing, RC: Reconstruction, B: Bending magnet,
MPW: Multipole wiggler, U: Undulator, CP: Circular polarization, PF: Photon Factory,
ISSP: The Institute for Solid State Physics, STA: Science & Technology Agency.

Descriptions are made in this chapter on the new beamlines, improvements of working beamlines and new experimental apparatuses including lists of all experimental stations and apparatuses, and summary tables of the beamline optics.

H. Maezawa & T. Matsushita

B. NEW BEAMLINES

1. BL-16, A Multipole Wiggler/Undulator (MPW/U) Beamline.

Bl-16 transports radiation from a 3.6-m long, 53-pole wiggler/undulator. The insertion device has hybrid permanent magnets with a period of 12 cm and a maximum magnetic field of 1.47 Tesla. Under the undulator mode, the energy of the fundamental peak can be varied from 40 to 400 eV. The typical total emitted power is about 1 kW for undulator-mode operation with a magnet gap of 50 mm (K = 5.8) and ring operation at 2.5 GeV and 300 mA. Under the wiggler mode, an X-ray beam (critical energy of 6 keV) 50 - 100 times more intense than that from the bending magnets is obtained. The total radiated power is 8.36 kW at 1.47 Tesla, 2.5 GeV and 300 mA.

The beamline consists of two time-shared branch lines: a side beamline for soft X-rays under the undulator operation, to which photon beams are deflected sideways by a cylindrical SiC mirror, and a straight line for hard X-rays under the wiggler operation. A plan view of the beamline is shown in Fig. 1 and optics on these two branches are schematically shown in Fig. 2.

The optics on the undulator branch line consist of five optical components; (1) a cylindrical SiC mirror, (2) a vertical deflection mirror for directional matching, (3) a cylindrical mirror with a major radius of curvature of 1.8 m, (4) a 2-m concave grating, and (5) a refocusing-mirror of a bent-cylinder. In the design of this optics, we intended to decouple horizontal focusing from vertical dispersion to have better focusing of the source image on the exit slit and then to achieve a high resolution compatible with the high output flux. The M_0 SiC mirror gives a 5:3 horizontal focusing of the source image on the exit slit. With a combination of the M_2 mirror and the grating satisfying the second-order focusing condition, it was possible to make the monochromator entrance-slitless even in a very asymmetric configuration between the source-to-monochromator and monochromator-to-exit slit distances. The refocusing mirror M_3 forms a 1:1 image of the exit slit on the target point of experimental apparatus. In a preliminary test of the monochromator, a replica grating was severely damaged with an hour exposure to the undulator beam. We intend to replace this grating with a SiC grating now under

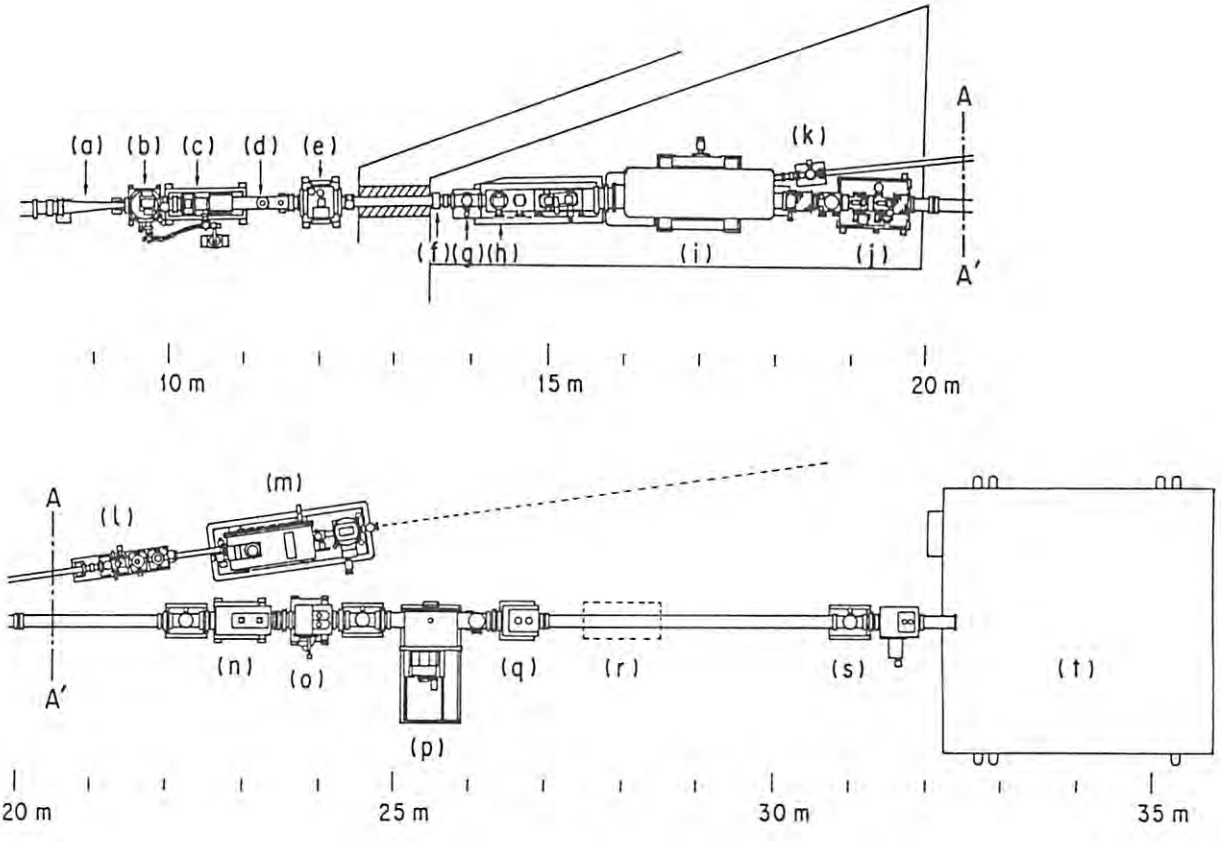

Fig. 1. Plan view of the beamline BL-16.

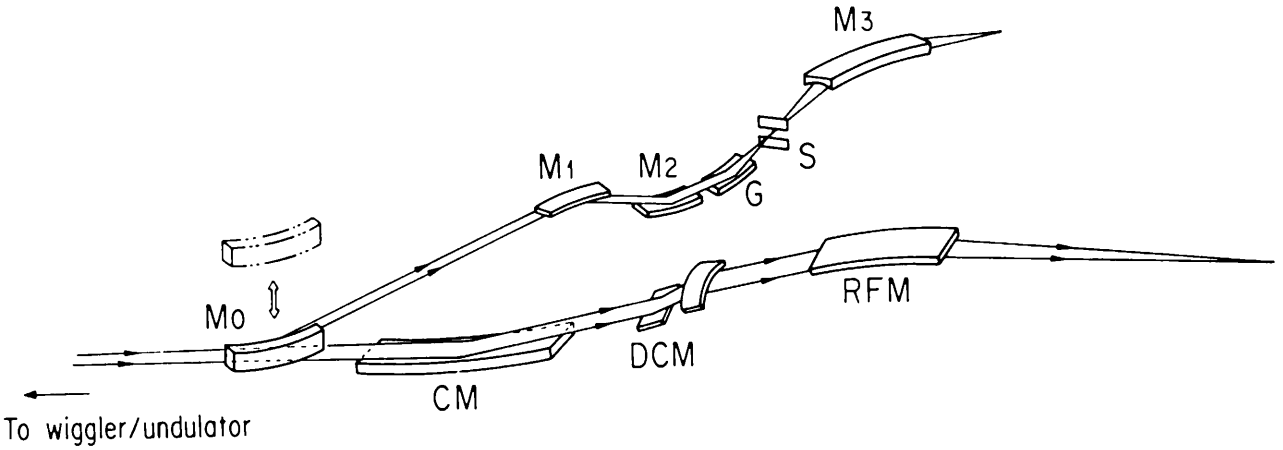

Fig. 2. Optical arrangement of the branch beamlines BL-16X and BL-16U.

development.

Under the wiggler mode, the SiC mirror is removed from the optical axis and X-ray beams are transported to the straight line through graphite filters (the total thickness of 0.78 mm) and two berillium-windows (0.2 mm thick each). The longer wavelength component of synchrotron radiation is absorbed by these graphite filters and Be windows and the total power of the beam hitting the first crystal of the double crystal monochromator was measured to be 1.6 kW.

The X-ray optics designed for X-ray branch beamline is also schematically shown in Fig. 2. It has a collimating mirror, a fixed-exit sagittal-focusing double-crystal monochromator and a refocusing mirror. By summer of 1988, only the double crystal monochromator has been installed 25.5 m from the source and has been commissioned. Two mirrors will be installed in 1989. The first crystal of the monochromator has semi-circular shaped channels under the reflecting surface for direct water cooling, as shown in Fig. 3. Test of this directly water-cooled crystal was made in June 1988 in collaboration with Tom Oversluizen and Pete Stefan from NSLS. We measured temperature of the reflecting surface, rocking curves and topographic observation. Fig. 4 shows correlation of data for the crystal having 0.7 mm wide channels and 1.5 mm thick fins. The surface temperature rose up to 38°C with the Wiggler field strength of 1.47 Tesla and the ring operation at 2.5 GeV and 225 mA. The rocking curve width is broadened to 25 arc sec. This is because the crystal was bent to an radius of curvature of 180 m as can be understood from the 333 topographs shown in Fig. 4. Further efforts to solve this problem are being continued. A cylindrically bent crystal will be used as the second crystal in order to focus the beam in the horizontal direction. The vertically collimating mirror will be placed 17 m from the source and consists of three flat SiC pieces (500 × 140 × 25 mm each), the flatness and the r.m.s. roughness of which are better than $\lambda/10$ over the whole area of the mirror and less than 6A, respectively. Surfaces of these mirrors are platinum coated. These three mirrors will be clumped to an I-beam to form a 1.5 m long mirror surface. The I-beam will be bent to form a parabolic surface. It can also be bent to form a cylindrical surface with a radius of curvature of approximately 5 km and can be used as a one-to-one vertically focusing mirror. The cut-off energy of the mirror will be chosen to be around 20 keV. A refocusing mirror will be made of three pieces of flat fused quartz plates. The same bending mechanism as the collimating mirror will be used.

Ray tracing results showed that the vertical divergence of 4 arc sec is expected by the collimating mirror. With the refocusing mirror and the sagittal focusing crystal, a focal spot size of 1.5 mm × 0.5 mm is expected at the sample position.

T. Matsushita

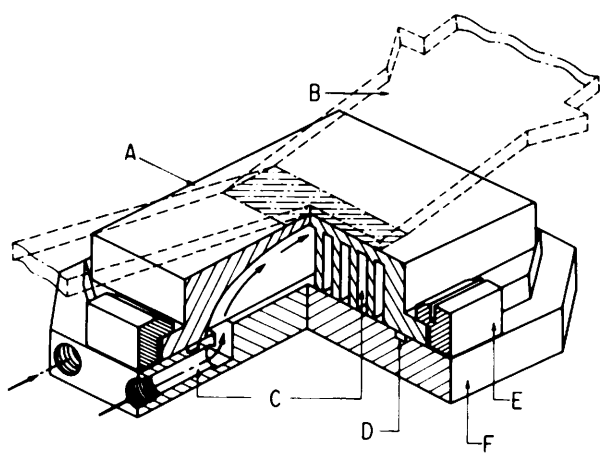

Fig. 3. Crystal cooling scheme of the BL-16X double crystal monochromator.

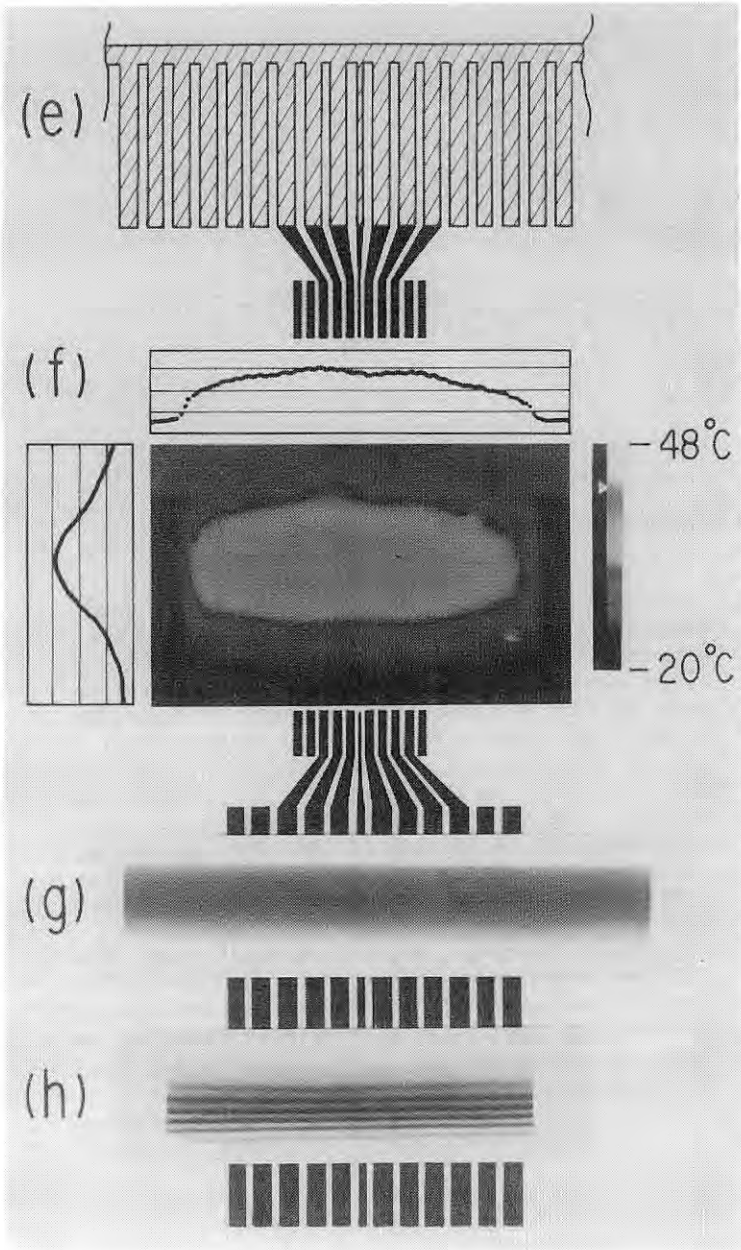

Fig. 4. (e): Cross-section of the directly-water-cooled crystal, (f): thermal image of the crystal surface, (g): Si(111) topograph, and (h): Si(333) topograph (zebra pattern).

2. BL-19, A Multi-undulator, Revolver, Beamline of ISSP

Construction of the BL-19 was completed in 1988 under collaboration between Synchrotron Radiation Laboratory of the Institute for Solid State Physics, the University of Tokyo, and the Photon Factory. The beamline was specially designed to accept radiation emitted from a multi-undulator[1] and to lead radiation into two branch beamlines, BL-19A and BL-19B. The beamline consists of a front end, a mirror system and monochromators. All the parts of the beamline were constructed under considerations to minimize the damage of optical elements by the heat load of the high power radiation from the insertion device and to avoid troubles by the vacuum hazard.[2]

The basic design of the front end is similar to those of other VUV beamlines in PF-ring.[3] It is equipped with an absorber, a fast closing valve, an acoustic delay line, a main beam shutter, water cooled masks, valves for vacuum isolation, etc. The front end accepts 7.0 mrad horizontal and 3.5 mrad vertical divergences of the undulator radiation.

The mirror system consists of three mirrors (M_{A1}, M_{A2} and M_B) in water-cooled adjustable mirror holders, four water-cooled diaphragms, four water-cooled branch beam shutters(BBS) and a beamline interlock system. As the undulator radiation has small divergence, the light beam is led alternatively into two branch beamlines, BL-19A and BL-19B, by the operation of inserting an appropriate mirror for each branch beamline. Two different modes of operation, mode-A and mode-B, are illustrated in Fig. 5(a) and Fig. 5(b), respectively. Since the first mirror has to withstand high power radiation from the undulator, we have selected SiC as a mirror material.

When the mirror system is in the mode-A, the light beam is led to BL-19A, and into constant deviation angle grazing incidence monochromator (CDM). This monochromator is a revised version of the CDM at BL-11D of the Photon Factory.[4] It has two constant deviation angles, 160 and 170, to cover wide range of output photon energy, from 12.5 to 250 eV. At BL-19A a photoelectron spectrometer with a spin- and angle-resolved electron energy analyzer will be installed early in 1989.

In the mode-B, the undulator radiation is reflected by a SiC mirror and led to BL-19B, and into the plane grating monochromator (PGM). The monochromator has no entrance slit and covers the photon energy range from 10 to 1100 eV by using four plane gratings. Of the four plane gratings, two are varied-space plane gratings recently developed by Harada et al.[5] This branch beamline is dedicated to photoelectron spectroscopic studies of solids on phase transitions at various temperatures.

A. Kakizaki

1. G. Isoyama et al.; Technical Report of ISSP No. 2031 (1989).
2. A. Kakizaki et al.; Technical Report of ISSP No. 2025 (1989).
3. S. Sato et al.; Nucl. Instr. and Meth. 208 (1983) 31.
4. T. Miyahara et al.; Japan. J. Appl. Phys. 24 (1985) 293.
5. T. Harada et al.; SPIE Proceedings, Vol. 503 (1984) 114.

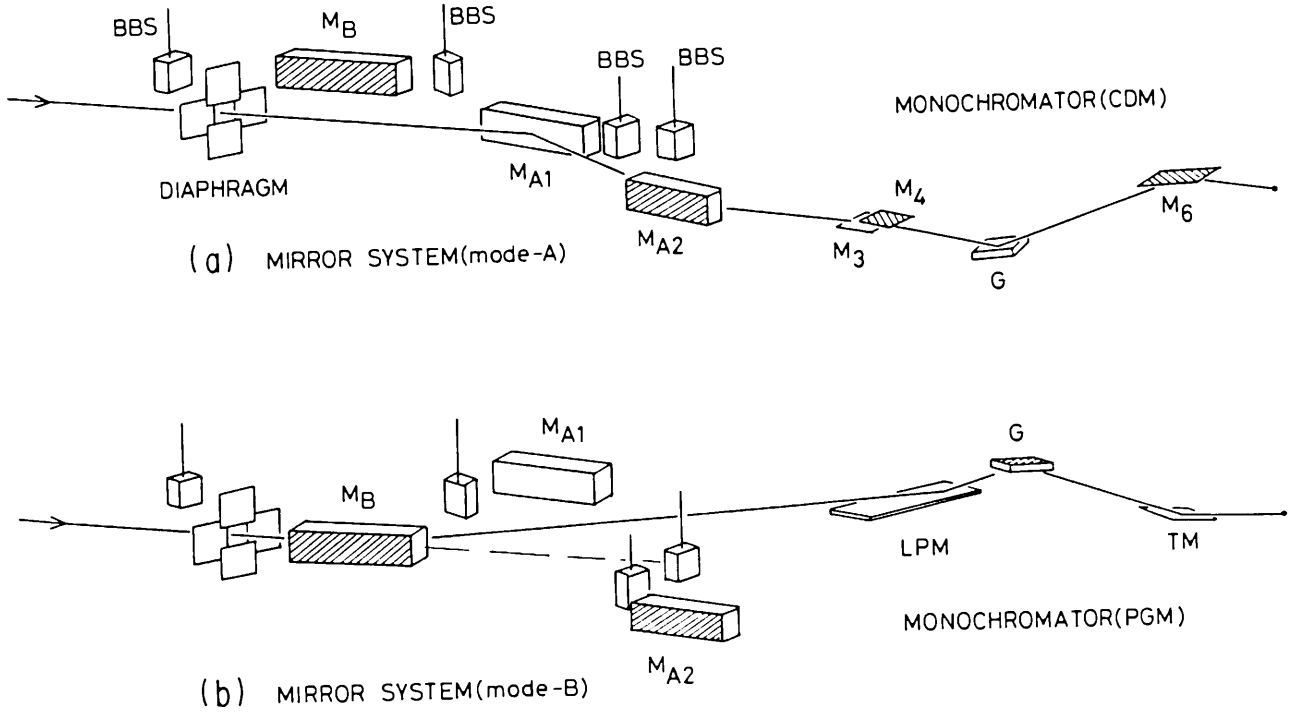

Fig. 5 Optical arrangement of the beamline BL-19A and BL-19B. (a) : mode A and (b) : mode B.

3. BL-13, An MPW/U Beamline of National Institutes of STA and MITI.

The design principle and outline of the BL-13 has been already given in the preceding volume.

Construction of this beamline was continued during FY 1988. A multipole wiggler/undulator was installed in the straight section of the ring located between the bending magnets B12 and B13 and a front-end of the beamline was set in position. Along with the construction work inside the shielding wall , a beam transport section, an ultra-high vacuum chamber which will accommodate a VUV mirror, a double crystal monochromator combined with a focussing mirror, a branch beamline monochromator were installed in the experimental hall.

At the branch beamline BL-13A, a vertical axis goniometer for X-ray precision measurement of the lattice parameter of crystals will be installed. The goniometer consists of a precision spindle rotated by a sine arm and an angle interferometer for the measurement of the angle of the spindle axis. The sine arm is driven by a stepping motor with an angle increment as small as 0.02" per pulse over a range of +15". Piezoelectric ceramic is used to control 0.001" level angle in +10" range. The designed angle interferometer will have a range of +15" with one fringe corresponding to 0.4" and the resolution being 0.001".

At BL-13B, a combined apparatus for X-ray photoelectron spectroscopy (XPS) and X-ray absorption spectroscopy (XAS) will be installed. A schematic diagram of the apparatus is shown in Fig. 6. It consists of two ultra-high vacuum (below 5×10^{-8} Pa) chambers and a multi-sample introduction port. Measurements of XPS and Auger electron yield XAS were performed by using a RIGAKU XPS-7000 electron analyzer system including a four-element cylindrical electrostatic lens. The 180°-hemi-spherical electrostatic analyzer and lens system guarantees high resolution analysis up to 5 keV. To clarify the performance of the apparatus, preliminary experiments were carried out on BL-11B. High resolution XPS spectra were obtained with a high signal-to-background ratio over a wide electron energy range up to 2.6 keV. XAS spectra were obtained in the two modes, total electron yield and Auger electron yield.

On the high pressure apparatus to be installed in BL-13B a description is given in a separate section of this issue (see MAX-90).

H. Iwasaki

4. AR-NE1, A Circular Polarization MPW/U Beamline of Tristan Accumulation Ring (AR)

4a. The beamline

The beamline for the circularly polarized synchrotron radiation at the 6-GeV Accumulation Ring for TRISTAN project is now under

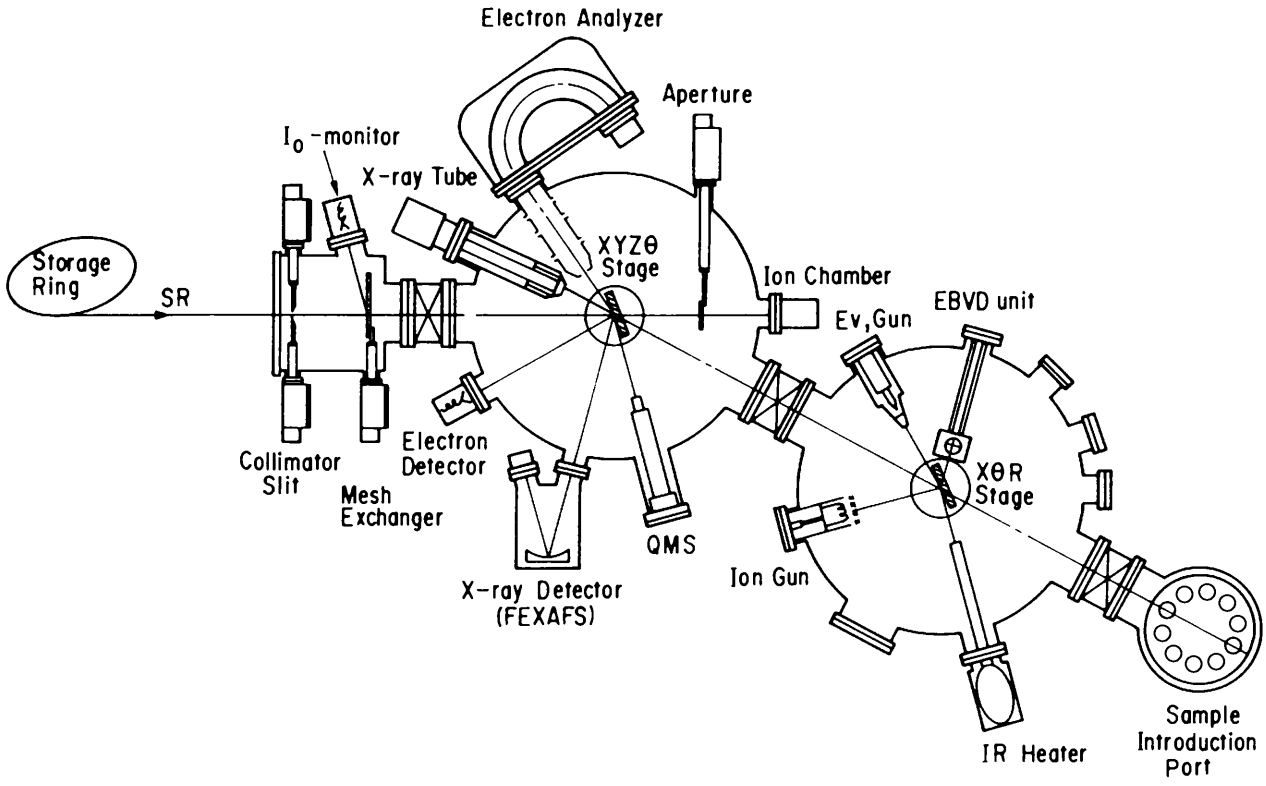

Fig. 6. A combined apparatus for the XPS and XAS to be installed at the branch beamline BL-13C.

construction. It was designed to produce the circularly polarized X-rays at the photon energy range of 200 eV ~ 100 keV. The details of the mechanism and the spectra of the brilliance and the degree of circular polarization are described in chapter of Light Source Department.

The radiation produced by the above insertion device is used by the following three branch beamlines;

1) BL-NE1A1 for high resolution normal Compton scattering and magnetic Compton scattering experiments. Its design values are as follows: The energy range of the monochromatized X-rays is E = 50 ~ 70 keV and the energy spread is $\Delta E/E \leq 10^{-3}$. The beam size at the sample position is S ≈ 1 mm^2 and flux is I > 10^{13} photons/s. The overall resolution in momentum space is $\Delta P \leq 0.1$ atomic unit. These figures are accomplished by a quasi-doubly-bent (Q-D-B) crystal monochromator.

2) BL-NE1A2 for multi-porpose experiments such as magnetic Bragg scattering and magnetic absorption spectroscopy. The energy range of the monochromatized X-rays 6 ~ 100 keV is provided by a newly designed fixed-exit-beam double crystal monochromator.

3) BL-NE1U for monochromatic complete circularly polarized soft X-rays (CPSX) works in the energy range of 200 eV ~ 1.5 keV which is made available by a grating monochromator.

For the MPW mode, the total power of SR is about 4 kW when the acceleration energy is 6 GeV and the stored current is 50 mA. To protect beamline elements from such a high power radiation, most of them have to be cooled by water. Figure 7 shows the top view and side view of the beamlines. At the front end, there are a water cooled mask I, a water cooled absorber, a beam position monitor for the undulator mode, a beam shutter made of stainless steel and a lead shield to avoid the bremsstrahlung from the long straight section.

CPSX is extracted by a plane VUV mirror I after a lead shield. Its angle of incidence is 1.5°. The reflected CPSX is reflected again by a VUV mirror II, which is a bent cylindrical mirror with variable radius of curvature to compensate the undesired additional bending of the mirror I caused by heat due to irradiation. The VUV monochromator, which is under design, is of a vertical dispersion type with two interchangeable gratings.

At the X-ray beamline, the heat absorber consisting of 4 foils of graphite whose thickness is 0.1 mm each, protects two 0.3 mm thick beryllium windows from 4 kW heat load. The height of beryllium windows can be adjusted remotely within an accuracy of 0.1 mm to extract SR completely even when a beam position changes. The Q-D-B crystal monochromator for Compton scattering experiment was designed so as to focus the monochromatized X-ray beam both vertically and horizontally. As shown in Fig. 7, this monochromatized X-ray beam is diffracted upward and led to the hutch for Compton

scattering experiment.

When the multi-purpose beamline is used, the Q-D-B crystal monochromator is shifted downward and white X-rays are led to BBS. A double crystal monochromator, a down stream shutter (DSS), a 2-dimensional X-ray slit and an experimental hutch have been installed so far. In the near future, two parabolic X-ray mirrors I and II will be installed at the location shown in Fig. 8.

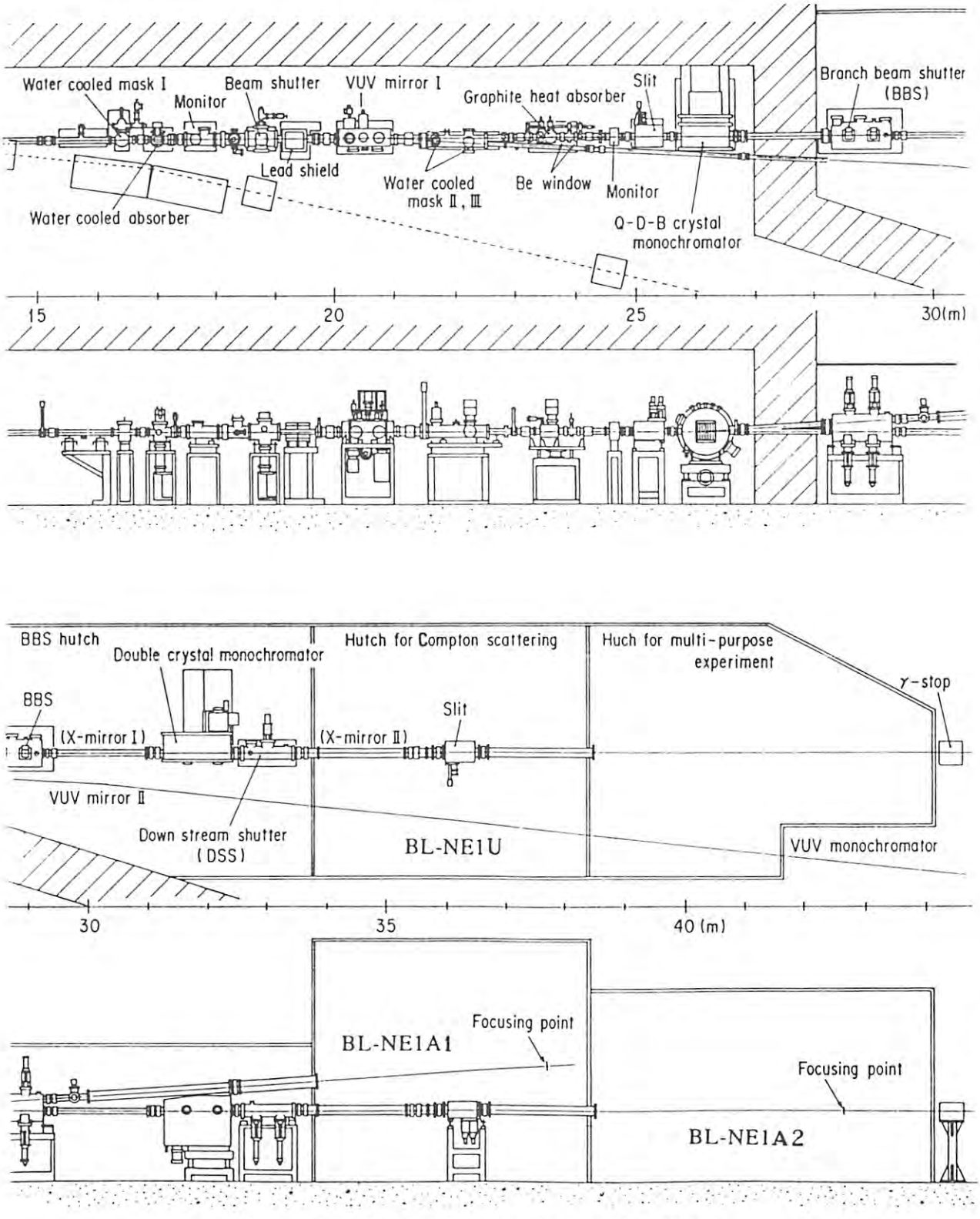

Fig. 7. Top and side view of the beamline AR-NE1.

4b. The monochromators

1) Q-D-B crystal monochromator

For the high resolution Compton scattering experiment, it is necessary to obtain a flux as high as 10^{13} photons/s and an energy resolution $\Delta E/E$ of better than 10^{-3} at the energy of 60 keV, though it is not necessary to have an extremely collimated monochromatic beam.

To obtain such high flux, a doubly-bent crystal monochromator as shown in Fig. 8(a) is expected to be suitable. The bending radii R_1 and R_2 are calculated from the geometry: In case of Si 111 diffraction and 60 keV monochromatized X-rays, R_1 = 596 m and R_2 = 508 mm. Furthermore, the crystal must be cooled by water in order to withstand 4 kW heat load. Since it is difficult to apply water cooling to a doubly-bent monolithic crystal, the Q-D-B crystal monochromator has been devised. The monochromator comprises an array of singly-bent crystals as schematically shown in Fig. 8(b). Each piece of the monochromator crystal mounted on a holder has thermal contact with liquid Ga-In alloy, and each of the holders is water-cooled while its orientations (ω_n, ϕ_n) can be adjusted independently.

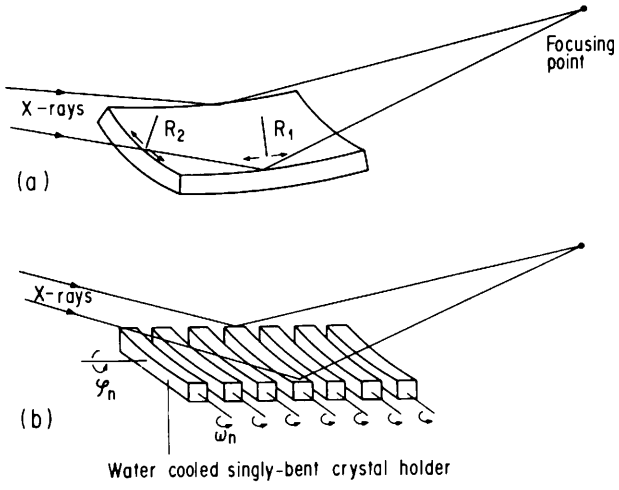

Fig. 8. The Q-D-B crystal monochromator at AR-NE1A1, (a): schematic figure of the doubly-bent crystal monochromator and (b): design concept of the Q-D-B crystal monochromator.

2) Double crystal monochromator

At the Photon Factory, double crystal monochromators using a mechanical linkage of a cam system have been developed and proved suitable for the Bragg angle range of 3° ~ 70°.

On the other hand, in order to cover the energy of 6 ~ 100 keV, it is necessary to design another system suitable for the Bragg angle of 1 ~ 20°. Figure 9(a) schematically shows a typical arrangement of the fixed-exit-beam monochromator. Supposing O be the pivot, the positions of the first and second crystal, OA and OB, are varied while the Bragg angle θ is changed with the following relations,

$$OA = \frac{h}{2}\frac{1}{\sin\theta}, \quad OB = \frac{h}{2}\frac{1}{\cos\theta},$$

where h is the height difference between white and monochromatized beams. The rapid change of OA at the relatively small Bragg angle region causes a difficulty of the mechanical linkage. If replaced by a monolithic large single piece of crystal, this difficulty is overcome. A large piece of a single crystal which is perfect enough for the present purpose is commercially available. Figure 9(b) shows the side view of the new type of double crystal monochromator. The first crystal of 820 mm long is mounted and directly water-cooled. The second crystal is translated in a direction of the surface normal by a mechanical linkage in such a way that the above relation is kept. The second crystal holder has a bending system for sagittal focusing, if necessary.

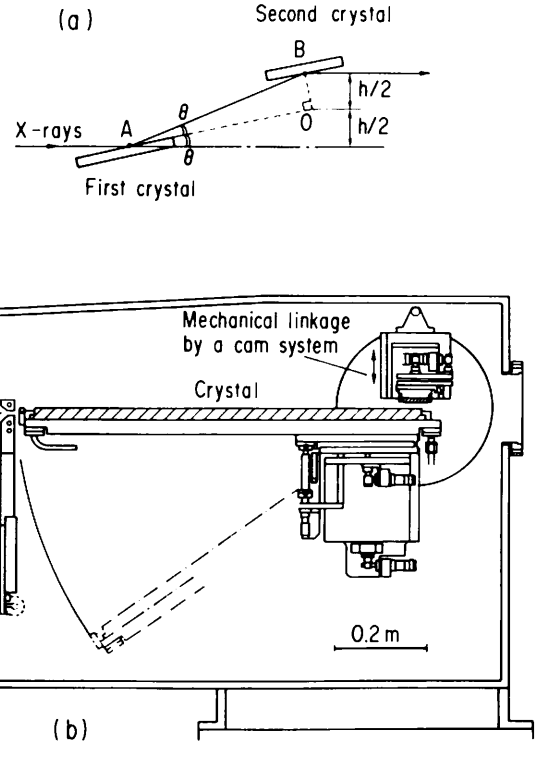

Fig. 9. The double crystal monochromator at AR-NE1A2, (a): schematic figure of the fixed exit beam monochromator and (b): side view of the monochromator.

3) Grating monochromator

The optical elements of the grating monochromator are composed of two prefocusing mirrors, an entrance slit, one or two interchangeable gratings, and an exit slit of Codling type. The entrance slit, the exit slit, and the grating are mounted on a Rowland circle with a diameter of 10.3 m which is equal to the radius of curvature of the grating. To keep polarization characteristics of the incident CPSX, the incident angle to the grating is chosen to be 89°. Two prefocusing mirrors are spherical concave to reduce the aberration and to obtain a sharp image on the entrance slit. The scanning of the monochromator is realized by a linear motion of the prefocusing mirrors, the entrance slit and by a rotation of the grating around the entrance slit. The photon energy covered by the monochromator ranges from 240 eV to 1.5 keV. The groove densities of the gratings are 1200 lines/mm and 2400 lines/mm.

H. Kawata

5. BL-28, A Circular Polarization MPW/U Beamline of PF.

The purpose of BL-28 is to utilize circularly polarized light (CPL) produced through a helical undulator placed at a straight section of the PF ring. Since the beamline NE1 of the Accumulation Ring (AR) which was also designed to provide CPL covers photon energies higher than 250 eV, BL-28 has been designed to cover photon energies lower than 300 eV with some overlap.

Among the experimental programs expected to be carried out at BL-28 are the absorption or the total yield measurements on some rare earth ferromagnets, spin-resolved photoemission spectroscopy on 3d metals and alloys and research studies to find a method of characterizing the CPL at photon energies higher than several tens eV.

The lowest photon energies available at the moment is assumed to be 12 eV corresponding to the parameters of the undulator, K_x = 3 and K_y = 7.5. However, in the future the lowest energy will be extended down to 5 eV, provided the heat problem of the first pre-focusing mirror is overcome to allow higher magnetic field of the undulator. The maximum heat load on the mirror, which is a toroidal mirror made

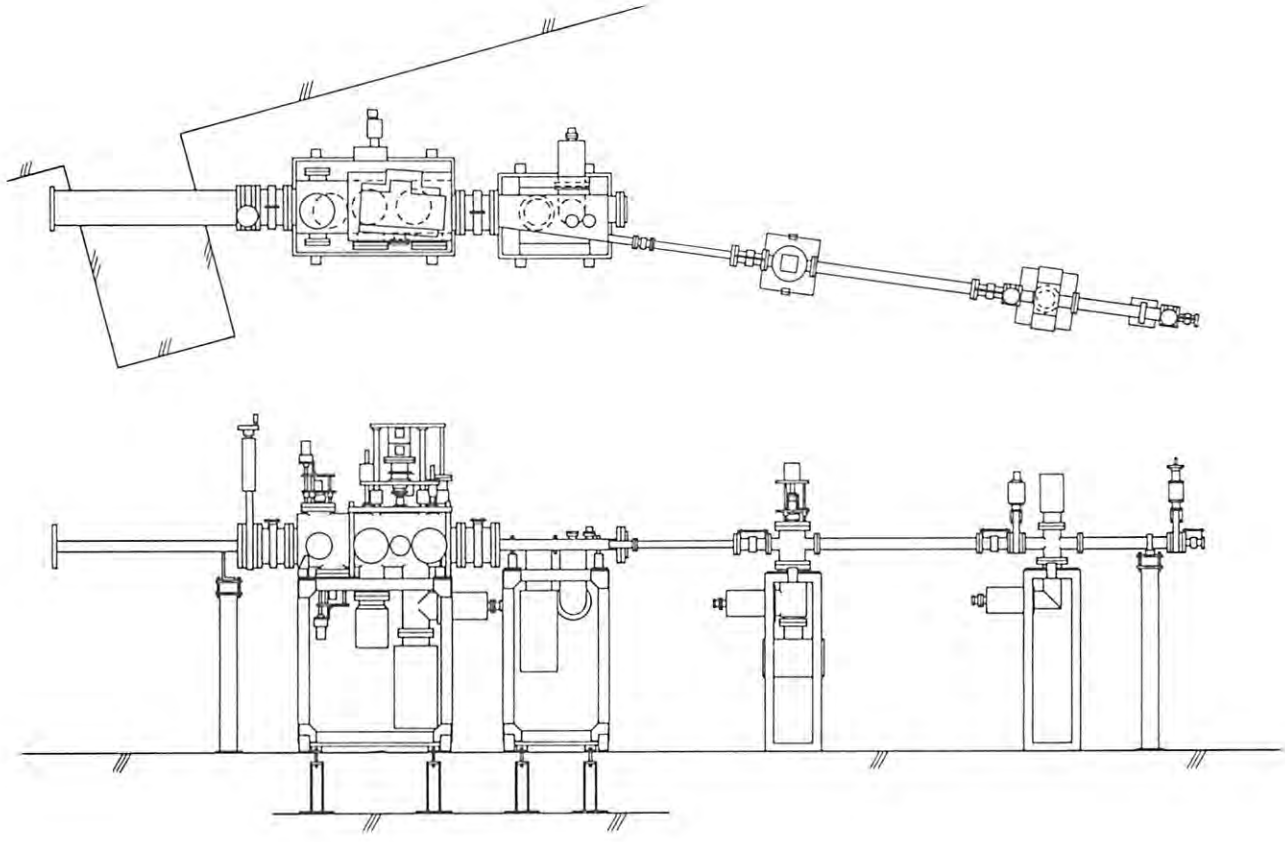

Fig. 10. Top and side view of the beamline BL-28.

of SiC with the radii of curvature R = 250 m and ρ = 680 mm, is estimated to be roughly equal to 500 W for the above K-parameters. The above heat load is partly blocked by two water-cooled slit blades by which the angular divergence of the radiation is limited vertically.

The CPL after being reflected by the pre-focusing mirror is introduced to a grating monochromator of a constant deviation type. The monochromator has five gratings with different parameters. Two gratings (R = 4 m, 600 l/mm, 1200 l/mm) cover the photon energy range from 80 to 300 eV with the deviation angle of 170°, other two gratings (R = 2 m, 600 l/mm, 1200 l/mm) cover the photon energy range from 20 to 80 eV with the deviation angle of 160°, and another grating (R = 500 mm, 600 l/mm) covers photon energies below 20 eV with the deviation angle of 8.85°.

A refocusing mirror system and an apparatus for photoemission spectroscopy are also under construction.

T. Miyahara

6. BL-3, A New Purpose-oriented Beamline

A study of designing BL 3 has been started in the spring of 1988. As schematically shown in Fig. 11, this beamline consists of three branch beamlines; BL-3A, BL-3B, and BL-3C. Synchrotron radiation from the bending magnet B2 is supplied for BL-3A and radiation from the bending magnet B3 is supplied for BL-3B and BL-3C. Optical components of BL-3A and BL-3B were commissioned until the autumn of 1988. Two photon-beam position monitors are installed in BL-3C. These monitors are used in a feedback system to reduce the drift of the electron beam position in the storage ring.

BL-3A is designed for X-ray experiments on diffraction, scattering, and absorption. The optics includes (1) a beam position monitor, located at 14.6 m from the source, (2) a collimating mirror at 16 m, (3) a double-crystal monochromator at 20 m, and (4) a refocusing mirror at 23 m. The first flat mirror can be bent in parabolic quadric to reduce the vertical angular divergence and increase the energy resolution. The monochromator is of a sagittally focusing type where a triangular second-crystal is used to focus the photons within a 4 mrad horizontal acceptance. The utgoing beam of the monochromator has a fixed beam-height. The second mirror has the similar structure as the first one and is used to make a focal point at 28 m from the source. Each optical component such as the monochromator, mirrors, and beamline pipes can be moved vertically and remotely when the glancing angle is changed.

The optics of this beamline has the following advantages: (1) it is one of the X-ray experimental stations to have the highest photon flux in bending-magnet beamlines; (2) the very small beam-size of about 100 μm can be achieved at the sample position without any X-ray slits; (3) the critical energy of in-coming beams is changeable within the range of 5-25 keV.

BL-3B will provide us monochromatized radiation in the energy range of 10-300 eV. The heart of the beamline is a constant deviation monochromator with a movable exit slit. A prefocusing toroidal mirror makes a 1:1 image of the source on the entrance slit of the monochromator. Refocussing cylindrical and spherical mirrors demagnify an image on the exit slit to the size of about 1 mm × 1 mm at the sample position. When a spherical laminar grating with the radius of 23 m and groove density of 1800 l/mm is used, the energy resolution is 4000 at 100 eV and 1100 at 300 eV

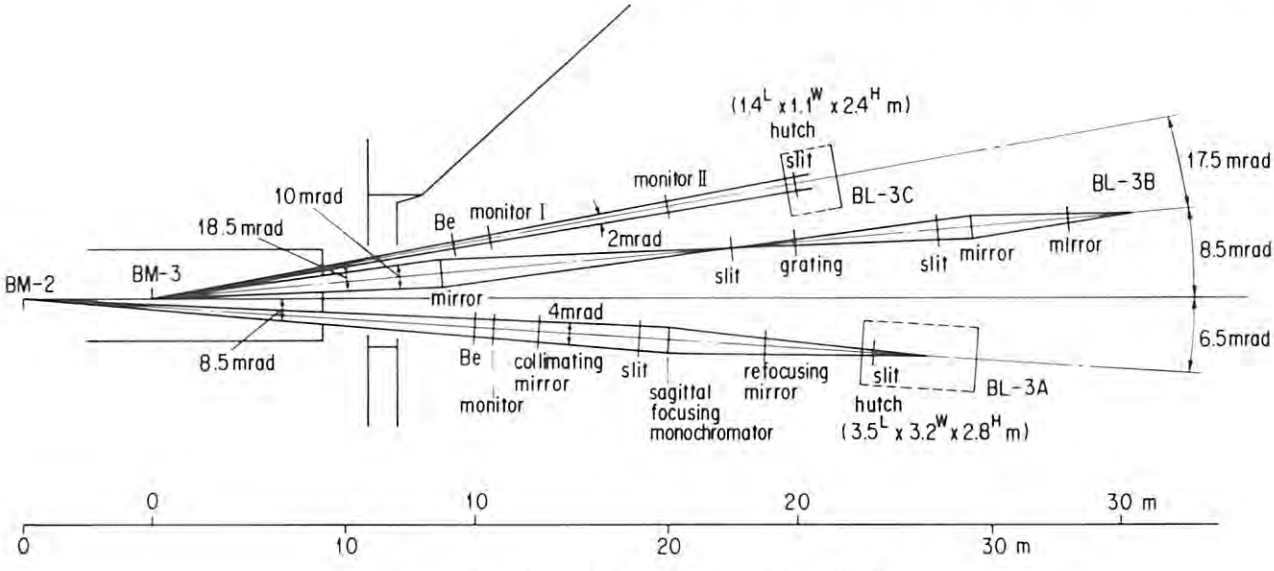

Fig. 11. Layout of the beamline BL-3.

under the condition of 100 μm - 100 μm slit widths. The maximum photon flux of about 10^{12} photon/sec can be expected with these slit widths.

Angle resolved photoelectron spectroscopy of gas and solid sample and coincidence measurements of Auger electrons and fragment photoions for free molecules are planned at this branch beamline.

BL-3C is mainly used for the beam position monitoring to stabilize the electron orbit of the storage ring. Two beam-position monitors are installed at 10.6 and 16.2 m from the source in order to detect the vertical displacement and inclination of the beam and operate the feedback system. This branch has also a hutch for white X-ray experiments at the distance of 20.7 m from the source. A double-crystal monochromator will be installed at 18 m on this branch in the near future.

A. Yagishita & S. Sasaki

7. BL-12C, A New Multi-layer Reflector Branch.

This branch beam line has been specially designed and constructed for the study of photochemical processing, involving photo chemicaletching and photochemical vapor deposition of semiconductor materials. Such study requires a high flux photon beam, but not high resolution. The optical system of this beamline consists of only two optical elements, a prefocusing mirror and a multilayer wavelength-selective reflector and is shown in Figs. 12 and 13 schematically. A Pt-coated SiC toroidal mirror, which is placed 18.3 m downstream of the source point, accepts 5 mrad horizontal and 1 mrad vertical divergence of SR, reflects into 3.8° upward and focuses it on the exit arm of the monochromator which placed 32.3 m downstream of the source point.

Multilayer reflectors, such as 27 layers of Mo-Si and 21 layers of Rh-Si, which were designed and fabricated by Yamamoto et al. of Tohoku University so as to obtain high reflectance around 100 eV of photon energy, is installed in the monochromator, steers SR beam downward and selects photon energy by changing an incident angle θ. With this arrangement, a quasi-monochromatic and bright light is obtained in the energy range 80 - 100 eV (θ : 38 - 48°). Two stage differential pumping system is provided in the exit arm of the monochromator so as to introduce the sample gases into the chamber up to 1 Torr.

In order to estimate the performance of this beamline, photoelectron spectra of Ne gas have been obtained using a Ph-Si multilayer reflector. From the spectra, the energy resolution $E/\Delta E$ and output flux of this beamline are estimated tobe ≈12 and ≈10^{15}

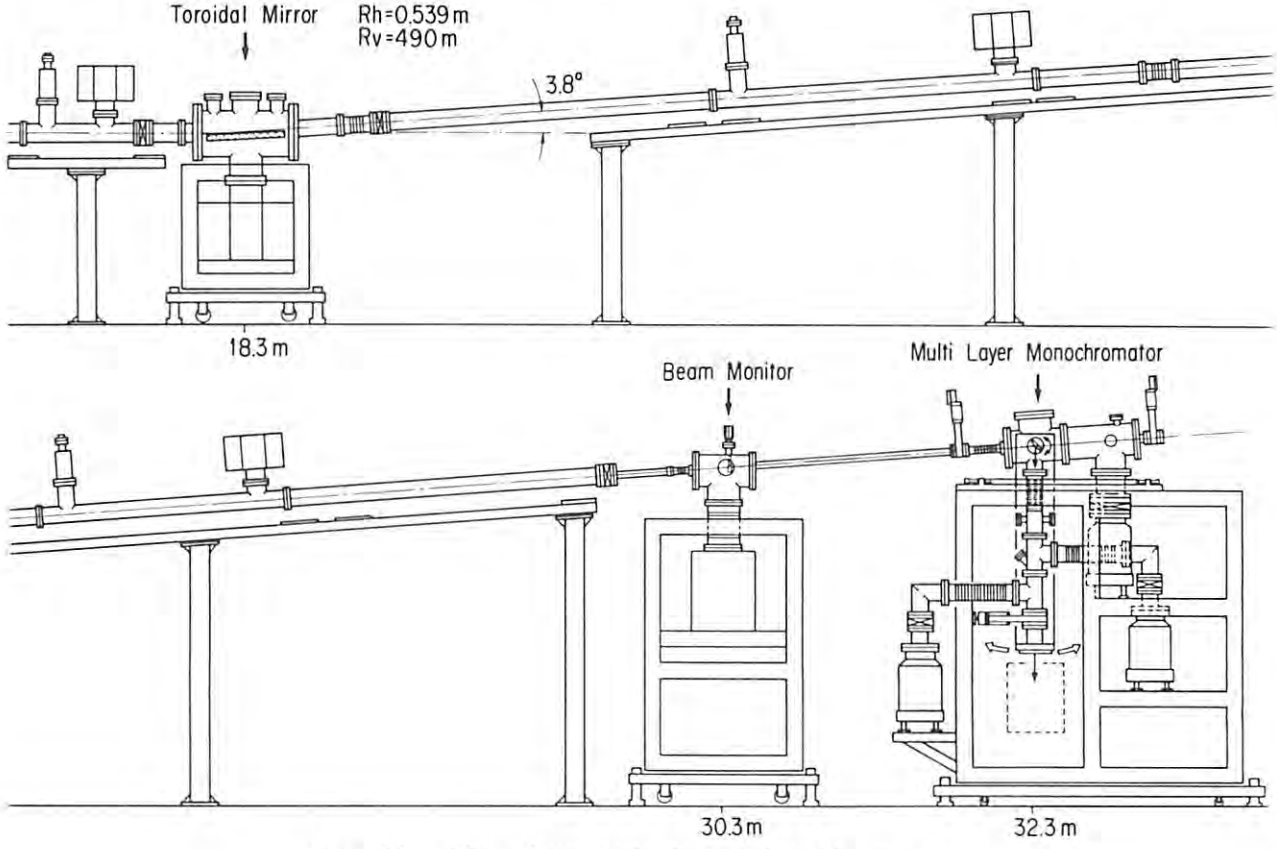

Fig. 12. Side view of the branch beamline BL-12C.

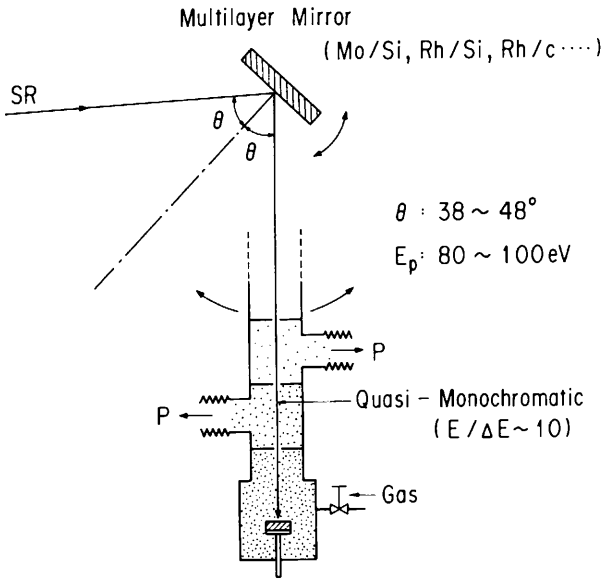

Fig. 13. Schematic diagram of the multilayer reflector monochromator together with the irradiation chamber.

photons/s at 95 eV with 200 mA ring current. Various kinds of experiment on photochemical processing and radiation biology are in progress at this beamline.

K. Tanaka

8. BL-18, A Purpose-oriented Beamline of ISSP.

This beamline is designed for experiments using VUV and soft X-ray. The beamline consists of three branch beamlines, BL-18A, BL-18B and BL-18C. The front end accepts 25 mrad horizontal divergence of the bending magnet B-18 radiation. In FY 1988, the construction of the front end and the branch beamline BL-18A was completed under collaboration between Synchrotron Radiation Laboratory of the Institute for Solid State Physics, the University of Tokyo, and the Photon Factory. The mirror system of BL-18A accepts 5 mrad horizontal divergence of the radiation and leads to a grazing incidence monochromator. The monochromator covers the photon energy range from 15 to 300 eV and is dedicated to the photoelectron spectroscopic studies of solid surfaces and interfaces.

A. Kakizaki

9. AR-NE3, An Undulator Beamline of TRISTAN AR

Technology of insertion devices has remarkably been advanced. Particularly quite recently a technique of installing magnet pieces into high vacuum has become feasible. Thus the feature has almost brought us to a decision to install a new beam line NE3 for an X-ray undulator. In order to meet this requirement the following conditions should be fulfilled: the magnetic periodicity λ_μ = 2.8 cm, magnetic field strength β = 0.4 T and electron acceleration energy E : 8 GeV. In other words the first harmonics can reach 14.4 keV which is not only suitable for production of Mössbauer source but also for other applications to solid state physics such as surface interface studies which needs highly brilliant X-ray sources.

Since the beam divergence of X-ray undulator radiation is expressed by K/γ, the apparent beam size at around 40 m will be only 0.2 mm V × 1 mm H. Current design of BL-NE3 shows us that two tandem X-ray hutches accept monochromatic X-rays mostly focussing on 10-20 keV, while in case of necessity of eliminating higher harmonics mirror optics will be in use. Each element of the beamline can be small due to the beam divergence and associated beam size.

The excepted brilliance under the current of 50 mA and the horizontal emittance of 130 nmrad with coupling of 1 % will be around 10^{15} photons/sec/mrad^2/mm^2/0.1 % b.w. Analysis of local heat load onto a first optical piece ranging the order of 40 watts/0.2 mm^2 and design of protection against γ-ray radiation hazard from the straight section for the insertion device are underway.

M. Ando

C. IMPROVEMENTS OF BEAMLINES AND STATIONS

1. BL-1A and 1C, The NTT Stations

Some modifications were made on the BL-1 in 1987/88.

At the BL-1A which is the Solid surface analysis beamline, two mirror chambers were installed for adjusting the positions or angles of paraboloidal mirrors for collimation and focusing in 5 axes. In these chambers, mirror bending mechanism was also added in order to finely adjust the longitudinal curvature of the paraboloidal mirrors for higher energy resolution.

A molecular beam epitaxy (MBE) chamber with which semiconductor films such as GaAs can be grown in UHV being monitored by RHEED were attached in vacuum to the Multi-technique surface analysis system. In order to operate this system safely, a special arsenic processing system, which consists of a liquid nitrogen trap with two polyimide valves, a quadrupole mass filter and a turbomolecular pump, was attached to the roughing pump system. During baking the MBE chamber, no $^{75}As^+$ mass

signal was detected, indicating the effectiveness of this processing system.

A plane grating monochromator was set around the center of the BL-1C which is the photochemical reaction beamline, as shown in Fig. 14. The wavelength of the output beam was selected by a combination of rotation of the first plane mirror or plane grating. This monochromator can be operated in three modes. White beam mode and low resolution mode obtained by combination of two plane mirrors are useful for the study of the wavelength dependence of the photochemical reaction. High resolution mode is obtained by selecting a combination of the plane mirror and the plane grating. The output beam spectrum was analyzed by a 1m grazing incidence concave grating monochromator (Minuteman Inc. model 310GSPM). A monochromatized beam with about 1 % resolution was obtained down to about 50 Å without any influence of the zeroth order tail. Adjustments of this monochromator are continued also in 1989.

M. Oshima

2. BL-9A and 9B, The NEC Stations

An atmospheric environmental exposure system for synchrotron radiation has been developed at BL-9A. It is most essential that the SR extraction mechanism for an atmospheric environmental exposure be investigated. The SR extracting chamber, equipped with a Be window and an extraction window, is filled with helium at atmospheric pressure. The Be window, vacuum-sealed by a Viton O-ring, was preliminarily employed giving a 25 mm square exposure area.

A new VUV beamline, BL-9B, has been constructed for the study of SR induced photochemical reaction, under the collaboration between NEC Corporation and the Photon Factory. This beamline has been designed to utilize photons ranging below 300 eV, and to allow using gases in the reaction chamber without any window between the chamber and the beamline.

The radiation emitted from the bending magnet B9 is reflected and focused into the monochromator by a combination of a SiC plane and a Pt/SiO_2 toroidal mirrors, with the acceptance angle of 10 mrad. The photons monochromatized by a grazing angle plane grating monochromator are refocused and introduced to the reaction chamber. White light is also available by changing the grating with the mirror in vacuo.

For the purpose of windowless experiments using gases, a differential pumping system and a vacuum protection system are carefully designed. The differential pumping system can maintain the pressure in the monochromator around 10^{-9} Torr, even when gas is flowing. Additionally, BL-9B has a vacuum protection system for the storage ring against accidental vacuum breakdown of the reaction chamber or the beamline. This system, essentially the same as in BL-9A, consists of the acoustic delay line (ADL) of 48 ms delay time and the fast closing valve (FCV) of 12 ms closing time. This system was examined and confirmed to have a sufficient performance.

Careful design was also made for the treatment of toxic gases to prevent researchers from hazards and to keep environmental safety; The gas is trapped almost completely with adequate adsorbents and the concentration of treated gas are monitored all the time. The gas leakage is also monitored by the sensors placed at several important points. When the sensor detects toxic gas leakage, all the valves in the gas supplier are automatically closed.

K. Okada & I. Nishiyama

Fig. 14. The plane grating monochromator at BL-1C.

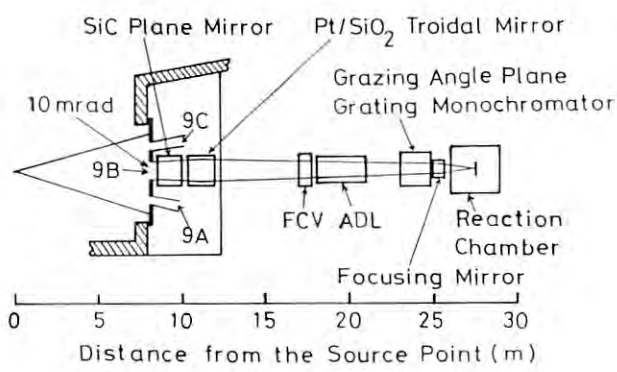

Fig. 15. Layout of the branch beamline BL-9B.

3. BL-11B, A Soft X-Ray Station

In this branch beamline a soft X-ray double crystal monochromator[1] has been used. The first crystal of InSb melted during the run of July 1987 due to a misfocusing of beam[2]. A water cooling system for the first crystal and a computer program to fix a vertical beam position have been developed.

A perspective view of the newly-installed first crystal driving and cooling assembly is shown in Fig. 16. Rotational motion of a goniometer (1) is transferred to the crystal through bending of a bellows (3). In order not to apply any torsion to the rotating mechanism, water pipes are inserted in an arm 1(2-1) and connected to a seamless pipe (5) at the connector (4). At this connector (4), water pipes are welded to ICF-34 flange but water does not touch the welding part. The seamless pipe (5) is formed along an arm 2 (2-2) and is silver-soldered onto a crystal base plate made of copper (6). A 1 mm-thick InSb crystal is mounted on the base plate and a 0.1 mm-thick indium sheet is inserted between the crystal and the base plates in order to improve thermal contact. The crystal and the arm 2 (2-2) can be disconnected from the connector (4) to exchange the crystal. The connecting part is evacuated to a low vacuum which is monitored by a pirani gauge to detect a water leakage.

Figure 17 illustrates how to fix the vertical beam position with the change of photon energy in the computer program. The dashed and solid lines denote the beam paths in the presence and absence of heating effect of the first crystal, respectively, for the same photon energy. When letting θ_0 be the ideal incident angle to the second crystal, and θ_1 and θ_2 be the real angles of the first and second crystals to the parallel horizontal solid lines, then,

$$\theta_1 = \theta_0 - \beta \text{ and } \theta_2 = \theta_0 - 2\beta.$$

Using the Bragg's low,

$$2d \sin\theta_0 = 2d(1 + \alpha\Delta T)\sin\theta_1,$$

then,

$$\beta = \frac{\alpha\Delta T}{1 + \alpha\Delta T} \tan\theta_0,$$

where α is a coefficient of linear thermal expansion of the monochromatizing crystal (α = 0.49×10^{-5}/°C for InSb). ΔT is the temperature difference between the first and second crystals.

In order to fix the vertical beam position, the first crystal should be translated to the horizontal position T_x from the second crystal;

$$T_x = \frac{L \tan 2\beta}{\tan(\theta_0 - 2\beta)} - \frac{H + L \tan 2\beta}{\tan(2\theta_0 - 2\beta)}$$

where H is the vertical distance between the first and second crystals and L is the horizontal distance from the second crystal to the sample position.

β is determined from estimated value of ΔT. Although the change of ΔT caused by decay of stored current is not taken into account, it turned out negligibly small in the present system, when ΔT is below 50 °C. Now continuous and fully automatic measurements can be performed without any care of beam height movement or energy calibration shift.

Y. Kitajima

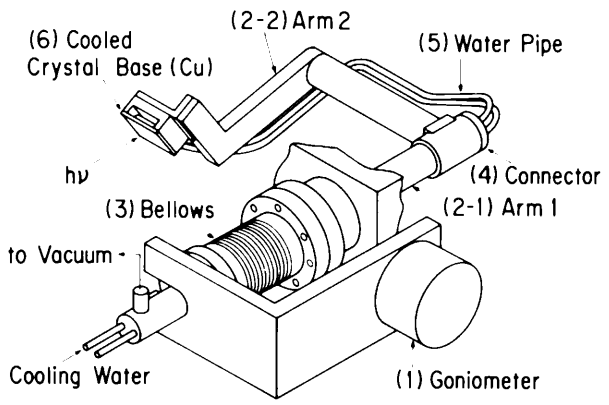

Fig. 16. Perspective view of the first crystal driving and cooling assembly of the JUMBO Jr. monochromator at the branch beamline BL-11B.

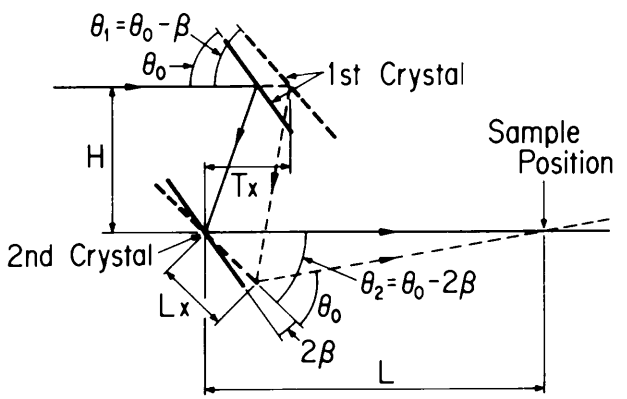

Fig. 17. Schematic figure of aligning principle of the BL-11B double crystal monochromator.

1. T. Ohta, P. M. Stefan, M. Nomura and H. Sekiya; Nucl. Instrum. Methods, A246, 373 (1986).
2. Photon Factory Activity Report 1987 p. 84 (1988).

4. BL-17A, A Fujitsu Station

A schematic drawing of BL-17A is shown in Fig. 18. This branch line consists of four main components; a thin Be-foil(10 mm thickness), a double crystal monochromator, a down stream shutter, and a mirror. The Be is held by water-cooled copper-plates and set between a branch beam shutter (BBS) and the monochromator. A pressure in the BBS chamber is 10^{-9} Torr, while that in the monochromator is 10^{-7} Torr. The first and second crystals of the monochromator can be rotated by 75°. The second crystal can be translated along a 313 mm long translation stage. These three motions of the two crystals are synchronously controlled so that the height of the reflected beam is always kept constant by 65 mm above the incident beam. The first crystal holder is water-cooled. Two different crystals can be changed for the first crystal and four different crystals for the second crystal in vacuo. At present, a direct beam is monochromatized by Si(111) crystals in a wavelength range from 0.9 to 3 A in air. The down-stream shutter behind the monochromator is used for keeping a diffraction condition of the first crystal constant even during work in the experimental hutch. We can, therefore, save a time by making a temperature of the first crystal stable at every change of experimental conditions in the hutch. A Pt-coated mirror is installed to reject higher harmonic components of a monochromatized X-ray.

Figure 19 shows an X-ray image on a screen with phosphorus materials through a 3 mm thick Al-plate. The shape of the image represents a spatial distribution of a direct-beam intensity. BL-17A accepts radiation generated by the B16 bending-magnet. Since the horizontal divergence of this line is from 2 mrad to 6 mrad toward BL-16 measured from the straight line between the B16 and B17 bending-magnets, the image includes radiation from a tail part of the magnetic field of the B16.

This branch line was designed and constructed by Fujitsu Laboratories Ltd. in collaboration with the Photon Factory. This line can also be connected to an ultra high vacuum (UHV) chamber, and used for surface EXAFS experiments.

T. Sato

D. NEW EXPERIMENTAL APPARATUSES

1. New Imaging Plate Reader

An imaging plate is an integrating area detector that operates on the basis of laser-stimulated luminescence from a storage phosphor ($BaFBr:Eu^{2+}$) screen. Its usefulness has been demonstrated by many examples reported in the last and present activity reports. We have developed a new readout system for imaging plate which is more optimized for X-ray diffraction and scattering applications. The scanner is made by modifying a conventional drum-type film densitometer. In this new system, following improvements have been made compared with commercially available scanner originally developed for diagnostic application: (a) We can choose the pixel size of 25 μm and 50 μm in addition to 100 μm. (b) The output signal from a photomultiplier tube is digitized by a 12-bit A-D converter. (c) A special mirror assembly is used to raise light collection efficiency for the stimulated fluorescence. (d) Two photomultiplier tubes are used to cover wide dynamic range of 10^5. (e) The image is immediately displayed on a color graphic

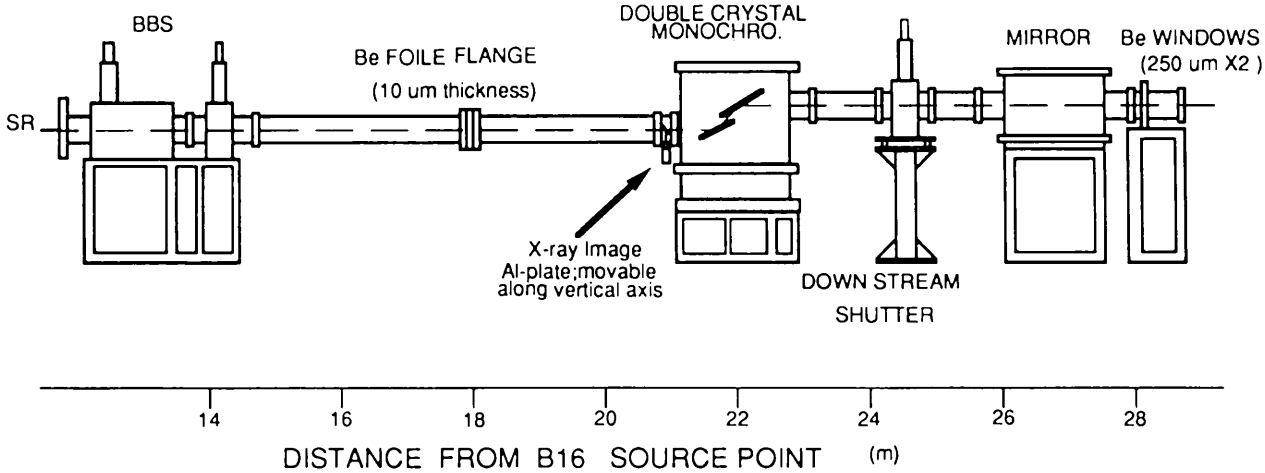

Fig. 18. Schematic drawing of the branch beamline BL-17A.

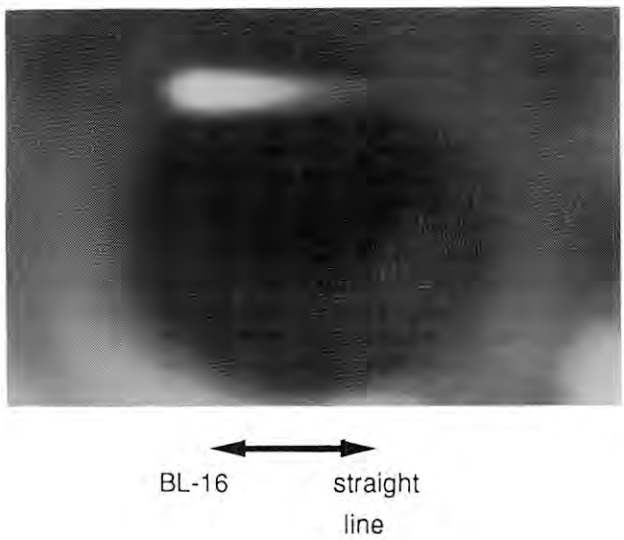

Fig. 19. An X-ray image of the direct photon beam of the BL-17A.

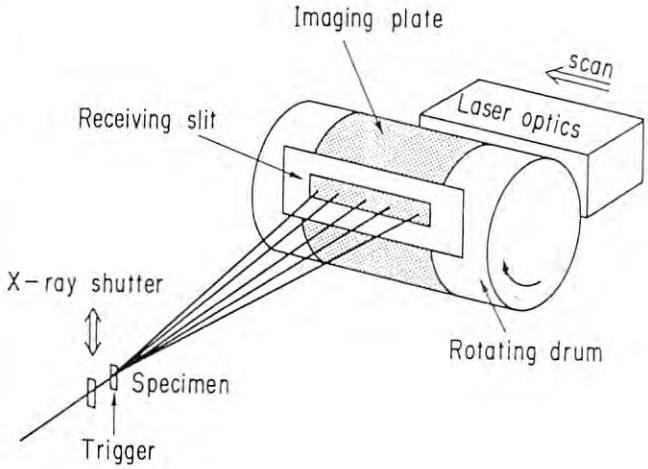

Fig. 20. Schematic drawing of the fast one-dimensional X-ray detector using the imaging plate attached on a rotating drum.

display. This readout system is installed in the room A just next to the experimental floor and is now routinely used by users.

T. Matsushita

2. A Fast One-dimensional X-ray Detector Using An Imaging Plate

A fast one-dimentional X-ray detector has been developed using an imaging plate attached on a rotating drum having a circumference of 1080 mm as shown in Fig. 20. One dimensional X-ray pattern is recorded consecutively in time series on the rotating imaging plate through a horizontal receiving slit. The effective width of the detector is 200 mm and the effective length is 1000 mm along the circumference. A time resolution and the number of time slices are determined by both the rotating speed of the drum and an slit width in the vertical direction. The best time resolution attainable is 23 μs for 2000 time-slice pattern with the drum speed of 20 rps and a slit aperture of 0.5 mm. The drum speed can be adjusted from 20 to 0.01 rps continuously and the slit width from 0.5 mm to several milimeters to meet various experimental requirements. If a multiple exposure is required to obtain better photon statistics, the exitation of the specimen and on-off of an X-ray shutter are synchronized to a timing signal from the rotating drum. The image stored in the imaging plate is read by a laser scanning optics at the opposite side of the receiving slit. Data are displayed on a graphic terminal and finally stored on magnetic tapes.

The detector has been used to record a time dependent small angle diffraction pattern from a contracting muscle and also in a time-resolved dispersive EXAFS experiment.

T. Matsushita

3. He-3 Dilution Refrigerator

The experiment in general science under the extreme conditions is an important clue to establish a new model of an unsolved problem taking out more than a true fact from the complicated phenomena controlled by many factors. Viewing chronicle progress in the low temperature physics, a new field has stepwise opened by development of a new cooling method every time based upon the fundamental discovery in the low temperature physics. The experiment and the theory in the cryogenic physics have spent a long honeymoon time after some turns and twists from 1908, in which Heike Kammerlingh Onnes in the Netherlands succeeded in the first liquefaction of helium named as permanent gas. This has been called as the first year of the low temperature physics by some low temperature physicists.

An application of He-3 dilution refrigerator (hereafter called as He-3 DR) to the diffraction experiment has been used very early to determine the nuclear spin arrangements of solid He-3($T_N \cong 1$ mK), LiH($T_N \cong ?$) and $HoVO_4$($T_N \cong 4.5$ mK). Nobody has ever challenged such an attempt in SR X-ray facilities as to cool down to mK region before our trial.

A He-3 DR with a complete top-loading system, which is able to load and unload the sample in the working duration of the refrigerator, was purchased from Oxford Instrument Inc. in 1988 by financial support of KEK. The virgin test drive of He-3 DR was done for two weeks. The lowest working temperature reached 6.4 mK as its base temperature.

In December, 1988, the second test drive of He-3 DR was made for its proper use from January, 1989. The base temperature reached 22 mK which was 3 times higher than that of the last test run. Many kinds of functions in He-3 DR worked well under an excellent condition. He-3 DR required constantly more rapid circulation of dense He-3 component to gain higher cooling power. For this purpose we supplied the power of heater in still over the regular value. Temperature could not reach the same base temperature as in the last time.

He-3 DR was installed in BL-6C$_1$ hutch, where there was no usual protection against mechanical vibration of the ground and hutch and no shield against electromagnetic waves which cause eddy current heating. The first test operation was made just in the middle of summer vacation and the experimental hall was quiet in everything. This time electromagnetic waves radiated from various kinds of electric machine cause heating up of He-3 DR. Then, He-3 DR shout himself hoarse his hope till he dies.

From January, 1989, we will measure the lattice constants of some materials by energy dispersive X-ray diffraction in mK region, to improve and develop stabilization of the temperature control, adjustment of sample and beam positioning mechanism, etc. After that, we try to confirm a feasible structural phase transition of elpasolite $CsNaHoCl_6$ whose nuclear spins order antiferromagnetically below 1.5 mK. In near future, the study of quantum mechanical effect in solid helium-3 and -4 will be studied by use of modified version of the He-3 DR.

T. Nakajima

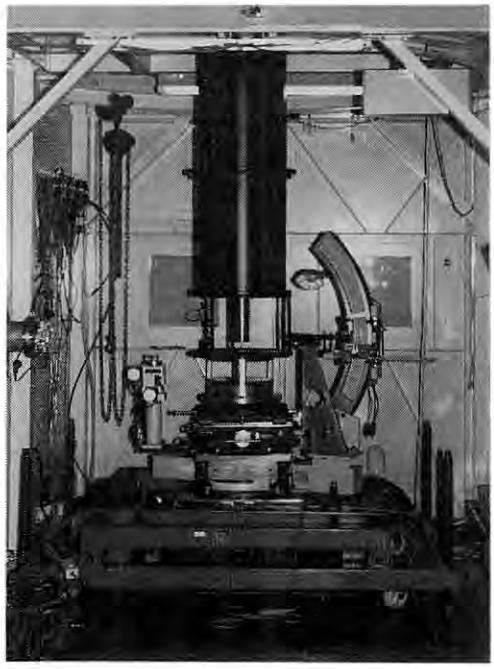

Fig. 21. The He-3 dilution refrigerator is under installation in the branch beamline BL-6C$_1$.

4. A Powder Diffractometer

A newly designed powder diffractometer is commissioned in FY 1988. The aims of the design are as follows.

(1) Easy alignment of the diffractometer to SR beam.

(2) Simple adjustment of the desired wavelength.

(3) Accurate measurement of the diffracted X-ray intensity for Rietveld analysis including anomalous dispersion.

(4) Usage of energy dispersive mode of diffractometry.

The diffractometer is composed of vertical type goniometer, monochromator, monitor and special slit system for alignment. Besides the main part of the system, a high speed specimen spinner, counter monochromator of graphite crystal and heating furnace are also available.

The range of the 2-θ axis is from 40° to 150° and that of θ is 40° to 190° and both angles are measured and controlled by rotary encorders attached directly to their axes. The minimum scale of the encorders is 5×10^{-4}.

For easy wavelength adjustment, a fixed exit beam monochromator is installed into the diffractometer. The range of wavelength obtained is from 0.26 to 4.0 Å for silicon 111 and 333 reflections. The monochromator angle and position are controlled by the rotary encorder and linear encorder with minimum scale of 0.001° and 0.5 micrometer, respectively.

The monochromator and the sample are placed in vacuum of about 1 Pa.

K. Ohsumi

5. MAX-90, A new High Pressure Diffractometer

A new X-ray experiment system for high pressure and high temperature study has been constructed. The new system, named MAX-90, was designed based on the past experience with MAX-80 at PF and AR. The system consists of a cubic type high pressure vessel (DIA10 type by KOBELCO), a 350 ton press, a large scale

goniometer system, a 4-axis table for adjusting the press (i.e. sample) to the goniometer center and a 2-axis base to align the system to X-ray beam.

The main feature of the new system is that a sintered diamond is used as an anvil material. So far, a cemented tungsten carbide has been used as an anvil materials, and the maximum pressure was about 13 GPa when an anvil set with 3 mm truncation was used. By using a sintered diamond anvil, pressure of 20 to 30 GPa is expected to be generated. The pressure generation in this region will be precisely studied using SR. In order to apply larger load to the high pressure vessel than before by a factor of 2 to 3, the press was constructed to clear the JIS special grade. A plunger type hydraulic pump is adopted so that the oil pressure of the 350 ton press is smoothly and accurately controlled for both of the pressure increase and decrease.

A handy SSD is used as a detector and diffracted or transmitted X-ray is analyzed by an MCA. Data acquisition and mechanical movements are controlled by a workstation (SUN386i).

The system is mainly used at BL-13, where SR comes from a 27-pole wiggler[1]. In this beamline, the brightness is expected to be 10 to 100 times higher than that of SR from bending magnet in the energy range of 10 to 50 keV. Featuring this characteristic, diffraction experiments with an angle dispersive mode will be positively performed, including a diffraction experiment utilizing an anomalous scattering.

Using MAX-90, studies of diamond formation, earth's interior materials, liquid materials, precise determination of compressibility, structure determination of high pressure phase, and EXAFS are planning.

O. Shimomura

1. PF Activity Report #5, p.80 (1987)

6. An apparatus for Electron-ion Coincidence Experiment

This apparatus has been designed and constructed for Auger electron-fragment photoion coincidence experiment of free molecules. The kinetic energy of Auger electrons defines the electronic state of doubly charged molecular ions. Therefore, the coincidence measurements can determine the dissociation path from the specific electronic states of the molecular ions.

The apparatus consists of three parts (see Figs. 22 and 23); a supersonic molecular-beam ejection system, a parallel plate electrostatic analyzer with a position-sensitive detector[1] for Auger electron measurements, and a time-of-flight spectrometer[2] for mass analysis of fragment photoions. To make a supersonic molecular beam, the region between a skimmer and an orifice of 100 μm diameter is evacuated by a 1000 l/sec turbo molecular pump. The chamber, in which the electron analyzer and time-of-flight spectrometer are installed, is evacuated by a 400 l/sec turbomolecular pump. The ultimate pressure of the chamber reaches to 2×10^{-8} Torr without sample-gas introduction. To reduce the magnetic field of the earth, double μ-metal shieldings are installed inside the chamber. The electron analyzer or time-of-flight spectrometer can rotate around incoming light in a plane perpendicular to the light.

A two-dimensional multi-channel analyzer is equipped with the apparatus to store Auger electron spectrum and mass spectrum simultaneously. This multi-channel analyzer has a function to store only the signals for events that occur within a set time window. Auger electron spectrum in coincidence with a specific fragment photoion will be stored in the multi-channel analyzer.

In the present case, the drift-tube length of the time-of-flight spectrometer was reduced to 19 cm taking into account the diameter of the vacuum chamber.

A. Yagishita

1. A. Yagishita, Japan. J. Appl. Phys. 25, 657 (1986).
2. A. Yagishita et al., KEK Report 86-6 (1986).

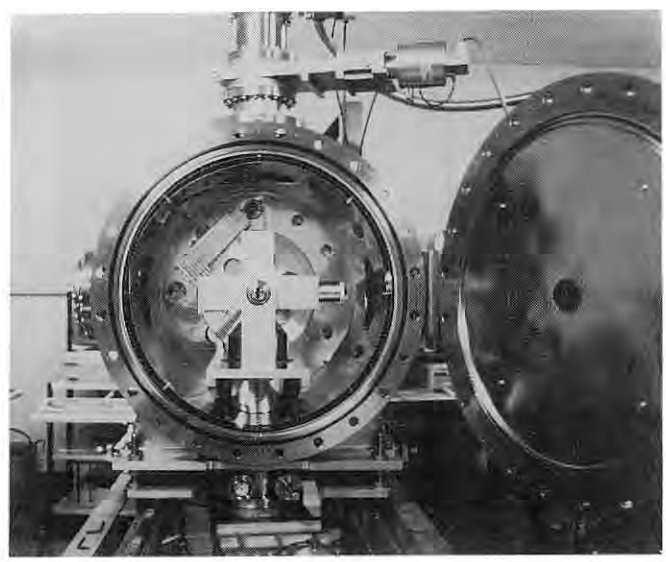

Fig. 22. A photograph of the apparatus for electron-ion coincidence experiment. The diameter of the vacuum chamber is 648 mm.

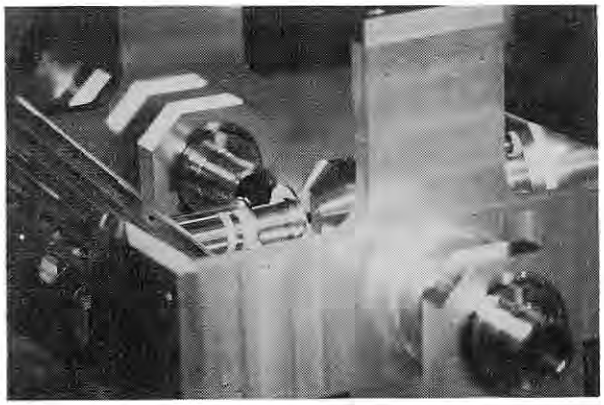

Fig. 23. A photograph of the electron analyzer and time-of-flight spectrometer both mounted on a rotatable arms.

E. SUMMARY OF EXPERIMENTAL STATIONS, APPARATUSES AND BEAMLINE OPTICS.

Figures 24 and 25 are the latest overview of the SR laboratory area of the TRISTAN-AR and the PF Experimental Hall schematically showing arrangement of total of 65 experimental stations now working or under construction. This section summarizes the working experimental stations and apparatuses with the assigned contact persons. Outline of the beamline optics, monochromators and optical elements for each beamline are also summarized in tabulated forms.

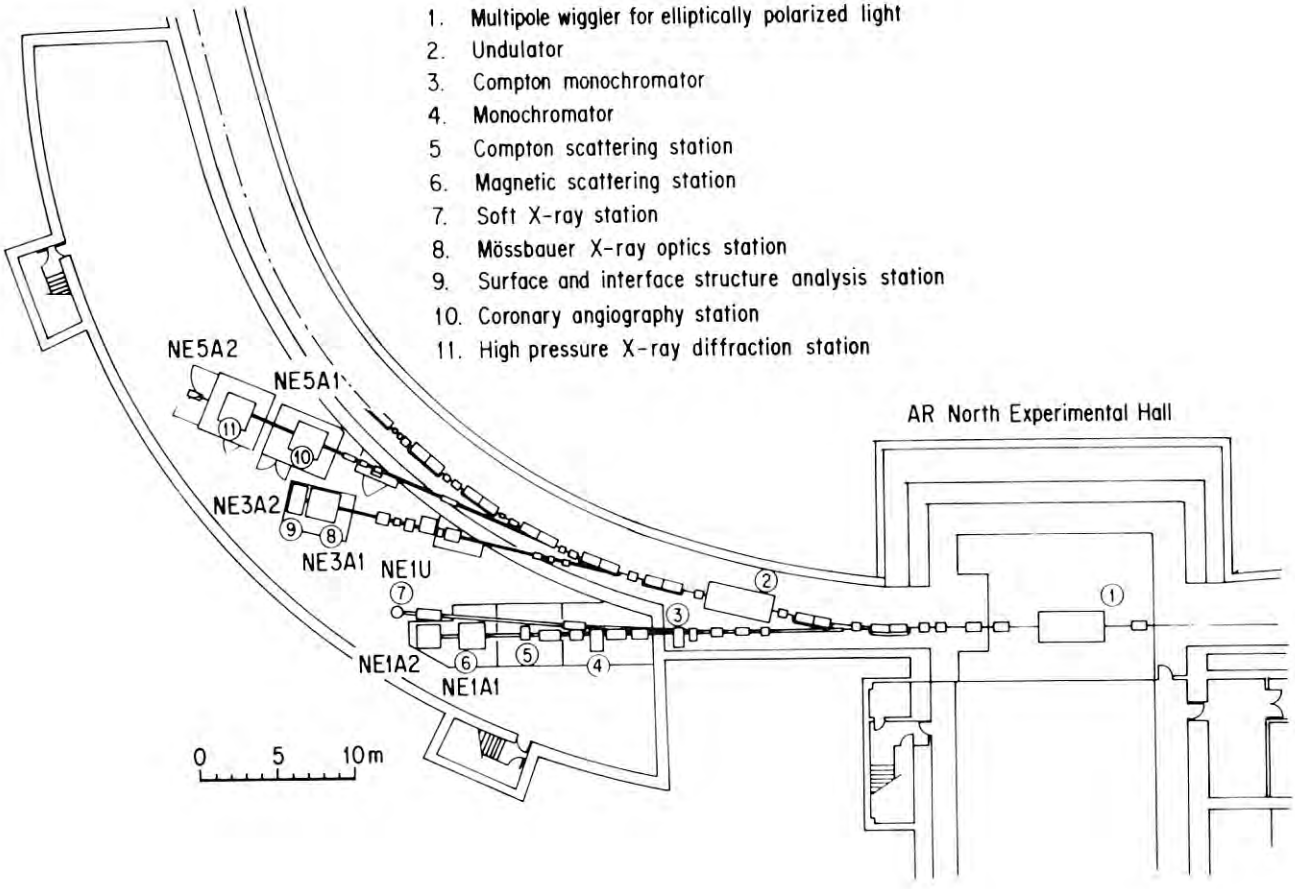

Fig. 24. Plan view of the synchrotron radiation laboratory area of the TRISTAN Accumulation Ring.

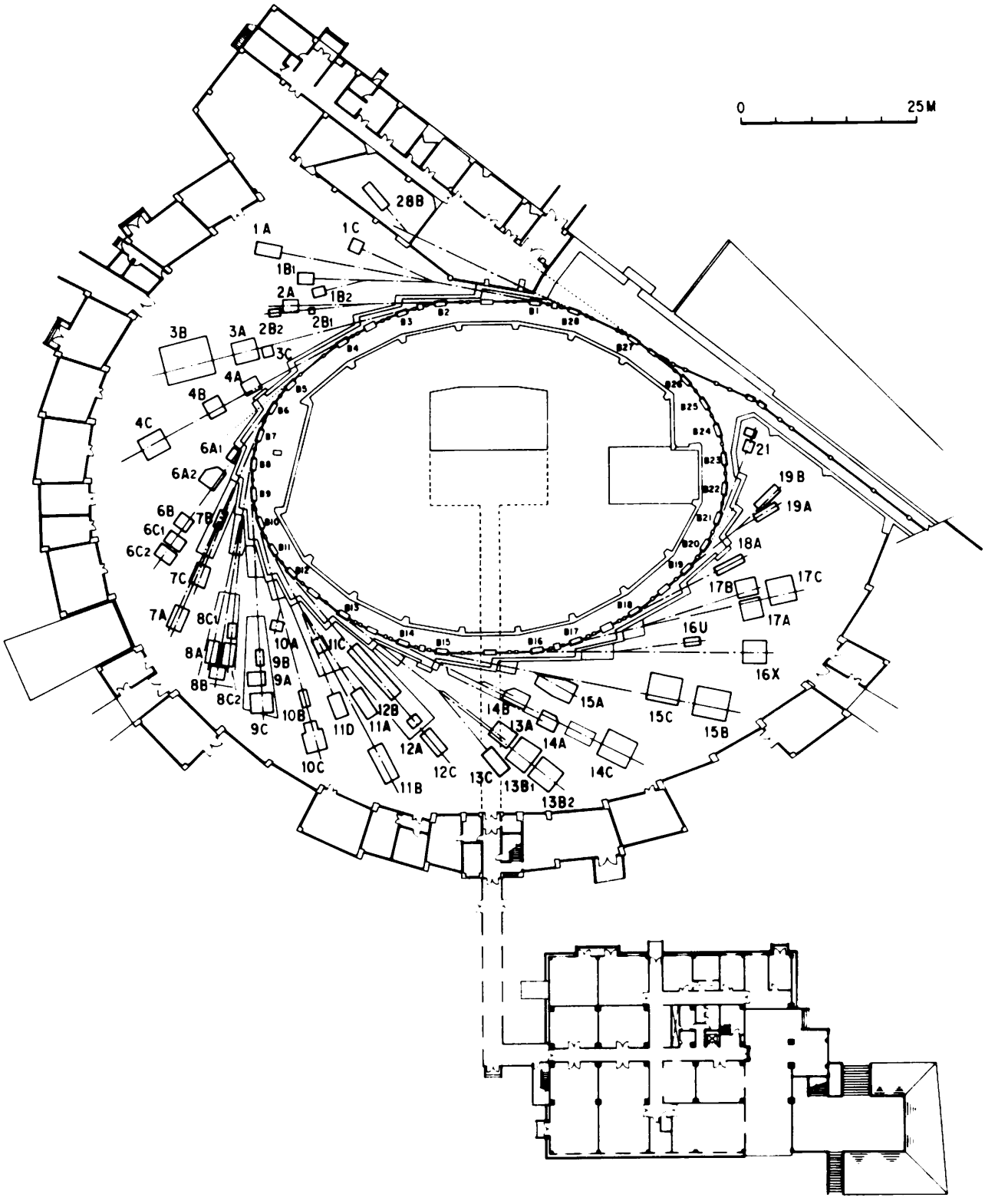

Fig. 25. Plan view of the Photon Factory Experimental Hall.

1. List of Experimental Stations

Beamline & Station		Contact person
BL-1	(NTT)	
1A	Solid surface analysis	M. Oshima
1B	X-ray lithography	T. Kaneko
1C	Photo-chemical reaction	T. Urisu
BL-2	(Undulator)	
2A	Soft X-ray spectroscopy	H. Maezawa
2B1	Soft X-ray microscopy	"
2B2	Soft X-ray spectroscopy	"
BL-4		
4A	Trace element analysis, Radiation effects on living cells	A. Iida
4B	Liquid/melt structure analysis, Powder diffraction	K. Ohsumi
4C	X-ray diffuse scattering, Fluorescent EXAFS	T. Matsushita
BL-6		
6A1	Ultra small angle X-ray scattering	T. Ishikawa
6A2	Macromolecular crystallography by Weissenberg camera	N. Sakabe
6B	X-ray spectroscopy and diffraction	M. Nomura
6C1	X-ray diffraction at low temperatures	T. Nakajima
6C2	Accurate lattice parameter measurement	M. Ando
BL-7	(The Research Center for Spectrochemistry, Univ. of Tokyo)	
7A	Soft X-ray photoemission spectroscopy	H. Namba
7B	Surface photochemical reaction	"
7C	X-ray spectroscopy and diffraction (PF)	M. Nomura
BL-8	(Hitachi)	
8A	Soft X-ray spectroscopy	K. Hayakawa
8B	EXAFS	"
8C1	X-ray lithography	"
8C2	X-ray tomography and digital radiography	"
BL-9	(NEC)	
9A	X-ray lithography	J. Matsui
9B	Photochemical reaction	"
9C	EXAFS and X-ray topography/diffraction	"
BL-10		
10A	X-ray diffraction/scattering, Crystal structure analysis	S. Sasaki
10B	EXAFS	M. Nomura
10C	Small-angle X-ray scattering of enzymes, Surface diffraction	K. Kobayashi
BL-11		
11A	Soft X-ray spectroscopy	A. Yagishita
11B	Surface EXAFS, soft X-ray spectroscopy	Y. Kitajima
11C	VUV solid state spectroscopy	H. Kato
11D	Angle-resolved photoelectron spectroscopy	"
BL-12		
12A	VUV gas phase spectroscopy	K. Tanaka
12B	VUV high resolution absorption	K. Ito
BL-14	(Vertical wiggler)	
14A	Crystal structure analysis of proteins, EXAFS at high photon energy	Y. Satow
14B	High precision X-ray optics	T. Ishikawa
14C	High speed X-ray topography, X-ray radiography,	

	Magnetic and Compton scattering	H. Kawata
BL-15		
15A	Small-angle X-ray scattering of muscle and alloys	Y. Amemiya
15B	X-ray topography and interferometry	H. Kawata
15C	High resolution X-ray diffraction	T. Ishikawa
BL-17	(Fujitsu)	
17A	Characterization of crystals	T. Hisatsugu
17B	Photochemical vapor deposition	"
17C	X-ray lithography	"
BL-21	(Light Source Division)	
	Beam position monitoring	T. Katsura
NE-5	Tristan Accumulation Ring (AR)	
5A1	Angiography	K. Hyodo
5A2	High pressure & high temperature X-ray diffraction	T. Kikegawa

2. List of Experimental Apparatuses

Format

Name of apparatus
1. General characteristics
2. Accessories
3. Other features
4. Typical Experiment
5. Station
6. Contact person
7. Pages in (A) Act. Rept. 82/83, (B) Act. Rept. 83/84, (C) Act. Rept. 84/85, (D) Act. Rept. 86, and (E) Act. Rept. 87 where detailed description is found.

X-ray

(a) X-ray fluorescence spectrometer
1. Energy dispersive type spectrometer. Equipped with a Si(Li) detector. Elemental analysis with very high sensitivity.
2. X-Z scanning sample stage.
4. Trace element analysis of semiconductor, ceramics, sea water, human tissues, etc. Surface elemental analysis of semiconductor.
5. BL-4A.
6. A. Iida
7. (A) V-23

(b) Monochromatic X-ray irradiation system for radiation biology.
1. Usable wavelength region, 0.8 A - 3.0 A. Beam size, typically 30 mmH × 3 mmV.
2. X-Z sample scanning stage. Ionization chambers for measuring X-ray intensity.
4. Studies on Auger enhancement of bromine atom using various biological samples. Wavelength dependence of radiation effects on biological samples.
5. BL-4A.
6. K. Kobayashi
7. (C) VI-21

(c) X-ray diffractometer for liquids and melts
1. Collects intensity-data for radial distribution analysis for non-crystalline materials such as gases, liquids, melts and glasses.
2. θ-2θ goniometer with monochromator and analyzer. Single-crystal monochromator with quartz and β-alumina. Double crystal monochromator with Si(111). Keramax furnace.
4. Energy-dispersive study of gas and liquid. Angle-dispersive study of liquids, melts and powder crystals.
5. BL-4B.
6. K. Ohsumi
7. (A) V-24

(d) Powder diffractometer
1. Measurement and collection of diffracted X-ray intensity from powder crystals and/or amorphous materials for profile fitting technique.
2. High speed sample spinner. Counter monochromator (graphite). Heating furnace.
3. $\Delta\lambda/\lambda - 10^{-5}$ Available of energy dispersive mode of diffractometry. Almost all of an X-ray path being in vacuum.
4. Angle-dispersive study of powder specimens or amorphous materials. Energy-dispersive study of powder specimen or non crystalline materials. Diffraction study using anomalous dispersion.

5. BL-4B.
6. K. Ohsumi

(e) Four-circle diffractometer with a crystal analyzer
1. Enables high resolution measurement, in momentum and energy, of intensity distribution. Intensity measurement from samples at high pressures or at low temperatures.
2. Liquid nitrogen cryostat.
4. High resolution measurement of diffuse scattering intensity, pressure dependence of commensurate-incommensurate transition.
5. BL-4C.
6. S. Kishimoto
7. (D) 160

(f) Focusing Weissenberg camera with multi-layer-linescreens
1. High resolution macromolecular crystallography with high S/N ratio. Equipped with multi-layer-line screens.
2. Cooling unit by N_2 gas.
3. Wide range of w-axis rotation. Wide 2θ range.
4. X-ray structure determination of macro-molecular crystal (insulin, actin-DNise I complex, Plasminostreptin, etc.)
5. BL-$6A_2$.
6. N. Sakabe
7. (A) VI-5

(g) Low temperature X-ray diffractometer
1. Equipped with a three-axis goniometer ($\omega, 2\theta, \chi$) mainly used for low temperature ($\geq$ 0.3 K) X-ray diffraction.
2. Some types of refrigerators and magnets.
3. Available addendum limited to 500 kg in weight.
4. Peiels transition $K_{0.3}MoO_3$.
5. BL-6C.
6. T. Nakajima
7. (A) V-25

(h) EXAFS spectrometer (II)
1. Designed for X-ray absorption spectroscopy in transmission mode and in fluorescence detection mode.
2. Control and data acquisition system. Closed cycle refrigerator.
4. EXAFS.
5. BL-7C.
6. M. Nomura
7. (D) 90

(i) X-ray Lithography (Hitachi Central Res. Lab.)
1. X-ray Lithography.
2. Band-pass optics, nonlinear wobbling mirror, low vacuum separating Be window, SSD X-ray detector.
3. White beam available, high speed SX shutter.
4. X-ray Lithography.
5. BL-$8C_1$.
6. T. Kimura

(j) X-ray computed tomographic imaging system (Hitachi Res. Lab.)
1. X-ray source : Monochromatic X-ray (7 keV - 40 keV).
Detector : X-ray sensing pickup tube.
Spatial resolution : - 10 μm.
Field of view : $\leq$ 10 mm.
4. Observation of internal structure of composite ceramics.
5. BL-$8C_2$
6. K. Usami

(k) EXAFS spectrometer (NEC)
1. Designed for X-ray absorption spectroscopy in transmission mode and in fluorescence detection mode.
2. Control and data acquisition system, closed cycle refrigerator (GK $\leq T \leq$ 300 K).
3. Focused beam is available.
4. EXAFS.
5. BL-9C.

(l) High-precision triple-crystal X-ray diffractometer (NEC)
1. Equipped with three crystal stages. Mainly used for a grazing incidence diffraction, X-ray topography.
2. Two high-precision goniometers (0.01"/pulse for θ, 0.004°/pulse for 2θ), two 220ϕ goniometers (0.0002°/pulse for ϕ, 0.0004°/pulse for 2ϕ), a 400ϕ goniometer (0.002°/pulse for ϕ), a goniometer for grazing incidence diffraction.
4. X-ray topography. Grazing incidence X-ray diffraction.
5. BL-9C.
6. J. Mizuki
7. (D) 88

(m) Six-circle-X-ray diffractometer (NEC)
1. Study of crystal structure for single crystal under various conditions (pressure & temperature).
2. Closed cycle refrigerator (13 K $\leq T \leq$ 300 K), image furnace (300 K $\leq T \leq$ 800 K).
4. Single crystal X-ray diffraction. Diffuse scattering.
5. BL-9C.
6. J. Mizuki
7. (D) 88

(n) Vertical-type four-circle diffractometer
1. Crystallographic studies and scattering experiments.
Large X-circle (280 mmϕ).
2. Control system with MELCOM 70/30.
High-temperature furnace.
X-rays film cassette.
4. Diffraction and diffuse scattering.
5. BL-10A.

6. S. Sasaki
7. (A) V-27

(o) EXAFS Spectrometer (I)
1. Dedicated to X-ray absorption spectroscopy.
High-resolution. Easy operation.
2. Control system with a microcomputer (SORD M-223).
Closed cycle refrigerator.
Reaction chamber for catalyst.
Furnace. (800°C).
4. EXAFS.
5. BL-10B.
6. A. Koyama, M. Nomura
7. (A) V-8

(p) Small angle X-ray scattering equipment for solutions (SAXES)
1. Dedicated to small-angle scattering for solutions, synthetic polymers.
2. Stopped flow apparatus.
Temperature jump apparatus.
Flash light for specimen.
3. Uses monochromatic beam from the optics installed at BL-10C.
4. Measurements for Bovine Serum Albumin, Lysozyme, Tobacco Mosaic Virus, Purple Membrane, etc.
5. BL-10C.
6. K. Kobayashi
7. (A) V-29

(q) Ultra-high vacuum X-ray diffractometer
1. Ultra-high vacuum with cryo-pumping system.
Equipped with X-ray diffractometer and LEED optics.
2. Super precision goniometer using elastic torsion mechanism.
Microcomputer control system.
NaI scintillation counter system and SSD.
4. Study on Si(7 × 7) structure.
5. BL-10C.
6. T. Ishikawa
7. (A) V-34

(r) Time-resolved X-ray measurement system with 1D-PSD
1. Time resolution up to 1 msec.
Either 256 ch. × 191 frames, 512 ch. × 95 frames, or 1024 ch. × 47 frames.
Fast data acquisition up to 1 MHz.
2. LSI 11/23 computer.
CAMAC modules (Time to Digital Converter, Histogramming Memory, etc.).
3. Uses monochromatic X-ray (λ = 1.5 Å).
4. Measurements on frog skeletal muscle, purple membrance, Ribosome, etc.
5. BL-10C, BL-15A1.
6. Y. Amemiya
7. (A) V-35

(s) Horizontal-type four circle diffractometer
1. Specially built, but having a conventional diffractometer configuration.
Fully computer-controlled for rapid, tunable and precise diffraction data collection.
2. Computer-controlled alignment carriage with 5 stepping motor driven axes, on which the diffractometer is mounted.
Rotation camera.
MELCOM 70/60 minicomputer with OPTRONICS FILM SCANNER.
3. Mechanical control interfaced through IEEE-488 bus.
CAMAC and NIM measuring system.
4. Crystal structure analysis of antibiotics, biotic metabolitos, proteins, etc.
5. BL-14A.
6. Y. Satow
7. (A) V-30

(t) High-speed X-ray topography camera
1. Equipped with two X-ray TV cameras.
Maximum load of 30 kg on sample goniometer.
Facilities simultaneous observation of two different Laue spots.
2. Microcomputer system (AIDACS-3000).
Image processor TF4110.
Work shutter for variable exposure time (0.1 - 9.9 sec.).
3. 1 arc sec accuracy of θ-rotation.
Ample space around the specimen position.
4. Melting process of GaAs.
Magnetization process of Fe-3% Si, etc.
5. BL-15B, BL-14C.
6. H. Kawata
7. (A) V-31

(u) X-ray diffractometer for gasses
1. Equipped with horizontal ω-2θ two-circle goniometer.
χ-ϕ circle motion available.
2. Gas cell with boiling system.
Gas cell for pressure tight experiments.
Incident beam monitor with SSD.
3. Uses white beam for energy-dispersive method. Uses monochromatic beam for angle-dispersive method.
4. Angle-dispersive X-ray diffraction and Compton scattering study of carbon dioxide.
5. BL-15C, 14C.
6. T. Mitsuhashi
7. (B) VI-172

(v) Three-axes X-ray diffractometer
1. Equipped with three precision goniometers (Huber 410, 420, and 440).
2. Scintillation counter.
SSD with MCA.
Asymmetry cut plane monochrometer.
3. Accuracy of 0.36 arc sec per pulse.
4. Phase-contrast microscopy.

Development of application to medical diagnosis.
5. BL-15B.
6. H. Kawata
7. (A) V-32, VI-97, VI-98

(w) Precision X-ray optics
1. Goniometer assembly dedicated to precision diffraction study such as double-, triple-, and more than triple-crystal diffractometry and topography.
2. Microcomputer control system.
NaI scintillation detector system.
SSD and MCA.
Ionization chamber for monitoring.
Room temperature controller.
Experimental table with air springs.
3. 1 arc sec accuracy for full rotation.
0.1 arc sec accuracy within 6° using tangential bar system.
Employs super-precision rotation mechanism with elastic torsion and PZT.
4. Detection of polarization rotation under magnetic diffraction condition.
Structure analysis of epitaxial layer/substrate interfaces with standing wave method.
5. BL-15C.
6. T. Ishikawa
7. (A) V-33

(x) X-ray diffraction
1. Equipped with horizontal or vertical θ-2θ goniometer.
2. Measurable in He gas.
Usable an additional monochrometer.
3. A double crystal monochrometer is set at the beamline.
4. General Purpose.
5. BL-17A.
6. S. Komiya

(y) Rapid acquisition system of two dimensional images for medical application
1. Dedicated to development of medical diagnosis using two-dimensional image acquisition system.
Large exposure area (70 mmH × 120 mmV) is obtained by asymmetrical reflection from a crystal.
Usable energy is 33 KeV ± 3 KeV.
2. Two-dimensional detector system using a metal image intensifier.
Polished Si single-crystal monochromator with 311 reflection.
Z scanning table detector and sample.
X scanning stage for sample.
4. Studies on medical application to diagnosis such as angiography, K-edge subtraction and computed tomography.
5. ARØNE-5A1.
6. K. Hyodo

(z) Multi anvil high pressure X-ray system
1. Maximum pressure 13 GPa.
Maximum temperature 1700 °C.
Sample volume (typical) 2 mmϕ × 3 mmH.
White and monochromatic X-ray.
2. Two axis goniometer.
Handy type SSD (pure Ge).
3. Best quality in the world for this research field.
4. Structure of liquid Se, Ga and Bi at high pressure.
Precise determination of the equation of state of mantle minerals.
Measurement of Debye-Waller factors of Al and Mo at high pressure.
5. ARØNe-5A2.
6. T. Kikegawa
7. (A) V-26

Soft X-ray and VUV

(a) Monochromatic soft X-ray irradiation system for radiation biology studies
1. Usable wavelength 3 Å - 6.5 Å.
Beam size, typically 7 mmH × 4 mmV.
2. X-Z sample scanning chamber.
4. Biological effects of soft X-ray resonance absorption around the K-shell absorption edge of phosphorus.
5. BL-1B.
6. K. Kobayashi
7. (D) 235

(b) Gas-phase angle resolved photoelectron spectrometer
1. Ultimate pressure 5×10^{-8} Torr.
Equipped with a conventional hemispherical electrostatic analyzer and with a position-sensitive parallel-plate electrostatic analyzer.
2. Sample-gas inlet system.
3. A sample gas is confined in a gas cell.
5. BL-2B'.
6. A. Yagishita
7. (A) V-42

(c) Reflection, absorption, and photoemission (Hitachi Advance Res. Lab.)
1. Spectrometer.
2. Evaporator.
4. Analysis of multilayered structure, evaluation of optical elements, and study of electronic structure of superconductors.
5. BL-8A.
6. Y. Hirai

(d) SR induced photochemical reaction (NEC)
1. High vacuum (4×10^{-10} Torr).
2. Reactant-gas inlet system.
Angle resolved Q-pole mass spectrometer.
RHEED, AES, EELS.
4. SR induced photochemical reaction.
5. BL-9B.
6. I. Nishikawa

(e) VUV and soft X-ray reflectometer
1. Equipped with a goniometer, insuring accurate incidence angle (30 sec).

Up to 89.4° incidence angle.
Easy optical alignment.
Easy sample exchange.
High vacuum (2×10^{-9} Torr).

3. Equipped with ports for vacuum evaporation.
4. Optical constants of mirror materials. Surface roughness.
5. BL-11A.
6. T. Miyahara
7. (A) V-41, VI-78

(f) Apparatus for surface EXAFS experiments

1. Base pressure $< 1 \times 10^{-10}$ mbar.
Equipped with a CMA and a soft X-ray fluorescent proportional counter.
2. Some equipments for sample preparation and characterization such as LEED, Ar^+ ion gun, e-gun for AES.
3. Mobile.
4. Surface EXAFS and soft X-ray standing wave method.
5. BL-11B.
6. Y. Kitajima
7. (B) V-9

(g) UHV experimental chamber for absorption measurements I.

1. Ultra-high vacuum (5×10^{-11} Torr).
Equipped with an electron-beam gun for evaporation of samples.
Equipped with a quartz oscillator capable of being cooled to LNT.
2. Sample holder with an adjustable linear motion, capable of being cooled to LNT.
3. Designed mainly for very reactive metal samples.
4. Absorption of alkali metals, alkali metal alloys, and rare earth metals.
Near-normal reflectance.
5. BL-11C, BL-11D, BL-11A.
6. T. Miyahara
7. (A) VI-82

(h) Apparatus for ARPES experiment for solid state

1. Base pressure 5×10^{-11} Torr.
Equipped with a hemispherical analyzer mounted on a two axis rotation mechanism.
2. Some equipments for sample preparation and characterization.
Sample bank and transfer system.
Sample gas inlet system.
4. Mainly for angle-resolved photoelectron spectroscopy (ARPES) of single crystals.
5. BL-11D.
6. H. Kato
7. (B) V-10

(i) Time-of-flight spectrometer for photoion measurements

1. Ultimate pressure 5×10^{-8} Torr.
Electrostatic lenses satisfying the conditions of double-field space focusing for ions.
2. Furnace to evaporate alkali and alkaline-earth metals.
4. The measurements of double and multiple photoionization cross sections of Ca, Sr, Rb, Cs and Ba.
5. BL-2A, BL-11A.
6. A. Yagishita
7. (A) V-40

(j) Multi-technique surface analysis system (NTT)

1. Surface analyses such as photoemission spectroscopy, surface EXAFS, AES, SIMS, LEED EELLS and ISS in conjunction with an MBE chamber.
2. CLAM analyzer, angle-resolved electron analyzer, LEED optics, Q-mass filter, X-ray source, ELS electron gun, auger electron gun, He ion gun.
4. Surfaces and interfaces of semiconductors and superconductors by using SRPES and SEXAFS.
5. BL-1A.
6. M. Oshima
7. (D) 144-117

(k) Angle resolved electron spectrometer (RCS)

1. Electron spectroscopy for surface studies.
2. Low energy electron diffraction, auger electron spectroscopy, surface preparation tools.
3. Based on beamline ADES 400 of V.G.
4. Photoelectron spectroscopy, surface EXAFS.
5. BL-7A and 7B.
6. H. Namba (University of Tokyo)

(l) X-ray lithography (Fujitsu Lab.)

1. X-ray lithography.
2. Low-pass mirror, energy dispersive type spectrometer with a Si(Li) detector.
3. White beam is available.
4. X-ray lithography.
5. BL-17C.
6. S. Gotoh
7. (E) 81

Table 2. X-Ray Beamline Optics and Monochromators

Branch Beam Line	Horizontal Acceptance Angle (mrad)	Typical Beam Size (Hmm × Vmm)	Photon Flux at Sample Position	Monochromator (Crystal)	Energy Resolution $(\Delta E/E)\times10^{-4}$	Energy Range (keV)	Mirror	Line Vacuum (Gas)
BL-4A	6	50 × 4 (4 × 1)		Double Crystal Si (111) (Saggital Focusing)	~ 2	4 ~ 20	None	Vacuum
BL-4B	4.5	50 × 5		Double Crystal Si (111)	~ 2	4 ~ 35	None	Vacuum
BL-4C	4	4 × 1		Double Crystal Si (111) (Saggital Focusing)	~ 2	4 ~ 20	None	Vacuum
BL-6A1	0.1	10 × 3		Plane (111)	7.5	8 ~ 17		Vacuum
BL-6A2	4	2.5 × 1		Bent Si (111) (α = 0, 6.0°, 7.8°, 9.5°, 11.4°, 13.7°, 16.5°)		5 ~ 25	Bent Plane Fused Quartz	Vacuum
BL-6B	4	8 × 1		Double Crystal Si (220), Si (111) (Saggital Focusing)		4 ~ 25 (4 ~ 16 when focused)	None	Vacuum
BL-6C1	0.5	10 × 5		None		8 ~ 30		Vacuum
BL-6C2	0.5	5 × 5		Channel-Cut Si (111)	7.5	8 ~ 12	None	Vacuum
BL-7C	4	8 × 1	$4 \times 10^9/7mm^2$ (8 keV, 100 mA) (3×10^{10} when focused)	Double Crystal Si (111) (Saggital Focusing)	2	4 ~ 20 (4 ~ 13 when focused)	None	Vacuum
BL-8C	5	50 × 5	$2 \times 10^6/mA{\cdot}mm^2$ at 10 keV with Si (111)	Channel-Cut Si (220), Si (111), Si (400)	~ 2	5 ~ 40	None	Vacuum & He
BL-9A	5	25 × 25				1.2 ~ 3.1	SiC	Vacuum
BL-9C	5	150 × 5		Double Crystal Si (111) (Saggital Focusing)	~ 2	5 ~ 25	None	Vacuum

Branch Beam Line	Horizontal Acceptance Angle (mrad)	Typical Beam Size (Hmm × Vmm)	Photon Flux at Sample Position	Monochromator (Crystal)	Energy Resolution ($\Delta E/E \times 10^{-4}$)	Energy Range (keV)	Mirror	Line Vacuum (Gas)
BL-10A	1	10 × 3		Si (111), Si (220) Ge (111), InSb (111) Quartz (100), PG (002) Curved Si (111) (α ~ 4°, 8°)	50 ~ 5	5 ~ 25	None	Helium
BL-10B	2	8 × 1	$3 \times 10^8/7mm^2$ (10 keV, 100 mA)	Channel-Cut Si (311)	1	6 ~ 30	None	Vacuum
BL-10C	4	6 × 1.5	~ $10^{10}/9mm^2$ (8 keV, 100 mA)	Double Crystal Si (111)	2	4 ~ 10	Bent Cylinder	Helium
BL-13A	1			Double Crystal Si (220)	~ 0.1	4 ~ 30	None	Vacuum
BL-13B	4			Double Crystal Si (111), Si (220)	~ 2	4 ~ 25	Bent plane Fused Quartz	Vacuum
BL-14A	1.28 (Vertical)	5 × 38		Double Crystal Si (111) Si (331) Si (553)	2	5.1 ~ 19.1 12.9 ~ 48 22.7 ~ 84.5	Bent Cylinder for Vertical Forcusing, Pt-cauted Fused Quartz	Vacuum (line) He (monochromator)
BL-14B	2.2	5 × 30		Double Crystal Si(111),Si(220),Si(311) (Saggital Focusing)	2	5.2 ~ 57	None	Vacuum
BL-14C	1.3	10 × 40		Double Crystal Si (111)	2	5.5 ~ 43	None	Vacuum
BL-15A	2	2.6 × 1.3	$9 \times 10^{10}/6mm^2$ (8.0 keV, 150 mA)	Curved Crystal Ge (111) (α = 8.0°)	~ 10	5.6 ~ 12.4	Cylinder, Fused Quartz	Vecuum and He
BL-15B	0.14	5 × 5		None		3.5 ~ 34	None	Vacuum
BL-15C	2	60 × 6		None		4 ~ 35	None	Vacuum
BL-16X	4	4 × 1		Double Crystal Si (111) (Saggital Focusing)	~ 2	4 ~ 35	Commissioning	Vacuuum

Branch Beam Line	Horizontal Acceptance Angle (mrad)	Typical Beam Size (Hmm × Vmm)	Photon Flux at Sample Position	Monochromator (Crystal)	Energy Resolution ($\Delta E/E \times 10^{-4}$)	Energy Range (keV)	Mirror	Line Vacuum (Gas)
BL-17A	4	100 × 10		Double Crystal Si (111)	~ 2	4 ~ 5	None	Vacuum
BL-17C	1	20 × 5		None		1	Quartz (plane)	Vacuum
ARNE1-A1	2	30 × 7 (3 × 1)		Single Crystal Si (111) (Double bent crystal Si (111))	~ 10	50 ~ 70	None	Vacuum
ARNE1-A2	2	80 × 10 (10 × 10)		Double Crystal Si (111) (Saggital Focusing)	~ 2	6 ~ 100	In Planning	Vacuum
ARNE5-A1	10	120 × 70		Single Crystal Si (311) (α = 5.9°)	~ 60	33	None	In Planning
ARNE5-A2	10	30 × 10		Double Crystal Si (111) (Saggital Focusing)	~ 10	30 ~ 100	None	In Planning

Table 3. VUV and Soft X-Ray Monochromators

Branch Beamline	Monochromator	Grating/Crystal	Groove density (l/mm)/spacing	Blaze (Å)	Typical Resolution	Range (Å)
BL-1A (NTT)	Grating/Crystal	Au-Coated Original InSb(111) Si(111)	1200 2d = 7.4806 A 2d = 6.27064 A		$\lambda/\Delta\lambda$ ~ 2000	2 ~ 2000
BL-1B (NTT)	Filtered White					
BL-1C (NTT)	Plane Grating	Pt-coated	1200 600		$\lambda/\Delta\lambda$ ~ 100	
BL-2A	Double Crystal with Constant Exit Beam	InSb(111)	2d = 7.4806 A			7.3 ~ 2.0
BL-2B1	Fresnel Zone Plate Microscope					30 ~ 15
BL-2B2	10m Grazing Incidence with Fixed Incidence Angle of 89°	Au-Coated Replica (Hitachi)	2400 1200	8 16	$\Delta\lambda$ = 0.004 A $\Delta\lambda$ = 0.008 A for 10μ–10μ Slits	6 ~ 25 6 ~ 50
BL-7A (RCS)	Grazing Incidence	Plane Au-Coated (Hitachi) " (Shimadzu)	1200 2400		$\lambda/\Delta\lambda$ ~ 500	12 ~ 1200
BL-7B (RCS)	1m Seya-Namioka	Au-Coated Replica (Hitachi, B & L)	1200 2400	380 960 1600	$\lambda/\Delta\lambda > 1000$	275 ~ 2500
BL-8A (Hitachi)	Grazing Incidence	Plane Self-focusing	2400 800	5 80	$\lambda/\Delta\lambda \sim 10^{-3}$	7 ~ 100 80 ~ 300
BL-8B (Hitachi)	Double Crystal	InSb(111), Beryl(1010) Si(311), (422)			$\lambda/\Delta\lambda \sim 10^{-4}$	0.4 ~ 1
BL-9A (NEC)	Oscillating Mirror					
BL-9B	Grazing Incidence	Plane				30 ~ 2000
BL-11A	Grasshopper Mark VII 2m Grazing Incidence with Fixed Incidence Angle of 88°	Au-Coated Replica (Hitachi)	2400 1200	16.6 33.3	$\Delta\lambda$ = 0.02 A $\Delta\lambda$ = 0.04 A for 10μ–10μ Slits	10 ~ 145 10 ~ 290

BL-11B	Double Crystal	Ge(111)	2d = 6.53 A		ΔE = 1 eV at 2 keV	2.7 ~ 6.2
		InSb(111)	2d = 7.4806 A		ΔE = 0.8 eV at 2 keV	3 ~ 7
BL-11C	1m Seya-Namioka	Au-Coated Replica (Hitachi)	2400	785	$\Delta\lambda$ = 0.3 A at 500 A	400 ~ 150
		Al-Coated Replica (Shimadzu)	1200	785	for 50μ–50μ Slits	400 ~ 3000
			1200	1300		
BL-11D	2m Grqazing Incidence Constant	Au-Coated Replica	2400	32	$\lambda/\Delta\lambda$ ~ 1700	80 ~ 150
	Deviation	(B & L, Hitachi)	1200	116	for 25μ–25μ Slits	120 ~ 300
	($\alpha + \beta = 154°$)		600	460		240 ~ 600
BL-12A	1m Seya-Namioka	Au-Coated Replica	2400	508	$\Delta\lambda$ = 0.4 A at 500 A	350 ~ 1000
		(B & L)	1200	536	for 100μ–100μ Slits	350 ~ 2000
BL-12B	6.65m Normal Incidence Off-	Pre-Coated Replica (B & L)	1200	1500		
	Plane Eagle Mounting	Os-Coated Replica (B & L)	1200	5500	$\lambda/\Delta\lambda = 2.5 \times 10^5$ A	400 ~ 2500
		Os-Coated Replica (Hyperfine)	4800	900	at ~ 800 A	
BL-12C	Multilayer Reflector	Rh-Si 21 Layers			$\lambda/\Delta\lambda$ ~ 12	20 ~ 180
BL-16U	Grazing Incidence				$\lambda/\Delta\lambda > 1000$	20 ~ 300
BL-18A	Grazing Incidence		1200		$\lambda/\Delta\lambda > 1000$	40 ~ 1000
BL-19A	Grazing Incidence Constant	Au-coated (Shimadzu)	1200	50	$\lambda/\Delta\lambda > 1000$	50 ~ 127
	Deviation			132	for 20μm-20μm Slits	99 ~ 253
	($\alpha + \beta = 160°$, 170°)		600	198		80 ~ 496
				500		359 ~ 992
BL-19B	Plane Grating	Original Varied Spaced	2400		$\lambda/\Delta\lambda > 1500$	10 ~ 150
		Plane Grating (Hitachi)	800		for 20 μm-20μm Slits	30 ~ 450
BL-28	Normal/Grazing Incidence	Holographic (Shimadzu)	600		$\lambda/\Delta\lambda > 2000$	50 ~ 1500
	Constant Deviation		1200			
			2400			
ARNE1-U	10m Grazing Incidence	Au-Coated (Hitachi)	2400	8	$\Delta\lambda = 0.001$ Å	6 ~ 25
			1200	16	$\Delta\lambda = 0.002$ Å	6 ~ 50

Table 4. Optical Elements of VUV and Soft X-Ray Beamlines

Branch Beamline	Pre- and Re-forcussing mirror	Radius of Curvature (mm)	Angle of Incidence	Material	Coating	Dimension (mm)	Horizontal & Vertical Acceptance (mrad)	Typical Beam Size (mm)
BL-1A	Paraboloidal		89°	Fused Quartz	Pt	500 × 80 × 50	4.0 × 0.5	
(NTT)	Paraboloidal		89°	Fused Quartz	Pt	500 × 80 × 50		4 × 1
BL-1B	Plane			88° ~ 89°	SiC		1.2 × 4.0	
(NTT)						19 ϕ		
BL-1C	Toroidal			Fused Quartz	Pt		2.0 × 4.0	
(NTT)								
BL-2B1	Plane		88°	SiC	Pt	120 × 60 × 15		
BL-2B2	Plane		86.85° ~ 88.83°	Sic	Pt	120 × 60 × 15	0.14 × 0.4	
	Concave	8903	89°	Pyrex	Pt	ϕ 90 × 15		
	Concave	7527	89°	Pyrex	Pt	ϕ 90 × 15		
	Toroidal	R = 43574, ρ = 26.162	89°	Fused Quartz	Pt	240 × 40 × 15		
BL-7A	Bent Cylinder	R = 7.83×10^5, ρ = 420	88.4°	Quartz	Pt	750 × 140 × 30	6 × 1	
(RCS)	Toroidal	R = 2.58×10^4, ρ = 90	88.3°	Quartz	Pt	200 × 60 × 18		2 × 1
BL-7B	Cylinder	1600	15°	Cu	Pt	250 × 80 × 30	6 × 4	
(RCS)	Toroidal	R = 2510, ρ = 200	10°	Quartz	Pt	60 × 80 × 20		1 × 1
BL-8A	Plane		89°	Quartz	Pt	400 × 170 × 40	0.5 × 1.0	
(Hitachi)	Bent	6.5×10^4	89°	Quartz	Pt	160 × 50 × 5		5 × 1
BL-8B	Bent Cylinder	R = 1.6×10^6	6.3 mrad	Quartz	Ni	500 × 120 × 30	6 × 0.5	
(Hitachi)		ρ = 1.7×10^2						
BL-9A	Plane		89.15°	SiC		400 × 170 × 40	5 × 0.33	
(NEC)	Cylinder	309.5	89.15°	SiC		400 × 170 × 40	5 × 0.33	
BL-9B	Plane		87°	SiO_2	Pt	700 × 60 × 20	0.2 × 0.2	

BL-11A	Spherical	360000	88°	SiC	Pt	400 × 170 × 40	1.3 × 0.4	
	Spherical	28000	88°	Fused Quartz	Au	300		
	Bent Cylinder	R ~ 3000	89°	Pyrex	Pt	220 × 24 × 6		1 × 0.3
BL-11B	Bent Cylinder	R ~ 950000, ρ = 300	89°	Fused Quartz	Pt	580 × 140 × 30	4.0 × 0.6	8 × 1
BL-11C	Plane		77.5°	SiC	None	250 × 100 × 40	4.8 × 3.0	
	Concave	5600	42.5°	Fused Quartz	Pt	100 × 100 × 20		
	Toroidal	R = 125, ρ = 2000	72.5 °	Pyrex	Au	90 × 50 × 10		~ 1ϕ
BL-11D	Toroidal	R = 250000, ρ = 750	86°	SiC	Pt	400 × 80 × 40	1.5 × 2.0	
	Plane		86°	Quartz	Au	50 × 40 × 10		
	Concave	4000	86°	BK-7	Au	50 × 40 × 10		
	Toroidal	R = 3500, ρ = 700,	77°	BK-7	Au	60 × 40 × 10		~ 1 ϕ
BL-12A	Cylinder	R = 1850	80°	SiC	None	250 × 200 × 40	2.4 × 1.5	
	Spherical	6250	45°	Fused Quartz	Pt	ϕ 100 × 20		
	Plane		80°	Pyrex	Pt	40 × 40 × 10		~ 1 ϕ
	Toroidal	R = 2000, ρ = 340	70°	Pyrex	Pt	30 × 40 × 10		
	Plane		80°	Pyrex	Pt	40 × 40 × 10		
BL-12B	Plane		80°	SiC	None	280 × 100 × 40	5.0 × 3.6	
	Concave	4321	35°	Pyrex	Pt	ϕ 110 × 20		
	Concave	2188.5	45°	Pyrex	Pt	ϕ 110 × 20		
BL-12C	Toroidal	R = 490455, ρ = 539,	88.1°					
BL-16U	Cylinder	R = 205294	87°	SiC	Pt	500 × 50 × 40	1.74 × 0.24	
	Plane			SiC	Pt	100 × 40 × 15		
	Cylinder	R = 1796	87°	SiC	Pt	100 × 40 × 15		
	Bent Cylinder	ρ = 52.4	86.22°	Quartz	Pt	220 × 30 × 8		
BL-17C (Fujitsu)	Plane		89° ~ 89.4°	Quartz	Pt	500 × 130 × 30	1.0 × 0.5	

Branch Beamline	Pre- and Re-forcussing mirror	Radius of Curvature (mm)	Angle of Incidence	Material	Coating	Dimension (mm)	Horizontal & Vertical Acceptance (mrad)	Typical Beam Size (mm)
BL-18A	Cylinder	R = 203252	87.5°	SiC	Au	500 × 50 × 50	2.0 × 2.0	
	Plane		86°	Quartz	Au	420 × 30 × 40		
	Bent Ellipse		87°	Quartz	Au	440 × 40 × 40		
	Toroidal	R = 16894, ρ = 72.9	87°	Quartz	Au	260 × 30 × 30		~ 0.5 ϕ
BL-19A	Plane		85°	SiC	Au	400 × 100 × 50	3.5 × 2.0	
	Toroidal	R = 350000, ρ = 372	86°	Quartz	Au	400 × 100 × 50		
	Spherical	R = 28000	86°	Quartz	Au	100 × 60 × 10		
	Toroidal	R = 13800, ρ = 320	85°	Quartz	Au	60 × 40 × 10		
	Toroidal	R = 7230, ρ = 1035	80°	Quartz	Au	60 × 40 × 10		< 0.3 ϕ
	Plane		80°	Quartz	Au, Al	60 × 40 × 10		
BL-19B	Cylinder	R = 500000	88.5°	SiC	Au	520 × 100 × 50	2.0 × 2.0	
	Plane		88.5°	SiC	Au	500 × 50 × 40		
	Toroidal	R = 38199, ρ = 52.3	87°	Quartz	Au	200 × 40 × 20		< 0.7 × 0.5
BL-28	Toroidal	R = 250000, ρ = 680	86°					
ARNE1-U	Bent Cylinder	R = 300000, ρ = 485	88.5°	SiO_2	Pt	700 × 60 × 20	0.2 × 0.2	
				SiC	Pt	450 × 150 × 65.5	5.0 × 1.0	

ISSN 0912-1803

PHOTON FACTORY ACTIVITY REPORT 1988

#6

NATIONAL LABORATORY FOR HIGH ENERGY PHYSICS, KEK

PHOTON FACTORY ACTIVITY REPORT 1988 #6